

**Western Australia School of Mines  
Department of Exploration Geophysics**

**Seismic Imaging in Hard Rock Environments**

**Konstantin Tertyshnikov**

**This thesis is presented for the Degree of  
Doctor of Philosophy  
of  
Curtin University**

**February 2014**

## Declaration

To the best of my knowledge and belief this thesis contains no material previously published by any other person except where due acknowledgment has been made.

This thesis contains no material which has been accepted for the award of any other degree or diploma in any university.

Signature: .....  .....

Date: ..... 13/02/2014 .....

To my parents

Olga and Victor Tertyshnikov,

and their parents before them...

## **Abstract**

The minerals industry is a substantial contributor to the economy in many countries. Accurate structural geological models of subsurface media are essential for mineral exploration and targeting. In the mining industry, electromagnetic and potential geophysical methods have traditionally been used for obtaining information about rock formations, but these techniques have strong limitations in spatial resolution, especially with increasing depth of investigation. Seismic exploration (especially seismic reflection method) provides the highest lateral and vertical resolution among geophysical remote sensing methods (capable of distinguishing layers with thicknesses of a few meters) and maintains that precision to depths of several kilometres. Migration algorithms are the final seismic processing steps to create accurate 2D and 3D images of the Earth's structures and define the true locations of subsurface objects from seismic data. Besides of having appealing benefits, seismic methods have certain problems in hard rock environments: geological settings are rather complex, contain a lot of steeply dipping interfaces and heterogeneities (faults, fracture zones, etc.); the environment is characterized by high propagation velocities of seismic waves; seismic data often have low intrinsic signal to noise ratio; near surface conditions are complicated (overburden rocks have a very high contrast in seismic properties with base formations). All these issues have to be studied and accounted for during seismic exploration to be able to achieve successful results.

This thesis focuses on a number of seismic imaging approaches to address the issues that seismic exploration is facing in hard rock environments. The study covers several aspects of seismic imaging involving analysis of different kinds of waves (surface, refraction, reflection, diffraction) for reconstruction of shallow and deep geological structures.

First, the work provides the results of a near surface 2D seismic experiment at the Hillside mine site (South Australia). The acquisition setup was designed to test the potential of seismic technology for regolith exploration and show the efficiency and cost effectiveness of the method for the mining industry. The experiment includes analysis of surface and refracted waves to reveal the structure of weathered cover and

to estimate the geotechnical rock properties. Results have demonstrated that near surface seismic methods can be used as an alternative and/or complement inexpensive geophysical tool for regolith exploration and mapping the near surface structures.

The following section describes the implementation and application of the velocity independent prestack time imaging algorithm. The need for such migration is justified by the difficulties in obtaining the velocity model exploiting standard velocity analysis techniques routinely used in oil and gas exploration. The algorithm has been tested on a number of simple synthetic models and illustrated an ability to handle data in the presence of random noise. The application to the synthetic model simulated the real geological settings and has demonstrated potential for imaging hard rock structures and estimating the velocity distribution. The final verification on the field seismic data from St Ives camp site (Western Australia) has proven the applicability of the velocity independent migration technique for purposes of imaging structural models in mineral exploration.

The next focus of the research is the development of the diffraction steered migration. Seismic exploration in hard rock environments often involves data with intrinsically poor signal to noise ratio. The presented imaging approach is capable of handling seismic records with severe noise conditions and enables detection and mapping of subvertical linear geological features (e.g. faults, fracture zones, etc.). The synthetic test has shown the stability of the steered migration in the presence of random noise. The algorithm has been applied to three field datasets from different geological regions: Western and South Australia and the Bismarck Sea. The comprehensive study on real seismic data revealed that the steered approach is able to significantly improve the quality of the final images and can be used for targeting of mineralization zones.

The research addresses challenges, which seismic methods are facing in hard rock environments, and considers particular solutions for a certain issue. The results of the study have an application to enhance the quality and increase the reliability of seismic images in hard rock exploration.

## **Acknowledgements**

First of all I would like to thank my parents, Olga and Victor Tertyshnikov, who have supported me through my life and continue to guide and take care of me.

I would like to thank my supervisor, Dr Roman Pevzner, for his encouragement, motivation and thoughtful advice. I am grateful to Dr Andrej Bóna for invaluable theoretical and technical discussions. I would like to thank Dr Andrew Greenwood and Dr Christian Dupuis for their experience sharing and the great time during the field projects. I am grateful to Dr Aleksei Shevchenko for constructive discussions about the theoretical aspects of seismic migration.

Special thanks to my friends for their emotional support and help, and many impressive weekends.

I would also like to thank the Department of Exploration Geophysics Curtin University for their years of support, servers for the hours of processing and software licenses. I would like to acknowledge the support of iVEC through the use of advanced computing resources located at iVEC@Murdoch. I am very grateful to Newcrest, Rex Minerals and Nautilus Minerals for permissions to publish the results from the real data examples.

The work has been supported by the Deep Exploration Technologies Cooperative Research Centre whose activities are funded by the Australian Government's Cooperative Research Centre Programme.

# Table of Content

1. Introduction .....	20
1.1. Hard Rock Seismic Imaging .....	20
1.2. Research Objectives .....	22
1.3. Thesis Structure .....	23
2. Australian Mineral Resources .....	25
2.1. Australian Mineral Deposits .....	25
2.1.1. Banded Iron Formation (BIF) .....	26
2.1.2. Iron-Oxide-Copper-Gold (IOCG) Deposits .....	29
2.1.3. Volcanogenic Massive Sulfide (VMS) Deposits .....	30
2.1.4. Porphyry Deposits.....	32
2.1.5. Orogenic Gold Deposits.....	34
2.1.6. Mississippi Valley Type (MVT) Deposits .....	36
2.1.7. Unconformity Type Uranium Deposits.....	37
2.2. Where to Expect New Discoveries .....	38
2.3. Seismic Exploration and Mineral Environments .....	40
3. Hard Rock Seismic Exploration.....	43
3.1. Overview of hard rock seismic exploration .....	43
3.2. Hard Rock Characteristics .....	46
3.3. Basics of Seismic Theory.....	48
3.3.1. Principals of Propagation of Seismic Energy.....	49
3.3.2. Seismic Reflectivity .....	50
3.3.3. Vertical and Horizontal Resolution of Seismic Data .....	52
3.3.4. Surface Waves and Multichannel Analysis of Surface Waves (MASW) .....	54
3.3.5. Refraction Seismic .....	57
3.3.6. Reflection Seismic .....	60
3.3.7. Diffraction Energy .....	64

3.3. Hard Rock Seismic Summary .....	66
4. Near Surface Seismic Imaging for Hard Rock Environments .....	68
4.1. Regolith Exploration .....	68
4.2. 2D Seismic Experiment at Hillside Mine Site .....	68
4.2.1. Seismic Acquisition .....	71
4.2.2. Multichannel Analysis of Surface Waves (MASW) .....	74
4.2.3. Refraction Data Analysis .....	77
4.2.4. Integrated results of MASW and Refraction Data Analysis .....	79
4.3. Near Surface Seismic Imaging Summary .....	82
5. Velocity Independent Imaging for Hard Rock Environments .....	83
5.1. Velocity-Less Prestack Time Migration .....	83
5.1.1. Implementation of the Velocity-Less Algorithm .....	84
5.2. Application to the Basic Models .....	88
5.2.1. Errors in Slopes Estimation.....	105
5.3. Synthetic Dataset Based on Realistic Geological Model .....	107
5.3.1. Comparison with Kirchhoff Prestack Time Migration .....	113
5.4. 2D Field Data Example – St Ives Mine Site .....	119
5.5. Velocity Independent Imaging Summary .....	123
6. Diffraction Imaging for Hard Rock Environments .....	125
6.1. Diffraction Imaging .....	125
6.2. D-volumes and Steered Migration .....	127
6.3. Synthetic Data Example.....	131
6.4. Field Example 1 – O’Callaghans Mine Site.....	134
6.5. Field Example 2 – Hillside Mine Site .....	141
6.6. Field Example 3 – Solwara Mine Site .....	146
6.7. Diffraction Imaging Summary .....	150
7. Discussions, Conclusions and Future Outlook.....	152

7.1. Seismic Imaging in Hard Rock Environments.....	152
7.2. Future Research of Seismic Imaging in Mineral Exploration.....	155
References .....	158

## Table of Figures

*Figure 2.1. Models of banded iron formation deposition a) chemical reaction of dissolved  $Fe^{2+}$  with oxygen produced by cyanobacteria; b) oxidation of  $Fe^{2+}$  by ultraviolet light; c) oxidation of  $Fe^{2+}$  by anoxygenic phototrophic bacteria (Reitner and Thiel, 2011). ..... 28*

*Figure 2.2. Diversity of settings of IOCG deposits. The thicknesses of arrows indicate the relative contributions of various fluids (Chen, 2013). ..... 29*

*Figure 2.3. Diagram of the modern Trans-Atlantic Geothermal sulfide deposit, representing a cross section of a VMS deposit with concordant semi-massive to massive sulfide lens underlain by a discordant stockwork vein system and associated alteration halo (Shanks and Thurston, 2012). ..... 31*

*Figure 2.4. General setting of porphyry copper and associated deposit types. Diagram shows interrelationships of different types of porphyry deposits and host rocks as well as the temporal sequence of rock types. (Sillitoe, 2010). ..... 33*

*Figure 2.5. Schematic representation of orogenic deposits in terms of depth formation and structural settings (Groves et al., 1998). ..... 35*

*Figure 2.6. Tectonic settings of the MVT deposits. The foreland basin filled with sediment is creating hydrologic conditions appropriate for generating the MVT mineralization (Leach et al., 2010a). ..... 37*

*Figure 2.7. Depth of cover on mineral discoveries in Australia (1950 – 2012) Analysis excludes Bulk minerals, and is limited to Moderate, Major and Giant deposits only (Major defined as > 1 million ounce Au, >100 kt, Ni, >1 Mt Cu. Giant is >5 Mt Cu-equivalent and Supergiant >25 Mt Cu-equivalent). Satellite deposits supply ore to a central mill within an existing mining camp. (Schodde, 2012) ..... 40*

*Figure 3.1. P-wave velocity versus density at confining pressure of 200 MPa for common hard rocks. Light grey is the Nafe-Drake curve. Lines for constant acoustic impedance for felsic ( $Z = 17.5 \cdot 10^5 \text{ g/cm}^2\text{s}$ ) and mafic rocks ( $Z = 20 \cdot 10^5 \text{ g/cm}^2\text{s}$ ) and the minimum reflection coefficient (R) required to produce strong reflection are shown for reference. Abbreviations: Py – pyrite, Sp – sphalerite, Ccp – chalcopyrite, Po – pyrrhotite, Pn – pentlandite, Gn – galena, g – gangue, Mgt – magnetite, Hem – hematite (Salisbury et al., 2003). ..... 48*

<i>Figure 3.2. Incident P-wave at an oblique angle to the plane interface and generated P- and S-waves (Yilmaz, 2001).</i> .....	51
<i>Figure 3.3. The Rayleigh's and Ricker's limits of vertical resolution (Kallweit and Wood, 1982).</i> .....	53
<i>Figure 3.4. The First Fresnel Zone (Yilmaz, 2001).</i> .....	54
<i>Figure 3.5. Rayleigh wave displacements with dimensionless depth (Cuellar, 1997).</i> .....	56
<i>Figure 3.6. Principle of seismic refraction method. Trave-time curves of direct wave (green) and refracted arrivals (red) are shown. Critically refracted waves start arriving after critical distance <math>x_{crit}</math>, and overtake the direct waves at a crossover point <math>x_{cross}</math>.</i> .....	58
<i>Figure 3.7. Basic principle of reflection seismic. Travel-time curve of the reflected wave from a horizontal interface is shown (green).</i> .....	61
<i>Figure 3.8. Migration principle. Geometrical consideration of migration of a dipping reflector (Bancroft, 2007).</i> .....	63
<i>Figure 3.9. Basic principle of the diffractions. 2D models and computed seismic records for coincident sources and receivers. a) Diffraction from the truncated interface (edge diffraction). b) Diffraction from the scatter point (sharp obstacle) (Torey, 1970).</i> .....	66
<i>Figure 4.1. Location of the seismic survey at the Hillside mine site (South Australia). Red and blue lines represent the position of a 2D seismic line with 1 m and 2 m geophone spacing, respectively. Green box shows the position of the mini-3D seismic survey (Images provided by Google Earth 2011).</i> .....	69
<i>Figure 4.2. Aeromagnetic survey of the Hillside camp. Line spacing of the magnetic survey is 25 m. Purple lines identify mineralized fault zones.</i> .....	70
<i>Figure 4.3. Seismic acquisition at Hillside camp. Left panel: EX-6 unit. Right panel: Accelerated weight drop on a trolley.</i> .....	72
<i>Figure 4.4. 2D Survey geometries. (A) Geometry of Line 1 (1 m geophone spacing); (B) Geometry of Line 2 (2 m geophone spacing).</i> .....	73
<i>Figure 4.5. Examples of five 2D raw shot gathers of Line 1 and an example of amplitude spectrum of the first shot gather.</i> .....	74

<i>Figure 4.6. Example of dispersion curves of slowness for both types of geometry: a) 1 m geophone spacing and b) 2 m geophone spacing.....</i>	<i>75</i>
<i>Figure 4.7. S-Velocity section for 1 m geophone spacing line.....</i>	<i>76</i>
<i>Figure 4.8. S-Velocity section for 2 m geophone spacing line.....</i>	<i>76</i>
<i>Figure 4.9. Time curves and inversion results of refraction wave's analysis. a) For 1 m geophone spacing geometry; b) For 2 m geophone spacing geometry. ....</i>	<i>78</i>
<i>Figure 4.10. Refraction data analysis results for two lines. Red and green lines correspond to the bottom of the first layer; blue and black lines correspond to the top of the third layer.....</i>	<i>79</i>
<i>Figure 4.11. Refraction interfaces and S-velocity section for 1m geophone spacing geometry. Red line represents the bottom of the first soil layer; blue line shows the top of the third metasediment layer.....</i>	<i>80</i>
<i>Figure 4.12. Refraction interfaces and s-velocity section for 2 m geophone spacing geometry. Red line represents the bottom of the first soil layer.....</i>	<i>80</i>
<i>Figure 4.13. Geological section of the regolith structure obtained from seismic data. ....</i>	<i>81</i>
<i>Figure 4.14. a) Shear wave profile obtained from MASW and b) P-wave velocity obtained from refraction tomography (Yavuz et al., 2012).....</i>	<i>81</i>
<i>Figure 5.1. Horizontal slownesses <math>p_r</math> and <math>p_s</math>. S is a shot point, R is a receiver location, A is a reflection point. ....</i>	<i>85</i>
<i>Figure 5.2. Geometry set up. S is a source location, R is a receiver location, A is a reflection point. ....</i>	<i>86</i>
<i>Figure 5.3. Convolution model of a dipping interface. a) True position of a dipping interface in time scale and b) example of a shot gather at 1000 m. ....</i>	<i>89</i>
<i>Figure 5.4. Horizontal slownesses for the model of a dipping interface. a) A semblances section for the shot gather at 1000 m, b) a section of <math>p_r</math> – values for the shot gather at 1000 m and c) a section of <math>p_s</math> – values for the shot gather at 1000 m.</i>	<i>90</i>
<i>Figure 5.5. Migration attributes for the model of a dipping interface. a) A migrated <math>x</math> coordinate attribute for the shot gather at 1000 m, b) a migrated <math>t_0</math> attribute for the shot gather at 1000 m and c) a migrated velocity attribute for the shot gather at 1000 m.....</i>	<i>91</i>

Figure 5.6. Migration results of the convolution model of a dipping interface. a) Migrated image of an interface of noise-free data (25 m radius and 5 time samples window for slopes estimation). b) Velocity distribution along the dipping reflector (shown only velocities at locations to which more than 15 samples contribute from different input traces). ..... 92

Figure 5.7. Convolution model of a dipping interface of data with 30% noise level. a) Example of a shot gather at 1000 m, b) a semblances section for the shot gather at 1000 m, c) a section of  $p_r$  – values for the shot gather at 1000 m and d) a section of  $p_s$  – values for the shot gather at 1000 m. (25 m radius and 5 time samples window for slopes estimation). ..... 93

Figure 5.8. Migration attributes for the model of a dipping interface of data with 30% noise level (25 m radius and 5 time samples window for slopes estimation). a) Amigrated  $x$  coordinate attribute for the shot gather at 1000 m (Figure 5.3a), b) a migrated  $t_0$  attribute for the shot gather at 1000 m (Figure 5.3a), and c) a migrated velocity attribute for the shot gather at 1000 m (Figure 5.3a). ..... 94

Figure 5.9. Migration results of the convolution model of a dipping interface of data with 30% noise level (25 m radius and 5 time samples window for slopes estimation). a) Migrated image of an interface of data with 30% noise level. b) Velocity distribution along the dipping reflector (shown only velocities at locations to which more than 15 samples contribute from different input traces). ..... 94

Figure 5.10. Horizontal slownesses for the model of a dipping interface of data with 30% noise level (75 m radius and 15 time samples window for slopes estimation). a) A semblances section for the shot gather at 1000 m, b) a section of  $p_r$  – values for the shot gather at 1000 m and c) a section of  $p_s$  – values for the shot gather at 1000 m. 96

Figure 5.11. Migration attributes for the model of a dipping interface of data with 30% noise level (75 m radius and 15 time samples window for slopes estimation). a) A migrated  $x$  coordinate attribute for the shot gather at 1000 m (Figure 5.3a), b) a migrated  $t_0$  attribute for the shot gather at 1000 m (Figure 5.3a and. c) a migrated velocity attribute for the shot gather at 1000 m (Figure 5.3a). ..... 97

Figure 5.12. Migration results of the convolution model of a dipping interface of data with 30% noise level (75 m radius and 15 time samples window for slopes estimation). a) Migrated image of an interface of data with 30% noise level. b)

*Velocity distribution along the dipping reflector (shown only velocities at locations to which more than 15 samples contribute from different input traces). . . . . 97*

*Figure 5.13. Convolution model of a syncline. a) True position of a syncline in time scale and b) example of a shot gather at 1000 m. . . . . 98*

*Figure 5.14. Convolution model of a syncline. a) Energy distribution from the unit amplitude syncline model. Shown how many points are coming from the input data to a certain location on the image. True slopes were used for the migration, b) a semblance section for the shot gather at 1000 m, c) a section of  $p_r$  – values for the shot gather at 1000 m and d) a section of  $p_s$  – values for the shot gather at 1000 m. 99*

*Figure 5.15. Migration attributes for the model of a syncline. a) A migrated  $x$  coordinate attribute for the shot gather at 1000 m, b) a migrated  $t_0$  attribute for the shot gather at 1000 m and c) a migrated velocity attribute for the shot gather at 1000 m. . . . . 100*

*Figure 5.16. Migration results of the convolution model of a syncline. a) Migrated image of a syncline of noise-free data (25 m radius and 5 time samples window for slopes estimation). b) Velocity distribution along the syncline (shown only velocities at locations to which more than 15 samples contribute from different input traces). . . . . 100*

*Figure 5.17. Convolution model of a syncline of data with 30% noise level. a) Example of a shot gather at 1000 m, b) a semblance section for the shot gather at 1000 m, c) a section of  $p_r$  – values for the shot gather at 1000 m and d) a section of  $p_s$  – values for the shot gather at 1000 m. (25 m radius and 5 time samples window for slopes estimation). . . . . 101*

*Figure 5.18. Migration attributes for the model of a syncline of data with 30% noise level (25 m radius and 5 time samples window for slopes estimation). a) A migrated  $x$  coordinate attribute for the shot gather at 1000 m (Figure 5.17a), b) a migrated  $t_0$  attribute for the shot gather at 1000 m (Figure 5.17a) and c) a migrated velocity attribute for the shot gather at 1000 m (Figure 5.17a). . . . . 102*

*Figure 5.19. Migration results of the convolution model of a syncline of data with 30% noise level (25 m radius and 5 time samples window for slopes estimation). a) Migrated image of a fold of data with 30% noise level. b) Velocity distribution along*

<i>the syncline (shown only velocities at locations to which more than 15 samples contribute from different input traces).</i> .....	102
<i>Figure 5.20. Horizontal slownesses for the model of a syncline of data with 30% noise level (75 m radius and 15 time samples window for slopes estimation). a) A semblance section for the shot gather at 1000 m (Figure 5.17a), b) a section of <math>p_r</math> – values for the shot gather at 1000 m (Figure 5.17a) and c) a section of <math>p_s</math> – values for the shot gather at 1000 m (Figure 5.17a).</i> .....	103
<i>Figure 5.21. Migration attributes for the model of a syncline of data with 30% noise level (75 m radius and 15 time samples window for slopes estimation). a) A migrated <math>x</math> coordinate attribute for the shot gather at 1000 m (Figure 5.17a), b) a migrated <math>t_0</math> attribute for the shot gather at 1000 m (Figure 5.17a) and c) a migrated velocity attribute for the shot gather at 1000 m (Figure 5.17a).</i> .....	104
<i>Figure 5.22. Migration results of the convolution model of a syncline of data with 30% noise level (75 m radius and 15 time samples window for slopes estimation). a) Migrated image of a fold of data with 30% noise level. b) Velocity distribution along the syncline (shown only velocities at locations to which more than 15 samples contribute from different input traces).</i> .....	104
<i>Figure 5.23. Migrated sections of the syncline model with unit amplitudes. Colours show the energy distribution from the unit amplitude syncline model. Shown how many points are coming from the input data to a certain location on the image. a) Image from true values of local slopes for migration. b) Image from 10% overestimated values of local slopes for migration. c) Image from 10% underestimated values of local slopes for migration. d) Image from random distribution of 10% errors in values of local slopes for migration.</i> .....	106
<i>Figure 5.24. 2D hard rock velocity model, which was used to generate a synthetic seismic dataset. (rock type letters are defined in Table 1)</i> .....	108
<i>Figure 5.25. 2D hard rock velocity model converted to time domain.</i> .....	109
<i>Figure 5.26. 2D section of the RMS velocities.</i> .....	109
<i>Figure 5.27. 2D synthetic geological model. Shot gather at 5500 m. a) A semblance section, b) a section of <math>p_r</math> – values and c) a section of <math>p_s</math> – values.</i> .....	110

<i>Figure 5.28. 2D synthetic geological model. Shot gather at 5000 m. a) A migrated <math>x</math> coordinate attribute, b) a migrated <math>t_0</math> attribute and c) a migrated velocity attribute.</i>	111
<i>Figure 5.29. Section of the migration velocities.</i>	112
<i>Figure 5.30. The final image of the prestack time migration from the 2D hard rock geology model.</i>	112
<i>Figure 5.31. The prestack migration image from the 2D hard rock geology model. Actual velocity model is overlaid onto the migrated section.</i>	113
<i>Figure 5.32. Kirchhoff PSTM image from the 2D hard rock synthetic model. Migration velocities from the presented migration were used as an input velocity model.</i>	114
<i>Figure 5.33. Kirchhoff PSTM image from the 2D hard rock synthetic model. Migration velocities from the presented migration were used as an input velocity model. Actual velocity model is overlaid onto the migrated section.</i>	115
<i>Figure 5.34. 2D stacking velocity model, which was obtained from a velocity analysis after applying DMO corrections.</i>	116
<i>Figure 5.35. Kirchhoff PSTM image from the 2D hard rock synthetic model. Stacking velocities from the velocity analysis were used as an input velocity model.</i>	117
<i>Figure 5.36. Kirchhoff PSTM image from the 2D hard rock synthetic model. Stacking velocities from the velocity analysis were used as an input velocity model. Actual velocity model is overlaid onto the migrated section.</i>	117
<i>Figure 5.37. Location of the 2D seismic line SI-NJI (North Junction) – red line. The St. Ives gold camp in Western Australia. Yellow and green lines are 2D seismic profiles. (Harlan et al., 1983; Stolz et al., 2004).</i>	120
<i>Figure 5.38. Processed shot records from the SI-NJI (North Junction) seismic line.</i>	121
<i>Figure 5.39. Smoothed velocity model of the SI-NJI (North Junction) seismic line. St Ives mining camp.</i>	122
<i>Figure 5.40. Migrated section of the SI-NJI (North Junction) seismic line. St Ives mining camp.</i>	123

<i>Figure 6.1. Diffraction (yellow hypersurface) and reflection (blue celled surface) travel time surfaces. Tangent contact of the diffraction surface to the reflection surface is shaded in light blue.....</i>	<i>128</i>
<i>Figure 6.2. Selection of the travel time surface portion for the semblance calculation (plane view) (2D projection of Figure 6.1). <math>\alpha</math> is a horizontal azimuth, <math>h</math> is a lateral offset, the dashed line is where the diffraction travelttime is split for phase change. ....</i>	<i>130</i>
<i>Figure 6.3. Cross-line section of the model for the generated synthetic data set....</i>	<i>132</i>
<i>Figure 6.4. (a) Noise free cross-line section of the synthetic dataset. (b) The same section after adding 50% of random noise. ....</i>	<i>133</i>
<i>Figure 6.5. Comparison of the standard Kirchhoff migration and the steered Kirchhoff migration of the 3D synthetic data with 50% of random noise. (a) Time-slice (500 ms) of the standard Kirchhoff migration. (b) Time-slice (500 ms) of the steered Kirchhoff migration. (c) Cross-section of the standard Kirchhoff migration. (d) Cross-section of the steered Kirchhoff migration. The steepest interfaces with <math>50^\circ</math> and <math>60^\circ</math> slopes are highlighted on the cross-sections in red and blue circles, respectively.....</i>	<i>134</i>
<i>Figure 6.6. Location of the 3D seismic survey at the O'Callaghans mine site (Western Australia) (Images provided by Google Earth 2011). ....</i>	<i>135</i>
<i>Figure 6.7. Comparison of a vertical slice (xline 88) of the 3D seismic volume obtained with (a) standard Kirchhoff migration and (b) steered Kirchhoff migration. Red circles highlight improvement of imaging the dome's flanks. ....</i>	<i>138</i>
<i>Figure 6.8. Comparison of time-slice (178 ms) of the 3D seismic volume obtained with (a) standard Kirchhoff migration, (b) steered Kirchhoff migration and (c) diffraction imaging technique (D-volume).....</i>	<i>139</i>
<i>Figure 6.9. (a) A point-star at the time slice 178 ms, located at in-line 72 and cross-line 25 and (b) the maximum semblance values of that point as a function of azimuth indicating the orientation of the diffraction object. The maximum semblance values show the direction of the possible fault.....</i>	<i>140</i>
<i>Figure 6.10. Steered Migration Section (Xline 88). Geological interpretation is overlaid onto the migrated image. Red lines are faults. ....</i>	<i>141</i>

<i>Figure 6.11. Location of the 3D seismic survey at the Hillside mine site (South Australia) and a CDP fold map of the survey (Images provided by Google Earth 2011).</i> .....	142
<i>Figure 6.12. a) Example of steered migrated 3D seismic cube with the interface of the regolith overburden. b) Map of the bottom of the weathered regolith layer. ....</i>	144
<i>Figure 6.13. Time-slices at 120 ms of D-volumes with an indication of main linear geological features. a) The computed D-volume with taking into account the phase-reversal phenomenon. b) The computed D-volume without phase reversal. The area with presence of gabbro intrusions is circled in blue. ....</i>	146
<i>Figure 6.14. Location of the Solwara 1 site. Main tectonic elements and structures of the Manus Basin region (Moss and Scott, 2001) (Image provided by Google Earth 2011).</i> .....	147
<i>Figure 6.15. In-line 150 of the Solwara 1 3D seismic volume. a) Kirchhoff migration. b) D-volume section. Concentrations of diffraction energy along linear features, which are unseen on the Kirchhoff image, are circled blue in the section .....</i>	149
<i>Figure 6.16. Time-slices at 2528 ms of the Solwara 1 3D seismic volume. a) Kirchhoff migration. b) Steered migration.....</i>	150

## Table of Tables

<i>Table 1. Velocity-Density table for the 2D geology model. ....</i>	108
<i>Table 2. Acquisition parameters for the SI-NJI (North Junction) seismic line. ....</i>	121
<i>Table 3. Acquisition parameters used for the 3D seismic surveys acquired at O'Callaghans mine site. ....</i>	136
<i>Table 4. Acquisition parameters used for the 3D seismic surveys acquired at Hillside mine site. ....</i>	143

# 1. Introduction

## *1.1. Hard Rock Seismic Imaging*

The mining is an important and integral part of the Australian economy. Steady productivity and growth of the mineral industry has largely relied on discoveries of new mineral provinces and deposits and expansion of present mining prospects. Geophysical methods play a significant role in the mineral exploration process. Traditionally, in the mining industry geophysical mineral exploration has been conducted using potential field methods, and electromagnetic (EM) surveys. These techniques are based on using the contrast in physical properties of mineral deposits (e.g., enhanced conductivity, chargeability, or magnetization) to detect them. These exploration techniques have historically been utilized to locate surface or shallow prospective targets for exploration drilling. They are appropriate for shallow (< 200 m) exploration tasks, but have limitations in spatial and depth resolution, and lose their sensitivity in the presence of substantial regolith overburden. Uncovering deep targets requires the geophysical techniques with high spatial and depth resolution. To this end, deep exploration increasingly involves the seismic methods in hard rock mineral prospecting.

The seismic methods have the highest resolution among surface geophysical technologies, and utilise many reliable imaging techniques. Properly acquired seismic data can image subsurface geological strata and objects, and also define structures, lithological units and fluid content of reservoirs. At the present time, reflection seismic technologies play an important role in oil and gas exploration and have the leading role in identifying hydrocarbon deposits in sedimentary basins. These methods are utilized to build 3D geological models of oil and gas reservoirs and monitor production processes. Despite the successful applications of surface seismic in sedimentary environments, these methods are not widespread in the mineral industry. One of the reasons is the high cost of seismic surveys in comparison with conventional (electromagnetic and potential) geophysical methods. Another is that the application of seismic methods is facing a number of difficulties

in hard rock environments due to complex and inhomogeneous structure of these media.

Hard rock camps comprise igneous and metamorphic rocks and often have rather complex geological structure, which includes a lot of reverse and relaxation faults, shear and fracture zones, steep dips, granite intrusions with surrounded alterations etc. Such environments are also often characterized by rugged topography and complex near-surface situations. These circumstances could lead to different and unstable conditions for generating and recording of seismic waves. The weathered regolith overburden (which could be >100 m thick) causes attenuation of the seismic signal by distorting, scattering and absorbing seismic energy. Seismic exploration surveys are often acquired around active mine sites, where constant machinery's movements produce a high level of ambient noise. Because of these reasons, the field data could have an anomalously low signal-to-noise ratio that may affect the quality of final subsurface images. In general, hard rock media have high seismic velocities, which translate to long wavelengths; this can also affect seismic resolving power, because often the seismic acquisitions are carried out with an insufficient frequency range. All of these difficulties and a complex geology make seismic imaging in hard rock environments rather challenging.

Seismic migration (imaging) techniques enable us to produce 2D and 3D images of geological structures and reveal location, size, and thickness of mineral targets. Most of the conventional seismic migrations need a velocity model for a geological section. In sedimentary environments, where boundaries between the layers are usually horizontal and continuous, velocities could be calculated directly from seismic data. However, in hard rock conditions, there are many steep dips and sustained boundaries are lacking, and the estimation of velocities becomes a nontrivial problem. Acoustic logs and full waveform sonic logs, which provide important information about the wave propagation velocities, are typically not acquired during mining exploration. These factors impose additional challenges for seismic imaging in hard rock environments.

All described features of mining seismic exploration do not allow an easily transferable conventional imaging algorithm from oil and gas seismic to obtain

proper geological models for mineral deposits. Modification of known seismic migration methods and development of new imaging approaches should be implemented to meet the needs of the mining industry.

Complete understanding of mineral prospecting site structures requires investigation at both shallow and deep depths. Research of the deep Earth strata is necessary to identify the main hydrothermal fluid conduits and reveal the structure of mineral systems, while exploration of shallower parts detects fault and shear zones, where mineral and ore accumulations can occur; exploring the near surface altering regolith cover is also important for mine planning. In order to achieve mineral targeting at any geological level seismic methods collect information about propagation of different types of waves (compressional, shear and surface waves) through the media and analyse refracted, reflected and diffracted responses from subsurface formations.

The availability of reliable models of complex hard rock structures helps estimate reserves of ore and mineral deposits and enables effective production. To overcome ambiguities on seismic images, they should be calibrated through surface geology and mine interpretations. The development of robust imaging algorithms for mining environments will improve seismic abilities to target the new discoveries of mineral deposits and make seismic exploration more cost effective.

### ***1.2. Research Objectives***

The main objectives of this research are to investigate seismic imaging techniques in order to address challenges that are facing the seismic method in hard rock environments and to improve the application of seismic tools for mineral exploration tasks.

Research involves studies of different seismic tools including analysis of surface waves, refraction waves, reflections and diffraction energy in application to hard rock environments. Exploration tasks in the mining industry are highly diverse and embrace shallow and deep depths, various geological complexities, different types of mineral deposits (layered, separate bodies, disseminated, confined to faults, etc.). In

order to satisfy targeting tasks the research covers several seismic imaging techniques.

The overall objectives consist of the following parts:

- Imaging of the regolith structure by using surface and refraction waves analysis – cost effective near surface seismic field survey;
- 2D velocity independent prestack seismic migration algorithm. Simultaneous velocity estimation and time seismic imaging of mineral formations. Testing the algorithm on synthetic models and field datasets;
- 3D poststack diffraction imaging algorithm for data with a poor signal to noise ratio. Delineation of subvertical geological structures and faults. Testing the algorithm on a synthetic model and field data from various regions.

### ***1.3. Thesis Structure***

The thesis is organized into seven chapters. The significance of the new imaging algorithms for hard rock seismic exploration and objectives for this research are summarized in Chapter 1. Chapter 2 provides a brief overview of the main important types of mineral deposits for the Australian mining industry. The chapter contains a description of geological settings and highlights features for each type. The expected trends in new deposit discoveries are stated at the end of the chapter. Chapter 3 comprises information regarding historical and current applications of seismic methods for hard rock exploration. General knowledge and basic concepts of seismic waves and tools, and discussion of the physical rock properties are explained in the chapter.

Chapter 4 includes the field example of near surface seismic imaging of the weathered cover structure at the Hillside mine camp using surface and refracted waves. Chapter 5 contains the methodology of the velocity independent prestack time migration algorithm. The chapter describes the implementation of the approach and its application to synthetic models; the comparison with the conventional migration is shown in the chapter as well. The last part of chapter 5 shows the

application of the imaging method to the field seismic data from St Ives mine site. The developed diffraction steered migration is presented in Chapter 6. The chapter provides the methodology of the algorithm and the testing on a synthetic model. The application to two surface seismic datasets from South and Western Australia mine camps and to marine seismic volume from the Bismarck Sea region are completed in Chapter 6.

The final discussions, conclusions and recommendations of my research are outlined in Chapter 7. A full list of cited references then completes this thesis.

## **2. Australian Mineral Resources**

### ***2.1. Australian Mineral Deposits***

The mining sector in Australia is a substantial primary industry. The mining industry is a significant contributor to the Australian economy and it has a large impact in many social and environmental areas in the country. Australia is one of the largest mineral producers of the world's key minerals commodities. In 2011 Australia was ranked as the top producer of bauxite, alumina, rutile, and zircon; and had the second largest production rate of gold, zinc, lead, and manganese ore (McKay et al., 2013). Australia has the largest economic resources of gold, iron ore, nickel, uranium, zinc, lead and silver (McKay et al., 2013).

Several dozen types of mineral deposits of economic importance exist in Australia in old and young rocks in a great variety of geological situations. Such diversity of ore deposit types exists due to a complex interaction of several factors: presence of an ore components source, transport mechanism of these elements, mechanism of precipitation and accumulation of the components in a mineral site, and appropriate settings to preserve the minerals. Formation of the mineral systems involves many geological and geodynamic factors that control the initiation, evolution and conservation of ore deposits (Pirajno and Bagas, 2008). The classification of the mineral deposits can be done based on elements composition, form, genesis, associated host rock and geological structures.

Generally, ore deposits are broadly divided into two categories: syngenetic – mine fields formed simultaneously with surrounding rocks; epigenetic – ore bodies introduced into pre-existing host rocks. The structure and geometry of the mineral deposits are often related to genesis processes. Syngenetic deposits are usually associated with a specific stratigraphic formation or can be layered and correlated with certain stratigraphy (McQueen, 2005). Epigenetic deposits are often confined to intrusive bodies; the hydrothermal deposits reflect the geometry of the fluid pathways, and commonly formed veins or elongated along fracture zones. Comprehensive knowledge of the form and structure of a mineral deposit provides

important information not only for a resource estimation and production design but can be used as a pathfinder for new discoveries.

In many cases the ore deposits are described as an association of a particular ore type with certain enclosing rock. The rock interaction within such complexes reflects the formation processes of the deposits (McQueen, 2005). The physical and chemical properties of the ore minerals and the host rocks within associations often vary greatly. The contrast in physical properties such as density, conductivity, magnetic susceptibility, velocity and radiometric signature provide the capability of using geophysical methods to explore mineral deposits. The following sections provide a general overview of the most economically important types of mineral deposits in Australia.

### **2.1.1. Banded Iron Formation (BIF)**

Banded Iron Formations are the most valuable source for significant economic iron ore deposits. Giant deposits of BIF occur in Australia, South Africa, Brazil, and Russia. These formations are usually associated with Precambrian (Archean to earliest Paleoproterozoic successions) sedimentary sequences and contain shales, dolomites and volcanic mafic rocks, which correspond to marine shelf lithological sequences. The global accumulation of BIFs in Precambrian time took place due to a combination of factors: the presence of a large supply of iron in ocean water from hydrothermal sources, developing of wide continental shelves to store the deposits, and a stratified ocean to connect the first two factors (Clout and Simonson, 2005). The main aspects of the iron origin and depositional mechanisms of the ore elements are still debated. Models of banded iron formation deposition include: the traditional mode, when hydrothermal dissolved  $\text{Fe}^{2+}$  chemically react with oxygen in the water column, which has been produced by cyanobacteria (Figure 2.1a); the abiotic mechanism in an anoxic ocean when oxidation of  $\text{Fe}^{2+}$  caused by ultraviolet light (Figure 2.1b); and the direct microbial model, which is also taking place in an anoxic water column when  $\text{Fe}^{2+}$  oxidation occurs via anoxygenic phototrophic bacteria (Figure 2.1c) (Reitner and Thiel, 2011).

There are two types of Precambrian iron formations related to their depositional environments. Archaean (or Algoma) type iron formations are interbedded with or stratigraphically connected to abyssal erupted volcanic rocks and sometimes with volcanogenic massive sulfide (VMS) deposits. The second Superior-type iron formations type are formed in passive-margin sedimentary basins and commonly do not interact with volcanic rocks (Bekker et al., 2010). In Australia, the well known Hamersley basin has the most extensional Precambrian banded iron formations; and contains the largest resources of iron ore in the world.

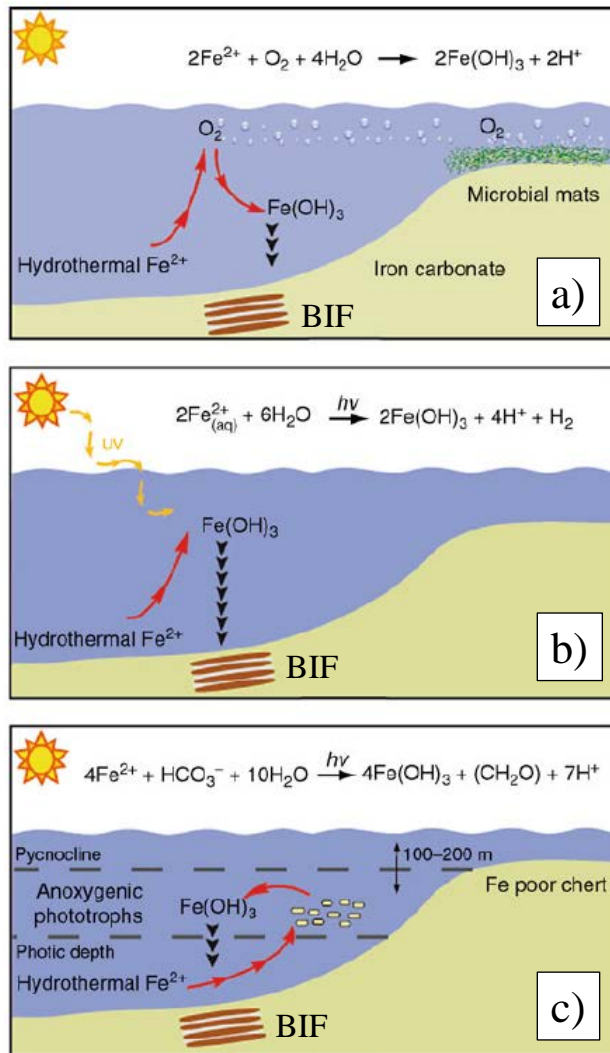


**Figure 2.1. Models of banded iron formation deposition a) chemical reaction of dissolved  $Fe^{2+}$  with oxygen produced by cyanobacteria; b) oxidation of  $Fe^{2+}$  by ultraviolet light; c) oxidation of  $Fe^{2+}$  by anoxygenic phototrophic bacteria (Reitner and Thiel, 2011).**

The mining exploration is based on high-grade iron ore (up to 65% Fe) BIFs. These types of formations are subsequently enriched with iron (Pirajno and Bagas, 2008). The location and geometry of such iron ore deposits are mainly controlled by structures (Dalstra and Rosière, 2008).

## 2.1.2. Iron-Oxide-Copper-Gold (IOCG) Deposits

The appearance of IOCG type ore deposits arose straight after the discovery in 1975 of the world-class Olympic Dam breccia-hosted iron oxide copper-gold deposit in South Australia. The term IOCG was suggested by Hitzman et al. (1992) and has become associated with many diverse ore systems. This classification is based on an empirical definition stemming mainly from geochemical characteristics and does not define tectonic framework, geological settings, and sources of fluids and ore components. The IOCG deposits are the magmatic-hydrothermal systems and occur in a wide range of different surrounding rock associations primarily within plutonic granitoids, andesitic (meta)volcanic rocks, and (meta)siliclastic-metabasic rocks (Williams et al., 2005). Figure 2.2 shows the diversity of the alteration zoning, minerals domination and contributions of different fluid sources for a number of IOCG deposits around the world.

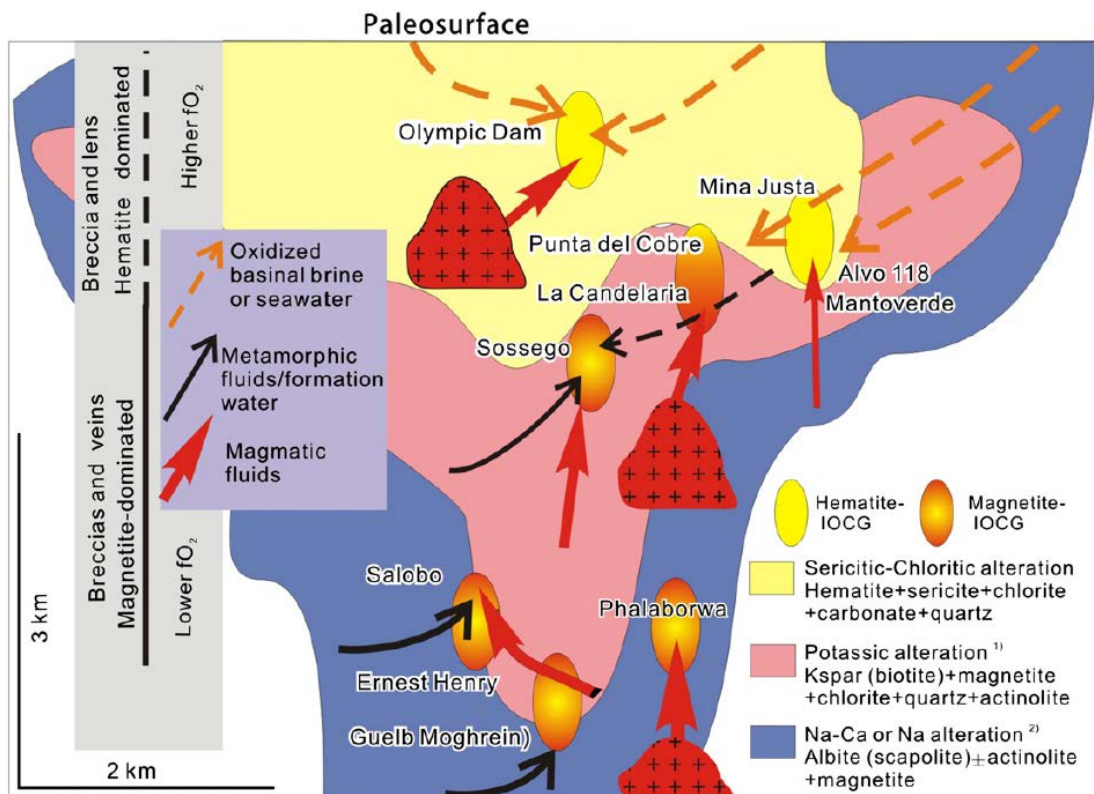


**Figure 2.2.** Diversity of settings of IOCG deposits. The thicknesses of arrows indicate the relative contributions of various fluids (Chen, 2013).

Despite the challenges in the clear classification of IOCG deposits due to their large variation in age, geochemical signature, mineralogy, host rocks, and local geologic settings, the relatively robust definition for economic concentrations of copper/gold can be applied. These deposits have to fulfil the following criteria: have copper and/or gold economic metals, be a hydrothermal ore style with strong structural control – mainly with breccias, are surrounded by alteration zones, have depleted silica concentration of altered wall rocks, have abundant low titanium iron oxides or iron silicates, and have a close temporal, but not spatial relationship with igneous intrusions (Groves et al., 2010). The IOCG districts are well controlled by structural and/or stratigraphic factors with ore occurrences typically confined to fault bends, shear zones, rock contacts, breccia bodies, or as lithology-controlled replacements (Williams et al., 2005).

This research involves the application of seismic techniques to the geological settings of the Hillside mine camp – the recent IOCG discovery located on the Yorke Peninsula (South Australia) – in order to study the capabilities of seismic methods to image subvertical structures and explore the regolith cover of the deposit.

### **2.1.3. Volcanogenic Massive Sulfide (VMS) Deposits**

Volcanogenic massive sulfide (VMS) deposits are significant global sources of copper, zinc, lead, gold, and silver. These types of mineral deposits are also known as volcanic-associated, volcanic-hosted, and volcano-sedimentary-hosted massive sulphide deposits. They form on, and immediately below the seafloor where discharging high temperature hydrothermal fluids are cooled through mixing with sea water or porewater in near-seafloor lithologies. This process occurs in association with synchronous volcanism and/or plutonism. The VMS deposits are commonly developed in extension tectonic environments, including both oceanic spreading zones and arc terranes. The age range is from the 3.4 Ga Archean Pilbara Block, Australia, to modern actively forming deposits (Galley et al., 2007).

VMS deposits are syngenetic and stratabound formations of massive to semi-massive sulphide. The deposits consist of two parts: a conformable massive sulphide lens (>60% sulphide minerals), and commonly underlain sulphide-silicate vein-type

mineralization zone. This subjacent vein system, the so-called stringer or stockwork zone, is surrounded by altered volcanic and/or sedimentary rocks (Figure 2.3). In some cases, the stratiform massive sulphide lens concentrates the entire economic ore resources, while in other deposits significant amount of ore can be mined from the stringer zone (Gibson et al., 2007).

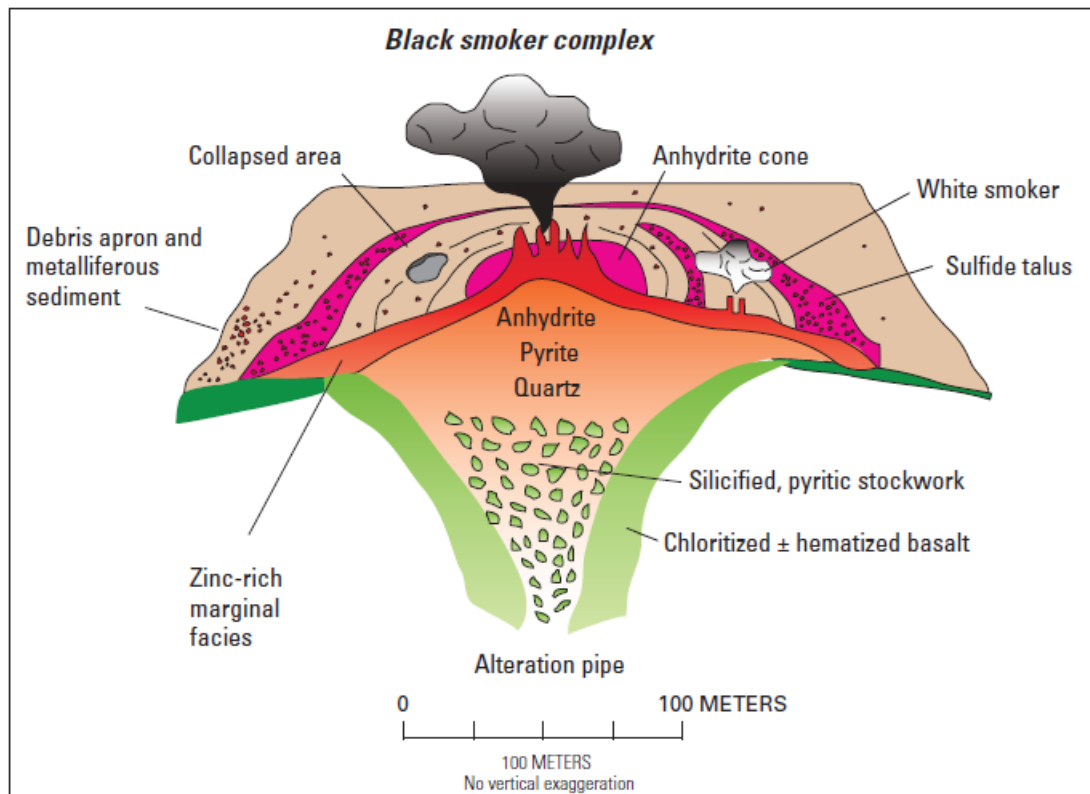


**Figure 2.3.** *Diagram of the modern Trans-Atlantic Geothermal sulfide deposit, representing a cross section of a VMS deposit with concordant semi-massive to massive sulfide lens underlain by a discordant stockwork vein system and associated alteration halo (Shanks and Thurston, 2012).*

In Australia, the VMS deposits are located within the submarine portion of volcanic belts. These belts consist of a number of complex volcanic centres with related volcanoclastic and epiclastic facies. The volcanic accumulations comprising the VMS deposits mainly consist of rhyolite (60-80% of pile) with lesser andesite, dacite, basalt and sediment. The major VMS districts have a thick rhyolitic underlying in the base of the volcanic sequence. This pile includes lavas, volcanoclastics and subvolcanic intrusives. The upper part of the volcanic succession represents a mixed

sequence of sediments and volcanics overlying the rhyolite pile. The massive sulphide deposits are usually confined to the base of overburden volcanic-sedimentary series or at the top of the basal rhyolite sequence (Large, 1992).

The plan view size of VMS deposits varies from tens of thousands of square meters to giant dimensions of several square kilometers. The form of VMS deposits may depend on the original hydrothermal geometry or on different post deformations such as folding, faulting, and shearing. In areas with minimal deformation, deposits can correspond to sheets, layers, lenses, mounds, pipes, and stockworks forms. In deformed zones the sulfide bodies can be complexly folded and dismembered. The diverse range of deposit morphologies, sizes and also compositions relies on the nature and duration of hydrothermal activity; topography of the sea bottom; footwall and host-rock lithology; temperature gradients; shearing, folding, and faulting and degree of erosional preservation (Shanks and Thurston, 2012).

The seafloor VMS deposits associated with ocean hydrothermal sites contain large amount of mineral resources. This study includes the investigation of the seismic diffraction imaging technique in application to marine data collected in the Bismarck Sea over a seabed VMS deposit.

#### **2.1.4. Porphyry Deposits**

The porphyry deposits are the largest source of copper in the world and significant storage of gold, molybdenum and silver. The porphyric systems have been mainly formed from Archean to Quaternary in age, with most known deposits developed in Cenozoic or Mesozoic eras (John et al., 2010). The porphyry districts are associated with subduction of submarine ridges and seamount chains, and oceanic plateaus beneath continental arcs. The porphyry deposits are generally related to shallow located intrusive complexes and underlying plutons and batholiths, where volcanic rocks have typically dioritic to granitic compositions. They consist of disseminated elements and minerals in veins and breccias that are rather equally distributed in large rock volumes, forming economic ores (John et al., 2010).

Porphyry systems are surrounded by different rock types such as igneous, sedimentary, and metamorphic rocks. The deposit grade can be raised by the presence of particular lithology of the hosted rocks. For instance, the concentration of high-grade ore can be formed in carbonate successions (especially like marble) or other fine-grained and low-permeable rocks that may seal a porphyry deposit all around. Lithologic clusters, which are rich in ferrous iron, also can assist in high-grade porphyry mineral accumulation (Sillitoe, 2010). Figure 2.4 shows general geological settings of porphyry deposits and their relationship with immediate host rocks.

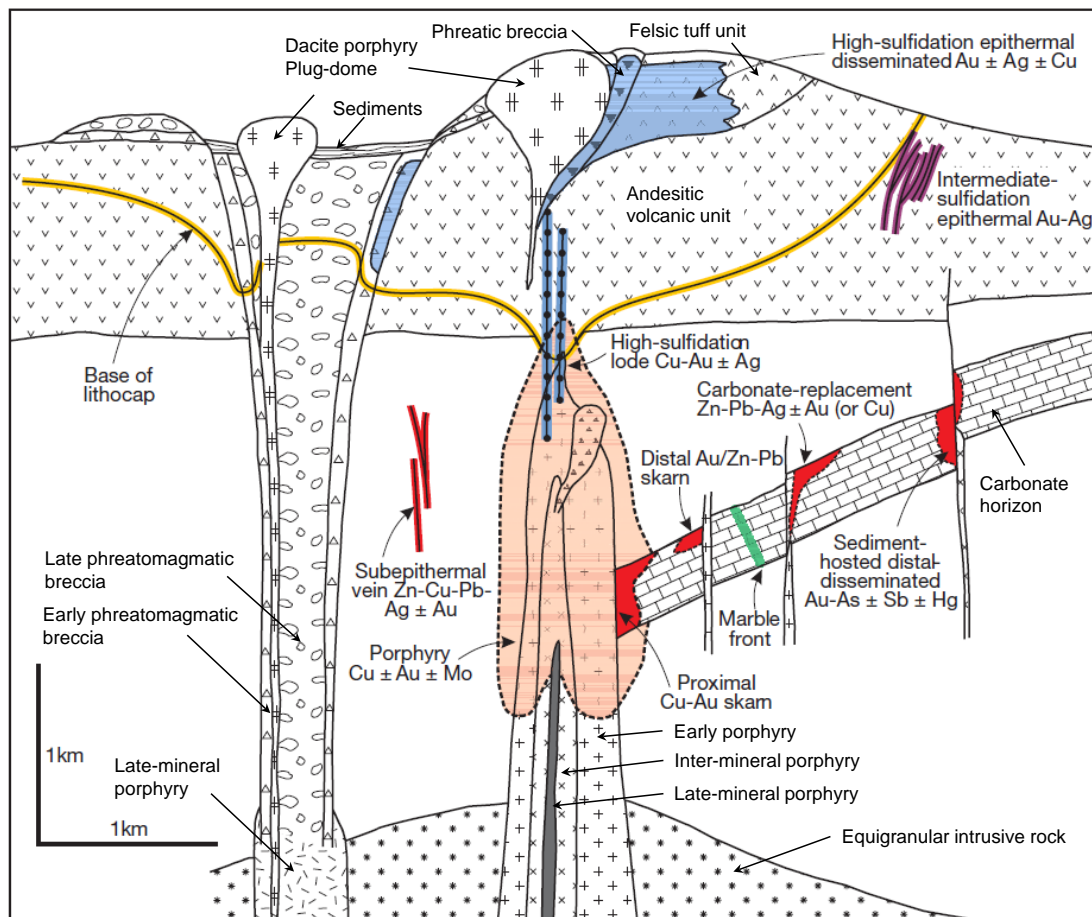


**Figure 2.4. General setting of porphyry copper and associated deposit types. Diagram shows interrelationships of different types of porphyry deposits and host rocks as well as the temporal sequence of rock types. (Sillitoe, 2010).**

The shape and plan view of the deposits normally reflects those of their host intrusions. The vertical stocks contain cylindrical ore bodies, whereas laterally

extended dike arrays show narrow and elongate shapes of ore mineralization. Generally diameters of stocks and lengths of dykes are around 1 km. Vertical extent of ore bodies is also approximately 1 km, but in several cases drilling has shown mineralized zones extended more than 2 km (Sillitoe, 2010). Configurations and dimensions of the porphyry deposits vary widely due to occurrences of post-ore intrusions, different types of host rocks, erosion processes, post-ore folding and faulting.

#### **2.1.5. Orogenic Gold Deposits**

Orogenic gold deposits contain over a quarter of world gold resources. These deposits were generated in circumstances of collision and mountain forming events over more than 3 billion years of the Earth's history. They have formed occasionally from the Middle Archean to younger Precambrian and during the whole Phanerozoic eon. Orogenic gold occurrences are associated with processes involving the flow of sulfur-bearing hydrothermal fluids transferring a considerable amount of the leachable gold through major fault networks and along migration paths. Eventually, gold precipitates in secondary and tertiary fault zones at shallow areas of uplifting orogens (Goldfarb et al., 2001). The mineralization zones commonly occur as lode and vein shape, and accumulate simultaneously with deformations in brittle and plastic structures. The orogenic deposits are commonly generated in the upper crust in accretionary belts adjoined to continental magmatic arcs during compressional/transpressional regimes (Figure 2.5).

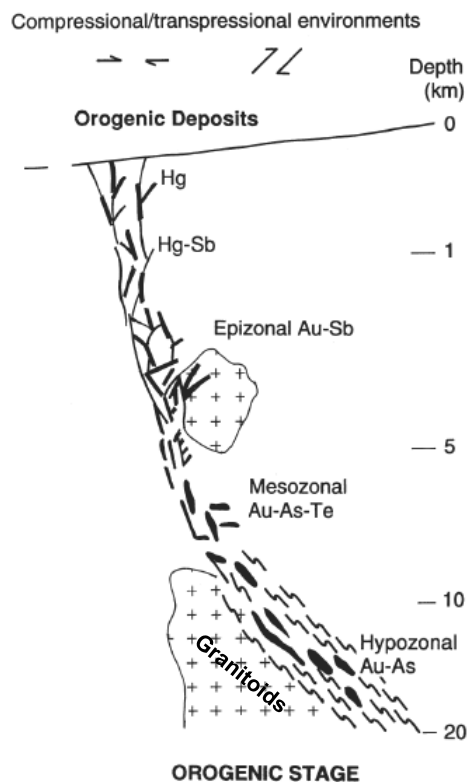


*Figure 2.5. Schematic representation of orogenic deposits in terms of depth formation and structural settings (Groves et al., 1998).*

The Yilgarn Craton of Western Australia is the largest Australian gold province. Most of the orogenic gold deposits (about 80 %) in this area are Archean (Cassidy and Hagemann, 2001). The gold mineralizations are hosted by different rock types such as banded iron-formation, felsic igneous rocks and sedimentary rocks, felsic-intermediate volcanoclastic rocks, rarely within granitoids, but the majority of gold camps are presented within mafic and ultramafic rocks (Witt and Vanderhor, 1998). Mainly, the gold deposits in this district are structurally controlled and there is a wide range of structural styles and occurrences in a variety of structural settings. The ore bodies are often associated with quartz veins, brittle faults, brittle-ductile shear zones and some strongly ductile shear zones. Most of the gold deposits are oriented and located in respect to the main regional east-west compressional deformation (along main regional shear zones), but the geometry and positions of individual veins within the particular camps may be varied and dependent on the local stress field variations (Witt and Vanderhor, 1998).

This research includes analysis of seismic data acquired to investigate one of the orogenic mineral deposits in the Yilgran Craton. The study shows an application of the velocity independent imaging technique to reveal geological settings from a 2D seismic line at St Ives mine camp.

#### **2.1.6. Mississippi Valley Type (MVT) Deposits**

The Mississippi Valley Type (MVT) mineral deposits are world important sources for zinc and lead. The economic resources of silver, barite, gypsum, and fluorite may also be found in these deposits. Most of the MVT deposits occur in Phanerozoic rocks and less than 20 percent in Precambrian host-rocks (Leach et al., 2010b). The MVT mineral districts are epigenetic and a product of regional fluid migration. They are accumulated by the migration of warm saline hydrous solutions through the underground reservoirs within carbonate formations, fluids temperature range is typically from 75 to 200°C (Leach et al., 2005). The MVT deposits are mainly located in carbonate platforms bordering the continental sedimentary basins. The surrounding rocks are generally dolomites or limestone; rarely deposits can be hosted in sandstones. This type of mineral deposits is not associated with igneous processes. The MVT deposits are usually generated in orogenic forelands; these areas have essential hydrological connection between platform carbonates and orogenic belts (Figure 2.6). Deposits are also common in foreland thrust belts, but occur less frequently in inner continental basins (Paradis et al., 2007). The key factor of the development of the MVT mineralization is lithological transformations, especially when large changes in the lateral and vertical penetration of carbonate successions have occurred. Such facies transitions are typically confined to reef and barrier environments.

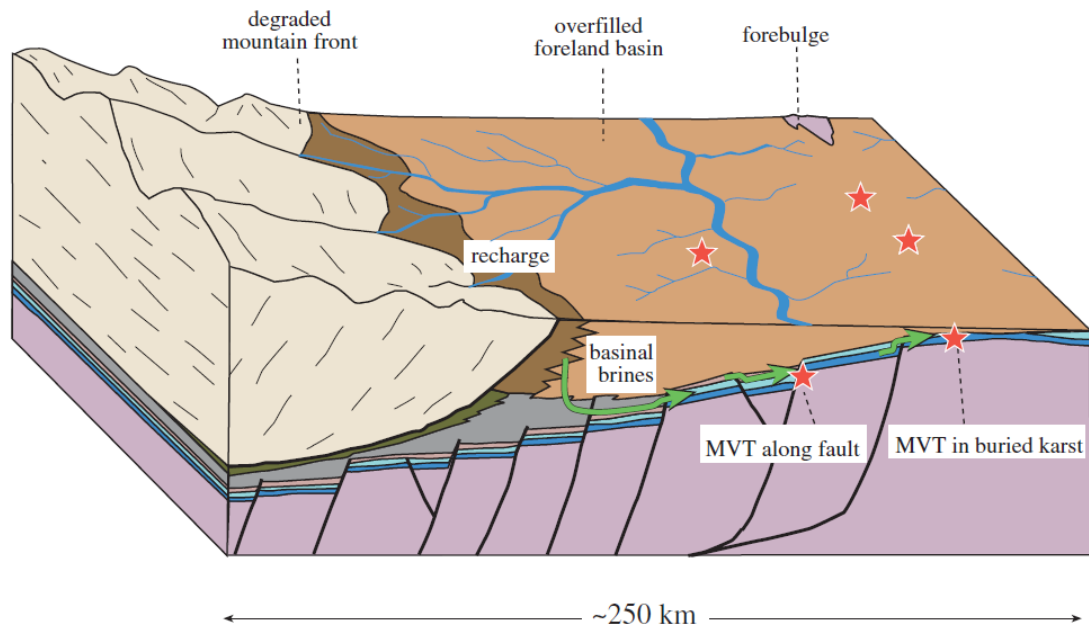


**Figure 2.6. Tectonic settings of the MVT deposits. The foreland basin filled with sediment is creating hydrologic conditions appropriate for generating the MVT mineralization (Leach et al., 2010a).**

The MVT deposits have highly variable and irregular shapes, because of that, it is quite difficult to estimate and classify the dimensions of the ore bodies. In a surface projection view the deposits are rather diverse and refer to geological settings and ore generating processes. The MVT districts may be associated with the collapse breccia bodies, may form extensive interconnected paleo-karst system, and may be controlled by carbonate reef and barrier frameworks or extended fault networks. The vertical extent of economic mineralizations normally does not exceed the range of several tens of meters. The deposits commonly form stratabound or stratiform ore accumulations. The main factors that control the location and geometry of the MVT deposits are the interaction between faults and fracture zones, pre-ore carbonate desalination features and permeable rocks (Leach et al., 2010b).

### **2.1.7. Unconformity Type Uranium Deposits**

One of the most important uranium mineralization types is the unconformity-related Proterozoic deposits. These types of uranium camps are mainly distributed in Australia and Canada. This is a hydrothermal type deposit which forms at redox

fronts where oxidized atmospheric water or underground fluids meet reducing environments or methane enriched fluids. In such settings, the uranium is washed out from rocks and precipitates in ore occurrences (Lehmann, 2008).

In Australia, the primary regions of the unconformity uranium deposits are the Alligator River province and Proterozoic Pine Creek Orogen in Northern Territory. The deposits are related to extended structures adjacent to discordant interfaces between a thick oxidized overlaid sediments and relatively reduced basement rocks. The ore zones form veins or open space-filling breccias and continue into the cover sequence (McQueen, 2005). The uranium deposits are commonly structurally controlled and reflect the geometry of faults and shear zones that normally align to the foliation and layering in host rocks (Pirajno and Bagas, 2008).

## ***2.2. Where to Expect New Discoveries***

The sustainability of the mineral industry is highly dependent on discoveries of new deposits. Exploring new locations is a key to the stable growth of the mining sector. Development of new exploration technologies and a combination of geological, geophysical and geochemical exploration methods allows one to discover new economic mineral targets.

In the last few decades, many analytical reports reveal that the trend of the new mineral discoveries is shifting toward greater depths. Although shallow deposits are still being discovered, the near surface reserves of zinc, copper, gold and other minerals are being depleted (Debicki, 1996). In recent years, the Australian mining industry has demonstrated a clear tendency for finding major ore deposits under thick cover (Schodde and Guj, 2012). Figure 2.7 shows thickness of overburden rocks for mineral discoveries excluding coal, bauxite, and iron ore.

Generally, the giant and major mineral camps are found in the early exploration stage of new geological terrains, because of their sizes and more distinct signatures. However, extensive exploration of detected greenfield areas and continuous research of brownfields can lead to significant discoveries. Figure 2.7 illustrates that the deep ore occurrences (more than 500 m of cover) are usually revealed in the brownfield

districts. In these cases, the existing infrastructure will allow speeding up the development and production stages of the new mine sites. For brownfield territories the time taken from the discovery moment to start up the production on a mine site, normally by 25 % less than for greenfield camps (Schodde and Guj, 2012).

The important aspects of sustainable supply of mineral resources are: researching generation and formation processes of ore deposits, carrying out geological mapping, geochemical and geophysical surveys, and providing the mapping of subsurface structures (Kesler, 2007). One of the primary paths of a future development for the mining industry is finding new major prospects and searching for deeper discoveries.

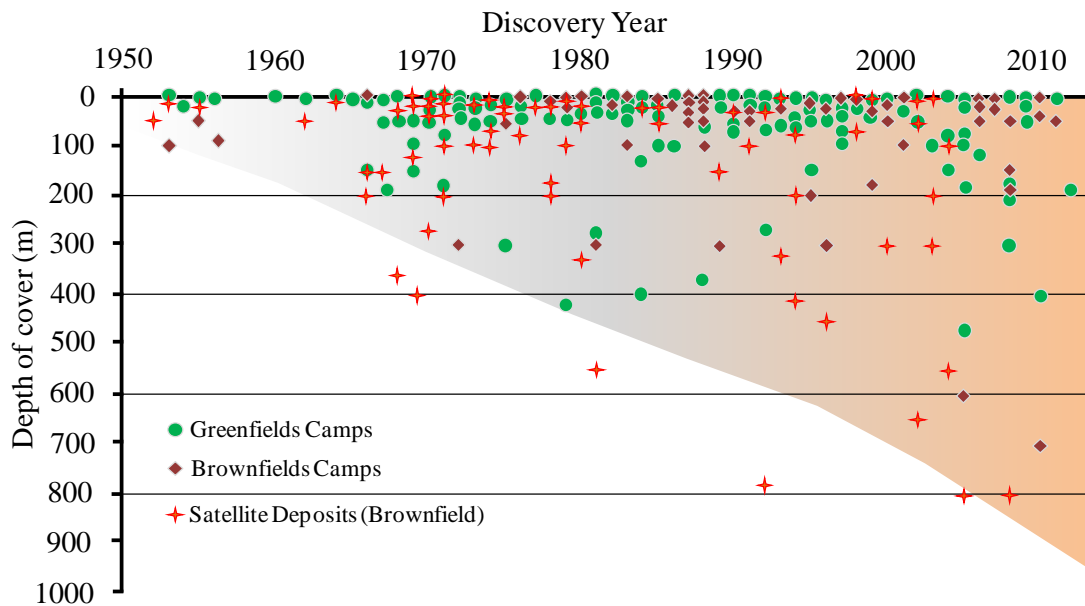


**Figure 2.7. Depth of cover on mineral discoveries in Australia (1950 – 2012)**  
*Analysis excludes Bulk minerals, and is limited to Moderate, Major and Giant deposits only (Major defined as > 1 million ounce Au, >100 kt, Ni, >1 Mt Cu. Giant is >5 Mt Cu-equivalent and Supergiant >25 Mt Cu-equivalent). Satellite deposits supply ore to a central mill within an existing mining camp. (Schodde, 2012)*

### **2.3. Seismic Exploration and Mineral Environments**

The general overview of major types of mineral deposits in Australia shows how variable and complex geological settings are in hard rock environments. The understanding of subsurface structures and interrelationships of rock sequences, faults and mineralization zones is an important key to discover new prospects. Seismic techniques are capable of reconstructing the geological structural model of mineral deposits and are able to address a number of exploration tasks. The complexity of hard rock geology introduces a number of difficulties for seismic methods. This section provides an overview of the main issues that seismic technologies are facing in mining exploration.

Study of the regolith was always an important concern in the mining industry and this task is becoming even more valuable due to the trend of deep mineral

discoveries. Exploration process and followed mining design require knowledge about the overburden structure and its physical properties. Different seismic techniques can be used effectively to characterize the cover formation and inhomogeneities. Propagation velocities of seismic waves in the regolith strata are generally significantly lower than the velocities in the base hard rocks. Such a high velocity contrast between formations affects the quality of seismic reflection images. Presence of heterogeneities in the near surface section causes attenuation of propagating seismic energy and distortion of the seismic signal. This study includes a field experiment that involves two seismic techniques (surface waves and refraction waves) to reveal a near surface structure and properties of the regolith overburden at the Hillside mine site (South Australia).

Many mining prospect areas have rather uneven and rough terrains that bring certain challenges into seismic survey design. In on-shore cases with highly variable topography, the different grounding conditions for locations of shots and geophones significantly influence the quality of seismic records. The present interest in unconventional seabed mineral deposits has involved marine seismic techniques in the exploration process. In this instance, the precise reconstruction of the dissected topography of the ocean floor is required information for the excavation design and it is a challenging task for seismic processing and imaging. This research involves an example of application of the diffraction imaging method to seismic data acquired in the Bismarck Sea for exploration of off-shore ocean floor massive sulphide deposits.

Most of the mineral deposits are structurally controlled; mineralization occurrences are often confined to structural elements such as faults, shear zones, lithological unconformities, etc.; a number of deposits form the stratiform bodies, others compile in a specific stratigraphic interval as a stratabound formation. Thus, knowledge of structure interrelationship and stratigraphic units is essential for mineral exploration. Seismic methods are able to produce high resolution images of the geological structure. Seismic imaging techniques require the input information regarding propagation velocities of the media. This information is usually recovered from seismic data in the processing step called interactive velocity analysis or such information can be obtained from borehole acoustic logs. Complexity of hard rock

environments and lack of continuous interfaces make the recovering of the velocity model a non-trivial task. Hard rocks have high seismic velocities; this fact brings in additional difficulties in the velocity analysis; also the resolution decreases if for hard rock seismic exploration the same source parameters (dominant frequency) have been used as for the investigation of sedimentary basins. The borehole acoustic measurements are often not available during mineral exploration. In this study a seismic imaging algorithm which does not require the input velocity model is introduced to mineral exploration and has been tested on synthetic and field seismic datasets.

One of the common issues in the hard rock seismic exploration is a quality of seismic data. Strong inhomogeneity of the environment often causes the low signal to noise ratio in seismic data. In many cases seismic surveys have been acquired at the production mining sites where the high level of ambient noise is produced by drilling rigs, moving machinery, etc. This research includes the development of a seismic imaging algorithm which is capable of handling data with a low signal to noise ratio. This 3D post-stack migration utilises diffraction attributes to enhance images quality. The method has been tested on a synthetic dataset and several field 3D seismic volumes.

### **3. Hard Rock Seismic Exploration**

Seismic exploration provides higher resolution images than other geophysical methods. Nowadays, reflection seismic technologies play an important role in oil and gas exploration and identifying hydrocarbon deposits. As shown by over 50 years of hydrocarbon exploration, seismic data allow geophysicists to construct detailed models of deposits, and even to monitor the process of their production. Nevertheless, in the mining industry the seismic methods are not so widespread. The main reason is a high structural complexity of hard rock environments that includes shear zones, reverse and relaxation faults, altered and fractured zones, intrusions and folding. Despite this, hard rock seismic has a long history and many successful examples of applications, and nowadays trends to be a standard exploration tool for mineral prospecting.

#### ***3.1. Overview of hard rock seismic exploration***

One of the first reported active experiments involving seismic waves detection in granites was conducted in 1878 in France near the township of Commentry in a house basement by Ferdinand Fouqué (Fouqué, 1888). In spite of such an early history of hard rock seismic measurements, there are not as many publications about the application of reflection seismic techniques in hard rock environments as there are seismic exploration in sedimentary basins. One of the earliest seismic surveys in a hard rock environment in the twentieth century was carried out in 1927 in the USSR to investigate mineral deposits near Krivoi Rog; in the same period prospecting for iron ore using seismic was conducted in England (Karaev and Rabinovich, 2000). In the 1940s the refraction seismic technology was used in Russia to study the crystalline basement (Gamburtsev et al., 1952). The high-frequency seismic method was introduced in Russia in the 1950s to investigate ore deposits and map vertical-layered media (Berson, 1957). A number of studies have been performed to characterize the correlation between seismic velocities and physical parameters of igneous and metamorphic rocks (Birch, 1960; Dortman and Magid, 1969; Krylov et al., 1990).

Large numbers of independent case studies have been conducted over the last few decades to develop useful and cost effective seismic technology for deep mineral exploration and mine planning. Many significant and successful projects were discovered in the 1980s; the outcomes have shown the potential of seismic techniques as a reliable targeting and mapping tool in hard rock environments. Green and Mair (1983) published the results high-resolution reflection seismic survey to study the fracture system at the radioactive waste disposal area on the Canadian Shield. Pretorius et al. (1989) presented the benefits from the cooperative approach using seismic and petrophysical techniques to identify geological structures for mining exploration in Witwatersrand Basin, South Africa.

Knowledge of acoustic properties and scattering characteristics of ore bodies is essential to construct adequate images in hard rock environments. Rock physics research is an integral part of seismic studies; it allows understanding and estimating the distribution of physical properties of ores and host rocks. According to a number of researchers, the average velocities of acoustic waves in igneous and metamorphic rocks typically increase with density along the known Nafe and Drake (Figure 3.1) curve for Earth rocks (Nafe and Drake, 1963). Nelson (1984) acquired a seismic survey in South Australia and concluded that the difference in hard rock density and velocity provides distinctive seismic reflections; and that reasonable acoustic impedance contrasts are most likely to be caused by density variation in rocks. Another important result demonstrates that sulphide ores and concentration of certain Fe-oxides because of their high density have higher acoustic impedance with respect to surrounding rocks (Salisbury et al., 1996). Massive ore mineralizations with relevant size and geometry should produce a strong seismic response in many geological situations (Salisbury et al., 2000). The contrast of acoustic impedance between felsic and mafic rocks is also significant; this allows an opportunity to detect mafic intrusions: dikes or sills (Salisbury et al., 2000). The high acoustic impedance of massive mineral deposits, which has been disclosed by laboratory measurements, should be confirmed by in-situ measurements from borehole logging as well. During the last decade such high values of acoustic impedance were verified at many mine sites (Eaton et al., 2003).

In the last few decades the number of publications reporting the successful results of seismic exploration surveys at hard rock mine sites has constantly increased. Many papers are coming out of Australia, South Africa, Canada and Northern Europe. Stevenson and Durrheim (1997) reported several case studies about gold, platinum and base metal exploration and mining in Southern Africa utilizing the reflection seismic. They have shown the results of the structural imaging, mapping of different reef types, detecting base metal ore bodies and defining faults. Drummond et al. (2000) presented a paper about several two dimensional (2D) regional seismic lines acquired over ore bearing structures at the Yilgarn craton, at the Mt Isa tectonic province and Tasmania. The study reveals the structures of deep faults and shear zones, which have been used for the modelling of mesothermal fluid flows and detection of distribution of mineralization zones. Roy and Clowes (2000) published the outcomes of a regional-scale seismic experiment over porphyry copper deposits in British Columbia to define the edges of a batholith. Several surveys conducted in granitic environments in Sweden were described by Juhlin and Palm (2003); the results have shown the successful determination of the sub-horizontal fracture zones and dipping dolerite / granite interfaces from reflection seismic images.

The first application of three-dimensional (3D) reflection seismic for mining planning and development was conducted in 1994 at Vaal Reefs in South Africa (Pretorius et al., 1997). The appropriate structural model of the Ventersdorp Contact 'Reef' gold ore body with adequate resolution was obtained from seismic data and has been used for mining design; the cost-effectiveness of 3D seismic survey was also demonstrated. The following 3D seismic survey in the Witwatersrand basin (South Africa) (Stuart et al., 2000) has provided the structural and depth models of the prospective stratiform ore horizon and revealed important information regarding faulting and lithological variations. This comprehensive result has led to the design of a shaft site and avoided the fault-damage zones and potentially hazardous grounds. Larroque et al. (2002) showed the direct delineation of sub-metric layered platinum mineral deposits at a depth of 800 m using 3D seismic. The 3D seismic survey was carried out in 1995 in the Sudbury basin in Canada; the investigation has provided important images of geological structures and lithological contacts as well as delineated the deep nickel-copper mineralization zone (Milkereit et al., 2000).

Malehmir and Bellefleur (2009) imaged the blind massive sulphide body from reprocessing seismic data acquired over the Halfmile Lake deposit located in the Bathurst mining camp in Canada (Adam et al., 2000). In the last decade several 3D hard rock seismic datasets were collected in Australia to investigate gold, nickel and uranium mineral sites (Williams et al., 2010).

In recent years seismic exploration has achieved good results in hard rock environments and a number of successful 2D and 3D surveys were completed on mine sites all over the world (Malehmir et al., 2012; Urosevic et al., 2012; White et al., 2012). Despite this, reflection seismic still does not play a major role in mineral exploration. Hard rock is a challenging environment for seismic. It has high seismic velocities and rather complex structure; seismic data often have a low signal-to-noise ratio. Further developments and improvements have to be provided to be able to use thoroughly all seismic benefits for mineral exploration.

### ***3.2. Hard Rock Characteristics***

Hard rock terranes are characterized by great ranges in lithology, metamorphism, and deformations. The compressional velocities of hard rock are generally higher than in sediments, where velocity usually does not exceed 4000 m/s. The average velocities of common hard rock formations tend to increase with density along the Nafe-Drake curve (Figure 3.1). Such a trend was first discovered in marine sediments (Nafe and Drake, 1963); Gardner et al. (1974) introduced an empirical relationship between compressional velocity and density for sedimentary rocks; this trend has been expanded to igneous and metamorphic rocks. In general, velocities and densities of hard rocks increase with growth in metamorphic grade and reducing silica content in rocks. So, interfaces between felsic and mafic formations should make detectable reflections and ultramafic rocks can give reflections against any lithological sequences. Measurements of sulfide ores were completed by Salisbury et al. (1996). Figure 3.1 shows that massive sulfides are located far to the right of the Nafe-Drake curve, their high density and wide range of velocities can be explained by differences in atomic weight and crystal structure (Birch, 1961). Thus sulfide ores have high impedance and should produce strong reflections within almost any host silicate

rocks. Mineralized units have unique velocity-density characteristics, and if they meet the geometric constraints (Chapter 3.3), mineral deposits can be illuminated on seismic images.

Information regarding compressional wave velocities and shear wave velocities and measurements of the rock density enables one to obtain the elastic parameters (dynamic moduli) of the formation: Young's modulus, Poisson's ratio, Bulk modulus, Compressibility and Shear modulus. Elastic attributes are important to engineers for mine design and for geophysicists for rock composition characterization.

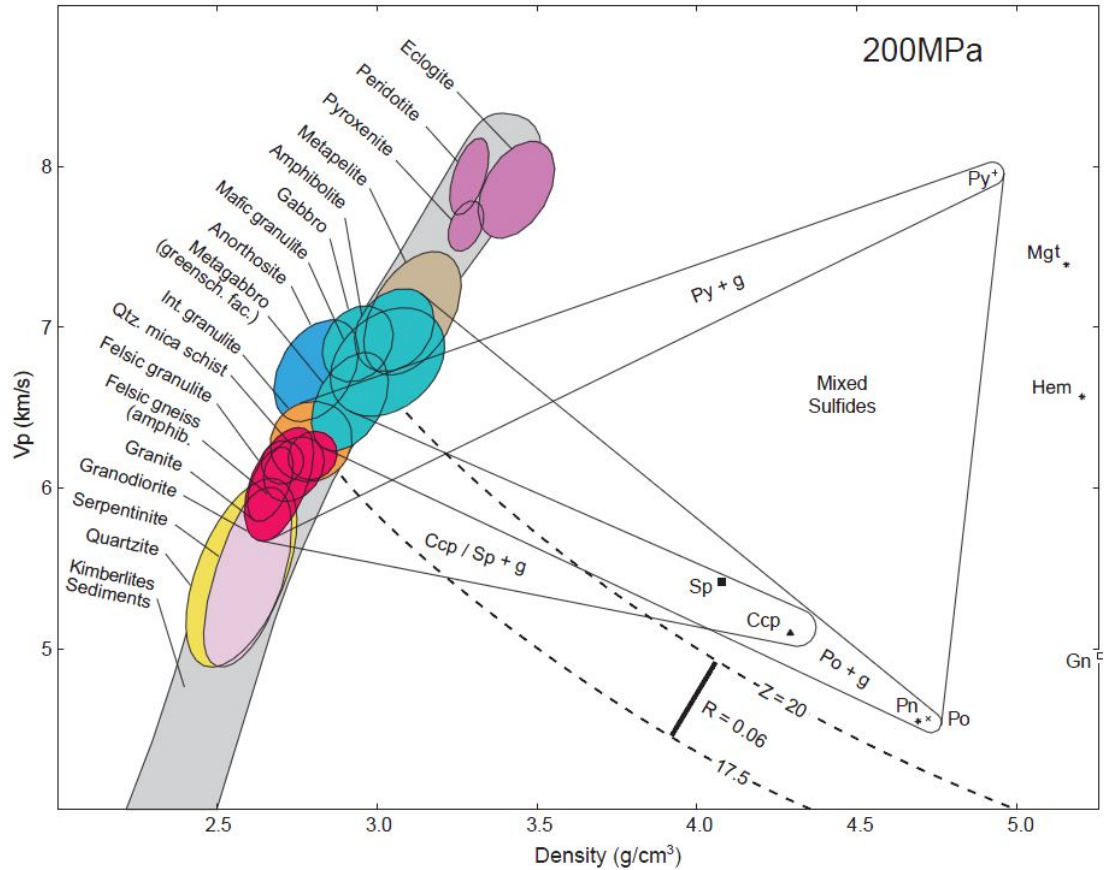


**Figure 3.1.** P-wave velocity versus density at confining pressure of 200 MPa for common hard rocks. Light grey is the Nafe-Drake curve. Lines for constant acoustic impedance for felsic ( $Z = 17.5 \cdot 10^5 \text{ g/cm}^2\text{s}$ ) and mafic rocks ( $Z = 20 \cdot 10^5 \text{ g/cm}^2\text{s}$ ) and the minimum reflection coefficient ( $R$ ) required to produce strong reflection are shown for reference. Abbreviations: Py – pyrite, Sp – sphalerite, Ccp – chalcopyrite, Po – pyrrhotite, Pn – pentlandite, Gn – galena, g – gangue, Mgt – magnetite, Hem – hematite (Salisbury et al., 2003).

### 3.3. Basics of Seismic Theory

This chapter describes the basic principles of propagation of seismic energy through a geological medium and an overview of seismic techniques that have been used in research for hard rock seismic exploration. The range of tasks and issues which should be addressed in mining seismic investigation is quite considerable, and for certain problems particular methods and approaches have to be applied.

### **3.3.1. Principals of Propagation of Seismic Energy**

Seismic methods are based on the study of elastic waves propagated through the Earth strata. Geological rocks and formations are characterized by different elastic properties and have various seismic velocities. Seismic energy propagating from a source encompasses different wave types such as surface waves, compressional waves, transversal waves; when waves encounter a contrast in properties at the boundary between two formations diverse responses could be generated – reflection, refraction and diffraction – and a conversion of wave types may occur. Recording of the seismic signal transmitted through the subsurface and analysis of these data enables one to estimate the velocity distribution in media, properties of the Earth's formations and geological structure.

Waves in elastic media interact with boundaries based on the Huygens-Fresnel principal and Fermat's principal. Huygens proposed that every point to which wave disturbances reach can be considered a source of a subsequent spherical wave (Huygens, 1690). Each following wavefront (surface including all the points in space reached by a wave at a particular time and at which the phase of a travelling wave oscillation is the same) represents an envelope tangent to all consecutive spherical waves and energy is carried along ray paths (directions or lines) everywhere perpendicular to the envelope surface (wavefront). Fresnel modified this statement with the principle of interference in order to explain some effects such as absence of a back wave formation and diffraction effects. Later Kirchhoff demonstrated that the wave propagation principle could be obtained from the wave equation.

Another essential principle of wave propagation has been proposed by Pierre de Fermat and is known as the Least-Time Principle. Its modern form states that the length of the ray path travelled by the wave between two points in a medium is an extremum or remains unchanged, in other words the ray path length must be stationary. An important consequence of this principle is determination of the relationship between the angles of incidence and refraction in the case of a wave passing through an interface between two various isotropic media and is known as Snell's law.

### 3.3.2. Seismic Reflectivity

Seismic reflectivity exists due to a contrast in the properties of different lithological formations, namely the seismic velocities and rock densities. The amount of energy reflected from rock boundaries depends on changes in acoustic impedance between geological sequences. Acoustic impedance  $Z$  is a combination of the density and seismic velocity of the rock unit. The ratio of the amplitude of the reflected wave to the incident wave is called the reflection coefficient. Reflection coefficient  $R$  for a normally incident seismic wave is defined by the expression:

$$R = \frac{\rho_2 V_2 - \rho_1 V_1}{\rho_2 V_2 + \rho_1 V_1} = \frac{Z_2 - Z_1}{Z_2 + Z_1}, \quad (3-1)$$

where  $Z_i = \rho_i V_i$  is acoustic impedance of the layer  $i$ ,  $\rho$  is density of individual layers and  $V$  is velocity of individual layers. The shear wave impedance and reflection coefficient can be calculated by substituting compressional (P-wave) velocity with the shear (S-wave) velocity.

Reflectivity is also influenced by angle of incidence of a seismic wave at an interface. In the case of normal incidence of a wave on an interface only the same type of reflected and transmitted waves are generated. If a compressional wave arrives at an oblique angle to the interface, the energy is partitioned into reflected P- and S-waves, as well as transmitted P- and S-waves; and reflectivity gets more complicated (Yilmaz, 2001). The simple case of two media with a plane boundary is shown in Figure 3.2.

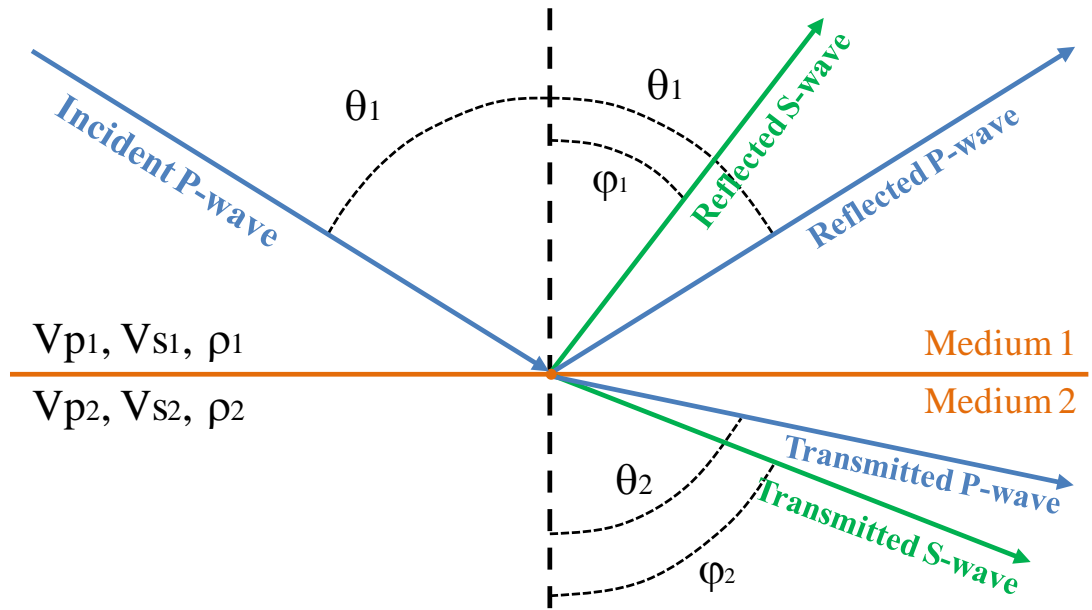


**Figure 3.2.** Incident P-wave at an oblique angle to the plane interface and generated P- and S-waves (Yilmaz, 2001).

Snell's law describes the relationship between the reflection and transmission angles:

$$p = \frac{\sin \theta_1}{V_{P1}} = \frac{\sin \theta_2}{V_{P2}} = \frac{\sin \varphi_1}{V_{S1}} = \frac{\sin \varphi_2}{V_{S2}}, \quad (3-2)$$

where  $p$  is the ray parameter,  $\theta_1$  is the angle of incidence as well as the reflected P-wave,  $\theta_2$  is the angle of transmitted P-wave,  $\varphi_1$  is the angle of reflected S-wave, and  $\varphi_2$  is the angle of transmitted S-wave.  $V_{P1}$  and  $V_{P2}$  are the P-wave velocities in the upper and lower medium respectively;  $V_{S1}$  and  $V_{S2}$  are the S-wave velocities in the upper and lower half spaces respectively.

The proportions of the reflected and transmitted energy depend on the angle of incidence and properties of a medium. Using continuity of displacement and stress at the reflecting interface as boundary conditions, the reflection and transmission coefficients have been defined as a function of incident angle and the elastic properties of the materials (densities, bulk, and shear moduli) by Knott (1899) and Zoeppritz (1919). The complex solutions of Knott and Zoeppritz equations were approximated by a number of authors (Aki and Richards, 1980; Shuey, 1985). These

simplifications are widely used to estimate physical properties of geological media such as lithology, porosity, and fluid content.

### **3.3.3. Vertical and Horizontal Resolution of Seismic Data**

The spatial and vertical resolution of seismic data are significant parameters for hard rock environments. It is especially important to have consistent depth resolution to discover deep mineral deposits. For complex geological conditions it is essential to have a decent horizontal resolution as well, to be able to distinguish and delineate structures.

Seismic vertical resolution – the ability to identify separate layers or objects – is determined by a dominant measured wavelength. In order to distinguish two interfaces their thickness should be about one quarter of the wavelength ( $\lambda$ ) of the seismic data (Rayleigh Criterion).

$$\lambda = \frac{V}{f}, \quad (3-3)$$

where  $f$  is the dominant frequency and  $V$  is the average velocity of a medium (Sheriff and Geldart, 1982). The limitations of the vertical resolution depend not only on the wavelength of the seismic waves but also on the thickness of the beds. Figure 3.3 shows the limits of vertical resolution; the layers with thickness less than the first zero crossing interval of the wavelet could not be resolved on seismic data. With typical velocities of 5000 – 6000 m/s for hard rock environments and 50 Hz dominant frequency of acquired seismic data, the resolution is approximately 25 – 30 meters for two dimensional (2D) seismic surveys. Such general temporal resolution enables hard rock seismic to detect deep structures (> 500 m) and mineral features including mineralization zones, shear zones, fault zones and large alteration zones.

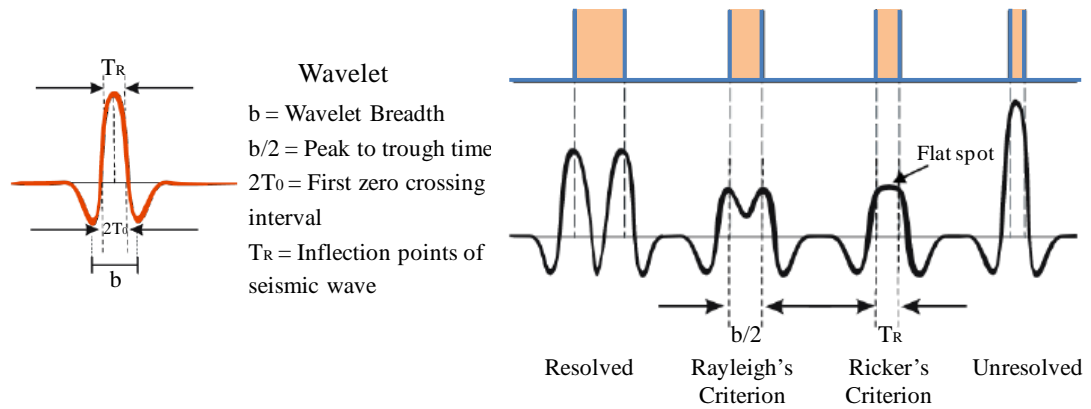


**Figure 3.3. The Rayleigh's and Ricker's limits of vertical resolution (Kallweit and Wood, 1982).**

The spatial resolution is an ability to detect two horizontally separated bodies on seismic data as individual objects rather than one. Lateral resolution is a function of the received signal wavelength; it as well depends on the frequency, the velocity of media and the depth of the reflecting boundary. According to Huygens' Principle, seismic sources produce a spherical wavefront, which reflects from not just one point but from an area. This region is known as the Fresnel Zone. The definition of the lateral resolution in terms of Fresnel zone is shown in Figure 3.4. S is a source-receiver location, O is geometrical reflection point, and AB is the first Fresnel zone. All reflection points within disk AB are indistinguishable at the receiver position. The radius  $r$  of that zone is approximated by the equation:

$$r = \sqrt{\frac{Z_0 \lambda}{2}}, \quad (3-4)$$

where  $Z_0$  is the depth,  $\lambda$  is the reflection wavelength (Yilmaz, 2001). In terms of dominant frequency  $f$  the radius of the Fresnel zone is:

$$r = \frac{V}{2} \sqrt{\frac{t_0}{f}}, \quad (3-5)$$

where  $t_0$  is the two-way travel time of the seismic reflecting energy,  $V$  is velocity.

Limiting of horizontal resolution by the Fresnel zone applies to unmigrated seismic data. Migration is the process of repositioning of data events to their true locations,

in other words, this is the procedure of moving the return signals to illuminate an interface point being encountered by a seismic wave rather than where it has been recorded. The migration increases spatial resolution, and theoretical limit of horizontal seismic resolution on migrated data is about

$$r \sim \frac{\lambda}{4}, \quad (3-6)$$

where  $\lambda$  is the reflection wavelength (Brown, 1999).

It should be noted that confidence of resolving under surface structures and objects also depends to some extent on the signal to noise ratio.

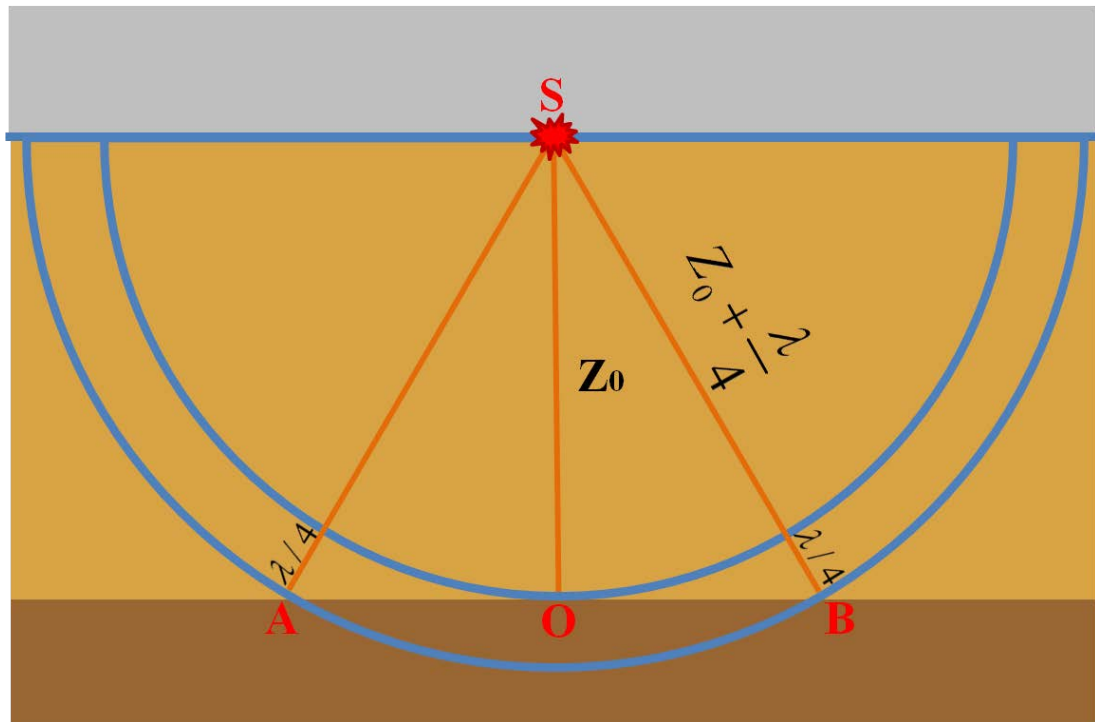


*Figure 3.4. The First Fresnel Zone (Yilmaz, 2001).*

### 3.3.4. Surface Waves and Multichannel Analysis of Surface Waves (MASW)

Surface waves are generated in cases where the medium is bounded by a free surface and propagation takes place near the surface. In 1885 Lord Rayleigh mathematically discovered the existence of waves which propagate along the surface and have exponentially decreasing amplitudes with distance from the surface (Rayleigh, 1885).

Considering a case of a layer on a half-space, Love proved the presence of surface waves which are polarized horizontally in the plane perpendicular to the direction of propagation (Love, 1911). Surface waves are named after their discoverers as Love waves and Rayleigh waves. Love waves are basically shear waves that propagate along the surface; the particle motion in these waves is transverse and parallel to the surface. The particle motion of those waves consists of variable transverse motions. Particle movements are horizontal and perpendicular to the direction of the wave propagation. Love waves require a shear velocity structure that increases with depth, and do not exist in a homogeneous half-space (Novotny, 1999). Rayleigh waves travel along the surface and the particles move as ellipses in two planes: normal to the surface (vertical) and parallel to the direction of the wave propagation. At the surface and at shallow depths this motion is retrograde. Particles deeper in the medium move in smaller ellipses with an eccentricity that changes with depth. At greater depths the particle motion becomes prograde (Figure 3.5). Surface waves have cylindrical wave fronts, their amplitudes decrease with the square root of the distance from the source point (Strobbia, 2003).

The depth of significant displacement in the material is approximately equal to the wavelength. The waves with longer wavelengths (low frequency) penetrate deeper into the medium than short wavelength waves (high frequency). The propagation of surface waves in a vertically heterogeneous medium shows a dispersive relation. In a homogeneous medium Rayleigh waves do not show dispersive characteristics and all the wavelengths have the same velocity. The geometric dispersion of surface waves in heterogeneous media means that different frequencies have different phase velocities and depend on the geometry of the investigated subsurface media. This phenomenon is being used to obtain the vertical distribution of the shear wave velocity, characterise the Earth's interior, explore near surface structures and rock properties.

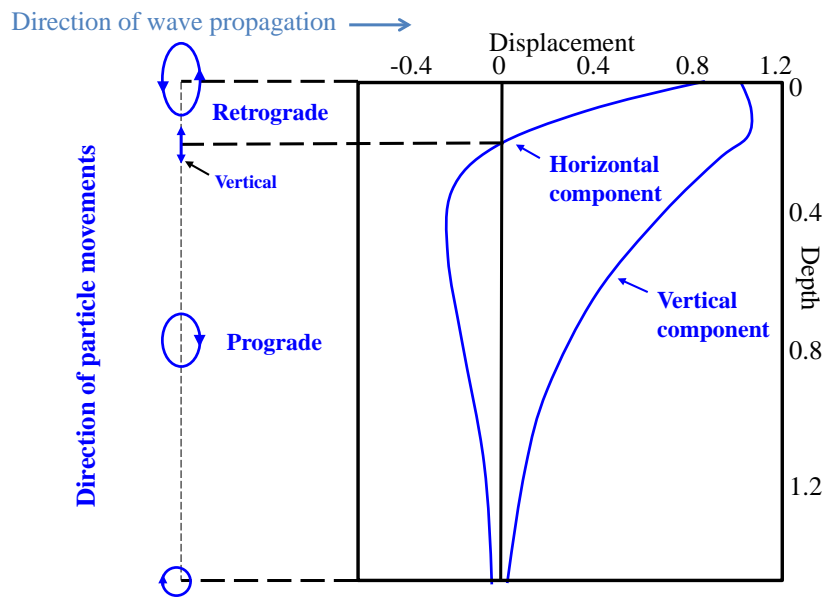


**Figure 3.5. Rayleigh wave displacements with dimensionless depth (Cuellar, 1997).**

Surface waves are widely used to study the Earth interiors as well as for site characterizations. Since the mid of twentieth century many papers have been published about the application of surface waves to reveal the crustal and upper mantle structure (Brune and Dorman, 1963; Dorman et al., 1960; Kovach, 1965); a number of researches of the uppermost crustal structure have been done using short-period surface waves (Arström and Lund, 1993; Holub and Novotny, 1997). The near surface applications of surface waves for soil properties investigation and geotechnical engineering date back to the 1950-1960s (Jones, 1958; Richart et al., 1970). Further developments have led to introduction of the spectral analysis of surface waves (SASW) (Heisey et al., 1982); the method is based on the recording of the surfaces waves of various wavelengths utilizing a pair of receivers with certain offsets for a particular wavelength (Nazarian et al., 1983).

At the moment the preferred approach for the reliable estimation of near-surface properties by surface waves is the multichannel analysis of surface waves (MASW) (Park et al., 1999). The method is designed to obtain the near surface structure and evaluate rock properties (like shear modulus) from shear-wave velocities. Data are recorded by using multichannel linear setup or another suitable configuration of the receiver array for a particular task. The approach deals with seismic waves in the

low-frequency range (3-30 Hz) and the investigation depth does not exceed a few tens of meters. The method has two modifications: active and passive. In active acquisition the surface waves are generated through an impact source (like a weight drop), the passive mode utilizes the seismic energy generated by natural (e.g. thunder, tides) or cultural (e.g. cars) causes (Park et al., 2007). Relatively simple in-field acquisition setup and following data analysis make the MASW a cost effective seismic tool for uncovering shear-wave velocity information and geotechnical parameters of near surface materials.

In mineral environments seismic methods based on surface waves analysis can in an inexpensive manner reveal valuable information about regolith structure and provide near-surface rock properties for engineering mine design. Research involves a near surface seismic experiment at the Hillside mine site in South Australia, which includes the MASW approach to investigate the structure and properties of cover rocks.

### **3.3.5. Refraction Seismic**

Refraction seismic deals with a boundary phenomenon that occurs when a wave passes from one material to another at an oblique angle. The propagation of refracted waves is described by Snell's law (equation 3-2). The principals of propagation of refracted waves have been used in seismology to determine the Earth's interior structure. In 1909 Mohorovicic defined the thickness of the Earth crust, in 1913 the radius of the Earth core was determined by Gutenberg, in 1936 Lehmann discovered the inner core and in 1939 Gutenberg and Jeffreys independently obtained the first velocity model of the Earth (Aki and Richards, 1980). The first application of seismic methods for petroleum exploration was the refraction survey conducted by Mintrop in 1923 in Mexico (Weatherby, 1940).

Nowadays, the seismic refraction method is one of the common geophysical techniques for near surface exploration and mainly used in engineering, mining, groundwater and environmental site investigations. The refraction method is utilized to provide detailed information on the thicknesses and structure of subsurface layers with characterization of seismic velocities. Based on the density contrast that usually

exists between geological formations, the refraction approach is generally applicable where the seismic velocities of rock sequences increase with depth. In refraction seismic surveying, the earliest times of arrival (first breaks) of the seismic waves at various distances from the source are measured. When energy, emerged from the shot point, reaches the lower boundary of the high velocity layer at a certain angle (critical angle) the head wave starts propagation along that layer and transmits back to the surface. This critical angle ( $i_c$ ) could be derived from Snell's law (equation 3-2). Eventually, that wave overtakes the direct wave (after the crossover point) and becomes detectable as first breaks in a seismogram. The basic principle of the refraction seismic is shown for a two-layer model in Figure 3.6.

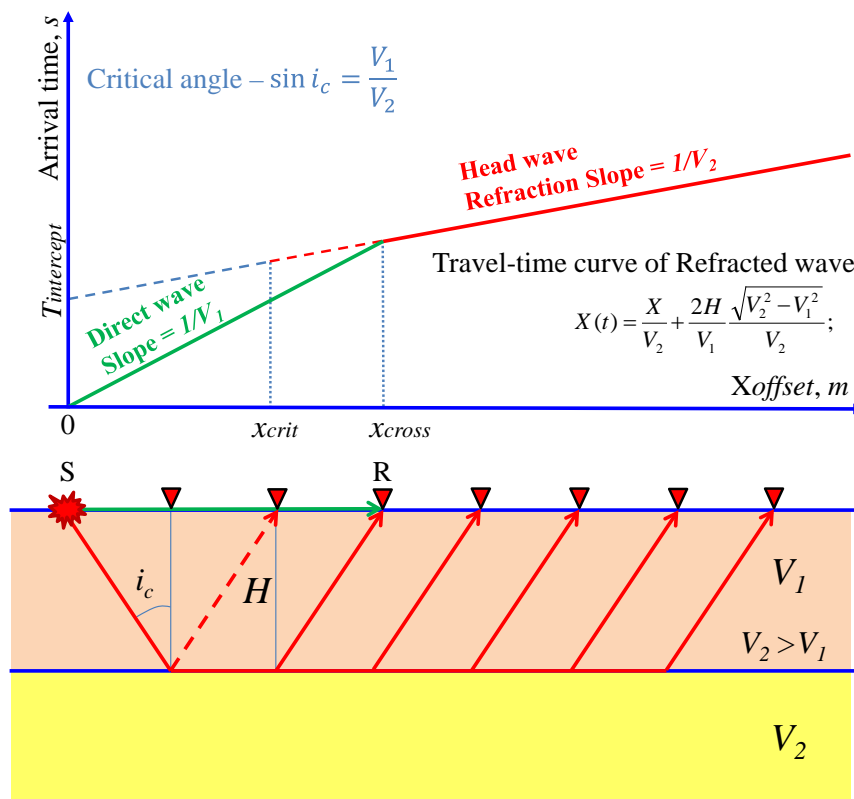


**Figure 3.6. Principle of seismic refraction method. Travel-time curves of direct wave (green) and refracted arrivals (red) are shown. Critically refracted waves start arriving after critical distance  $x_{crit}$ , and overtake the direct waves at a crossover point  $x_{cross}$ .**

Field acquisitions of the refraction seismic are generally conducted along 2D linear profiles; geophones are spread in a line, weight-drops or sledge hammers are

normally used for the generation of waves; seismic signals are transmitted to the recording system. Refracted waves travel quite a long distance before they are able to reach the survey spread, and low frequency geophones are desirable for the refraction seismic acquisition; commonly 8 to 14 Hz geophones are used for these surveys. The length of the geophone array should be 3-5 times the depth of investigation and the required horizontal resolution should be balanced by the number of channels in the spread (Dobrin and Savit, 1988).

There are a number of interpretation methods in refraction seismic exploration to obtain the information about subsurface structure and velocity distribution. The one-dimensional inversion has been formulated in seismology in the early part of the twentieth century by Herglotz (1907) and Weichert (1910) for reconnaissance of Earth's structure; the method considers a laterally homogeneous medium with velocity monotonically increasing with depth. Dobrin and Savit (1988) provided a broad overview of the most published methods of the interpretation of refracted waves. Hagedoorn (1959) developed a practical approach for interpretation of refraction sections: the plus-minus (reciprocal) method; the method is based on the traveltimes reciprocity and commonly used in near surface investigations; the approach is often utilized even for real-time processing of refraction data (Van Overmeeren, 2001). The further improvement of the reciprocal technique – the generalized reciprocal method – has been introduced by Palmer (1980). This method is able to determine layers with varying thicknesses and velocities and handle the dips up to about 20 degrees. The refraction tomography methods are the alternative approaches to determine the velocity distribution of the subsurface media in case of a complex geological situation (Iyer and Hirahara, 1993; Stefani, 1995).

In mineral exploration the refraction seismic is widely used for mapping the overburden structure (Whiteley, 1994). The study includes the investigation of the regolith structure at the Hillside mine site in South Australia by analysing the propagation of refracted waves in cooperation with the MASW technique.

### 3.3.6. Reflection Seismic

The reflection seismic is the most common geophysical methodology used to acquire images of the Earth's structure at depth which provides information on its geology and its subsurface resources. The first reflection seismic survey was carried out to map the interface between shale and limestone formations in 1921 by Geological Engineering Company in Oklahoma, USA (Weatherby, 1940). At present time, the seismic reflection technique is capable of providing high-resolution, detailed 2D and 3D models of stratigraphic boundaries and geological structures with defining the rock properties and it is used as well for time-lapse monitoring of reservoirs.

During seismic surveys, a source of seismic waves radiates energy into the ground. Energy forms spherically spreading wavefronts away from the source. According to Fermat's principle the energy, originated at the source, will traverse along a particular ray path (perpendicular to the wavefront) to the subsurface layer and reflect back to the geophone at the surface in the least time. In the case of a horizontal interface, the path of least time will generate a reflecting point midway between the source and the receiver with the angle of incidence equal to the angle of reflection from the boundary (Figure 3.7). The travel-time curve of the reflected wave to the first flat interface is given by the hyperbolic equation:

$$T_{refl}^2 = \frac{X^2}{V_1^2} + \left(\frac{2H}{V_1}\right)^2, \quad (3-6)$$

where  $T_{refl}$  is the arrival time of the reflected wave,  $X$  is a source-receiver offset,  $H$  is depth of the interface,  $V_1$  is the propagation velocity of the first layer.

The amount of energy reflected back to the surface from the strata boundaries is determined by the acoustic impedance, which is the product of the formation density with the wave velocity (see Chapter 3.3.2). The higher amplitudes of the reflected wave correspond to the larger contrast of the acoustic impedance between two layers. When the velocities and densities are different between two lithological units, but the impedance is (nearly) the same, there will be no reflection in the record. In reflection seismic, the amplitude measurements are really important and analysis of that

information provides an opportunity to recover valuable knowledge about physical properties of rock sequences.

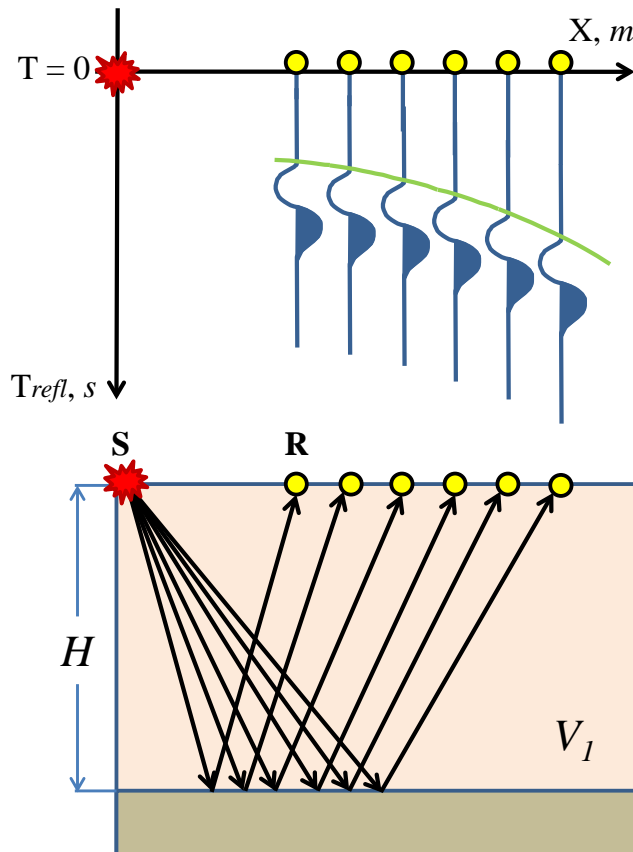


**Figure 3.7. Basic principle of reflection seismic. Travel-time curve of the reflected wave from a horizontal interface is shown (green).**

The reflection seismic is the most commonly encountered geophysical tool for subsurface imaging and it has about a 100-year history of theoretical research and practical applications (Dragoset, 2005; Weatherby, 1940). The basic principles of waves propagation and media properties which cause reflection from a boundary are mentioned above, and all aspects of the theory of seismic waves, acquiring and processing of seismic data and recent discoveries could be found in numerous scientific publications (Sherrif and Geldart, 1995; Yilmaz, 2001).

The ultimate purpose of processing seismic reflection data is to obtain a reliable image of subsurface structure to be able to construct a geological model of a reservoir or a mineral deposit. In order to achieve that goal the reflections should be

enhanced and all other waveforms and noise have to be attenuated or suppressed. A number of signal processing manipulations have to be accomplished to produce a dataset of satisfactory quality. The seismic processing routines generally include: editing to remove the noisy traces; static corrections to compensate for topographic elevations and velocity variations in the shallow part of the section; filtering to reduce the presence of any types of noise; deconvolution to retrieve the reflectivity function from the seismic trace; geometrical corrections to account for the different reflection ray lengths at various receiver locations; stacking to improve signal to noise ratio and emphasize the reflections. Details regarding seismic processing steps are available in many publications (Hatton et al., 1986; Sherrif and Geldart, 1995; Yilmaz, 2001).

Migration is a final and essential step of reflection seismic data processing to obtain an accurate image of subsurface geological structures of the Earth. Seismic migration is a process of the geometrical repositioning of the recorded events to their true locations, where seismic waves actually reflect from subsurface interfaces and objects.

Figure 3.8 illustrates the basic geometric principle of migration on an example of a dipping reflector. Considering the constant velocity situation and assuming a coincident shot-receiver section, Figure 3.8 shows the migration equation, which describes the relationship between an apparent and original dip of the interface. The apparent dip angle is always smaller than the real one, the length of the reflector on the seismic unmigrated section is longer than on the migrated geological section and after migration the reflector moves in the up-dip direction (Yilmaz, 2001).

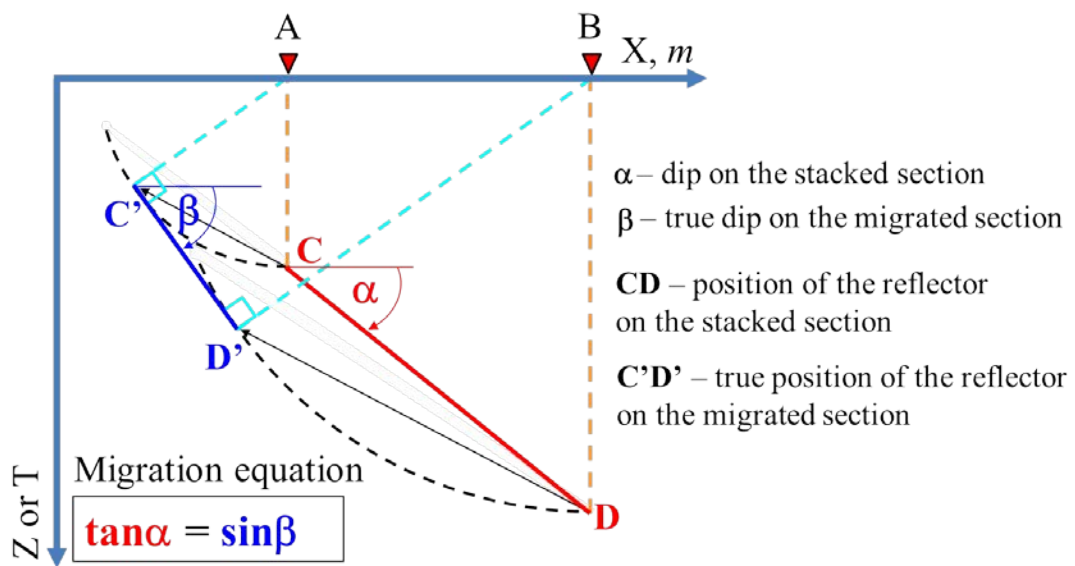


**Figure 3.8. Migration principle. Geometrical consideration of migration of a dipping reflector (Bancroft, 2007).**

There is a variety of migration algorithms and approaches. The classification of the migration algorithms are based on the assumptions underlying the methods, the domain of practical realization and the imaging approach utilized to construct the final migrated image. Migration processes can be performed for post-stack and pre-stack data as well as in time and in depth domains.

The post-stack algorithms are based on the assumption that the input stacked section represents a zero-offset acoustic wavefield, while the pre-stack techniques are dealing with input data with non-coincident source and receiver locations. The post-stack methods are computationally cheaper and faster than the pre-stack approaches, however with modern computer performance the preference is often given to the pre-stack algorithms especially in complex geological situations. The time migration is conducted in time coordinates and produces time image sections and can handle only slight lateral variations in the velocity field. The depth migration produces the most accurate and suitable for interpretation seismic sections in depth and can be applied in situations with presence of arbitrary velocity variations. However, this approach requires the velocity model in depth to be as close to the *a priori* geological model as possible. Every algorithm has an area of application; the most appropriate approach

should be chosen carefully to obtain an accurate enough final image for reasonable time and cost expenses.

The research includes the study of the prestack time migration algorithm with simultaneous velocity estimation and its application in hard rock environments. The capabilities of this approach for hard rock seismic exploration have been demonstrated on synthetic models and on the 2D seismic dataset acquired at the St. Ives gold camp in Western Australia.

### **3.3.7. Diffraction Energy**

In seismic data processing diffracted waves are often considered as noise, but they may contain valuable information about subsurface structure and media composition and could be used for imaging purposes (Landa and Keydar, 1998).

The diffractions occur when the radius of curvature of a layer's boundary is less than a few wavelengths and the interface is truncated, in presence of faults, pinchouts, fractures or any other types of heterogeneities. In these cases the energy from a seismic source is diffracted from the objects rather than reflected or refracted. Diffractions can be described in the first approximation by using the Huygens-Fresnel principle. According to this principle, in considering the propagation of a wave, every point of the medium that has been reached by the wavefront becomes a secondary point source and radiates energy (Figure 3.9). Diffractions are detected most clearly in those cases when the size of the obstacles is comparable to the wavelength.

The travel-time curve of the diffracted wave from a scattering point is given by the hyperbolic equation:

$$T_{diff} = \frac{2}{V} \sqrt{H^2 + \Delta X^2}, \quad (3-7)$$

where  $T_{diff}$  is the arrival time of the diffracted wave,  $\Delta X$  is the horizontal offset from the scatterer,  $H$  is the depth to the scatter point,  $V$  is the velocity.

In the case of edge diffractions, two phenomena are observed: the phase change of 180 degrees on either side of the reflecting edge and the 50 per cent amplitude decrease at the edge compared to the reflected part (Trorey, 1970). By phase reversal, a diffracted wave from an edge divides into two parts based on the polarity: the off-end part from the reflector with one polarity, and the part below the reflector (the shadow zone) with the opposite polarity (Figure 3.9a). This phase-reversal feature can be used in order to distinguish the diffractions produced from the edges.

Seismic imaging using diffraction energy is an important complement to the conventional processing to improve structural images in terms of detection of the small scale faults, fractures, formations' unconformities and any scattering heterogeneities.

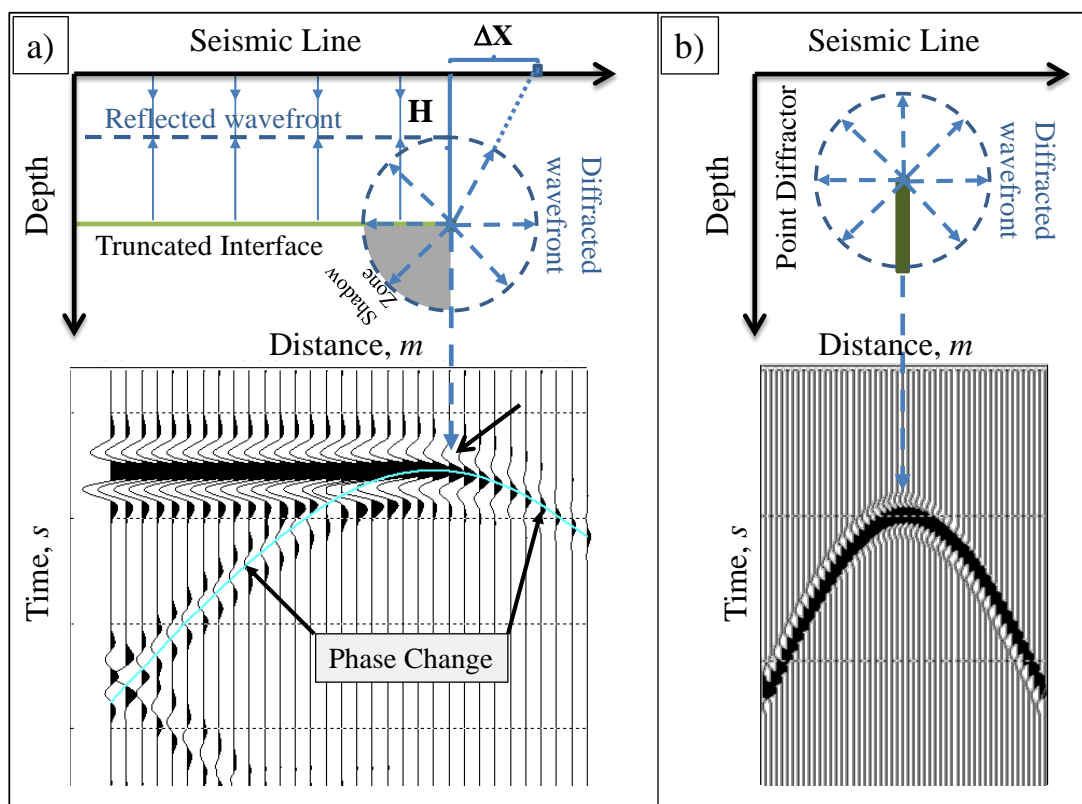


**Figure 3.9.** Basic principle of the diffractions. 2D models and computed seismic records for coincident sources and receivers. a) Diffraction from the truncated interface (edge diffraction). b) Diffraction from the scatter point (sharp obstacle) (Trorey, 1970).

The study involves the development of the 3D poststack imaging algorithm with diffractions. The abilities of the method to detect the subvertical structures and increase the signal to noise ratio of seismic data have been tested on a synthetic dataset and demonstrated on a number of 3D field seismic volumes from various hard rock camp sites.

### 3.3. Hard Rock Seismic Summary

Mineral exploration is commonly dealing with complex geological conditions and facing a wide scope of challenges discovering new deposits. Geophysical methods provide great support for the mining industry in the investigation process of hard

rock provinces. Seismic techniques enable one to estimate reliable models of subsurface structure with the highest resolution among all other methods and are capable of evaluating the physical properties of rock formations. Seismic methods have a long historical record of successful applications in hard rock environments. Despite the fact that seismic techniques are still not a standard tool in mining exploration, in recent years they have been involved more and more in mineral targeting and show effective results in resources detection.

Mineral environments comprise various types of rocks with different physical properties that give an opportunity for geophysical methods to distinguish them and study their settings. Seismic methods rely on a contrast in densities and velocities. Seismic exploration techniques have a large variety of tools which can be implemented to solve particular tasks in investigation of subsurface media. Many different kinds of waves (surface, refraction, reflection, and diffraction) emerge under an impact of a seismic source and during the following propagation through the geological strata. Each of them can be efficiently used for a certain exploration problem.

Seismic techniques based on analysis of surface waves and refracted waves can provide inexpensive solutions for near surface tasks in mineral exploration such as investigation of the regolith structure and estimation of the geotechnical properties of the shallow rock formations. Seismic reflection methods are capable of delivering the most accurate 2D and 3D images of deep geological structure and can evaluate the physical properties of rocks. Seismic approaches utilizing the distribution of diffraction energy enables one to detect subvertical structure and alterations and trace fault and fracture zones. The following chapters will cover the research aspects of the application of the whole arsenal of seismic exploration tools to image hard rock environments.

## **4. Near Surface Seismic Imaging for Hard Rock Environments**

### ***4.1. Regolith Exploration***

The exploration of regolith cover is one of the significant parts of the mineral exploration. The regolith is the unconsolidated and chemically altered cover that overlays fresh bedrocks. Regolith consists of re-deposited older rocks, which have been eroded and weathered, and it is charged with biota, water and gases (Scott and Pain, 2008). The thickness of the regolith varies from a few metres to over several hundred meters depends on the age of the surface formations, tectonic and climate history. Weathering processes in the regolith cause the formation of some commodities, such as bauxite, lateritic nickel-copper deposits, lateritic and saprolitic gold mineralizations, industrial materials and others (Butt et al., 2000). Knowledge about the regolith structure is necessary for discovering mineral sites and designing the mine excavation and production. In this chapter capabilities and effectiveness of the seismic refraction and MASW methods for regolith characterisation have been investigated on a dataset acquired over an IOCG deposit at the mine site in South Australia.

### ***4.2. 2D Seismic Experiment at Hillside Mine Site***

An experimental seismic survey was designed by researchers from Curtin University and conducted at Hillside mine site, located on the Yorke Peninsula (South Australia) 12 kilometres south of the Ardrossan township (Figure 4.1), with help from Adelaide University and under supervision of REX Minerals.

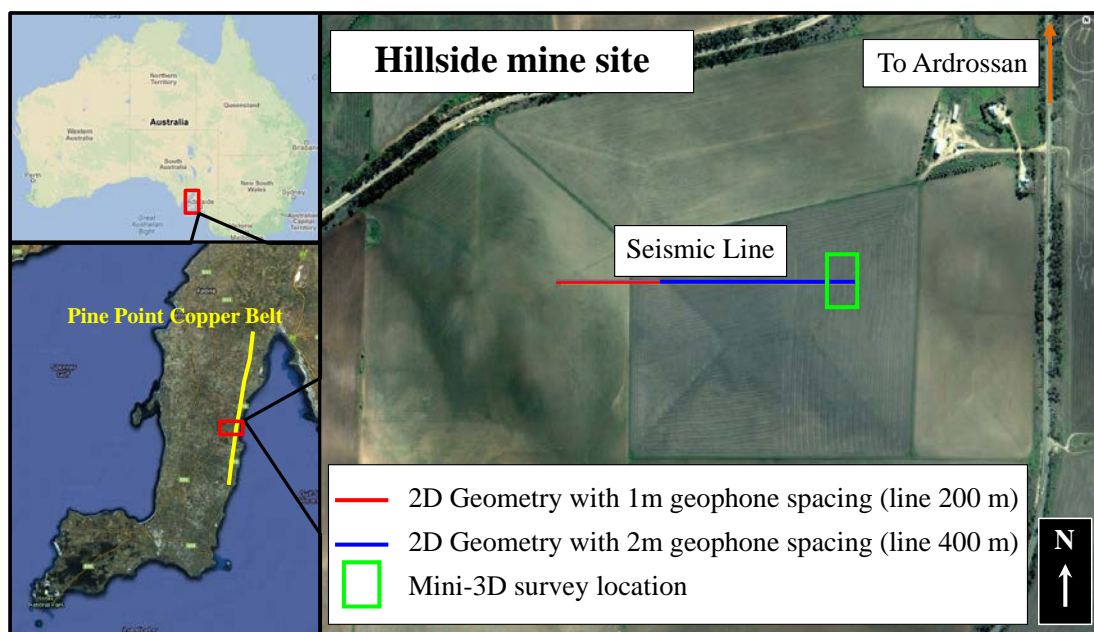


**Figure 4.1.** Location of the seismic survey at the Hillside mine site (South Australia). Red and blue lines represent the position of a 2D seismic line with 1 m and 2 m geophone spacing, respectively. Green box shows the position of the mini-3D seismic survey (Images provided by Google Earth 2011).

Hillside deposit is located in the Gawler Craton geological province. The Archaean to Palaeoproterozoic Gawler Craton hosts Australia’s largest historical copper mines such as Olympic Dam, Prominent Hill, Carapateena and Hillside polymetallic copper-gold deposits. All of these districts are IOCG systems. Most of the fresh rocks in the Gawler Craton are covered by a sequence of regolith rock. This overburden effectively hides deposits from exploration. The Hillside mineral occurrence is one of many targets that can be found along the Pine Point Copper Belt on the Yorke Peninsula (South Australia) (Figure 4.1). The copper-gold mineralization is associated with main structures, the Zanoni, Parsee, Songvaar and Dart, which are broadly defined by a magnetic anomaly (Figure 4.2). The thickness of Tertiary and Cambrian calcareous sediment cover is from 5 to 30 meters (Lowe, 2009).

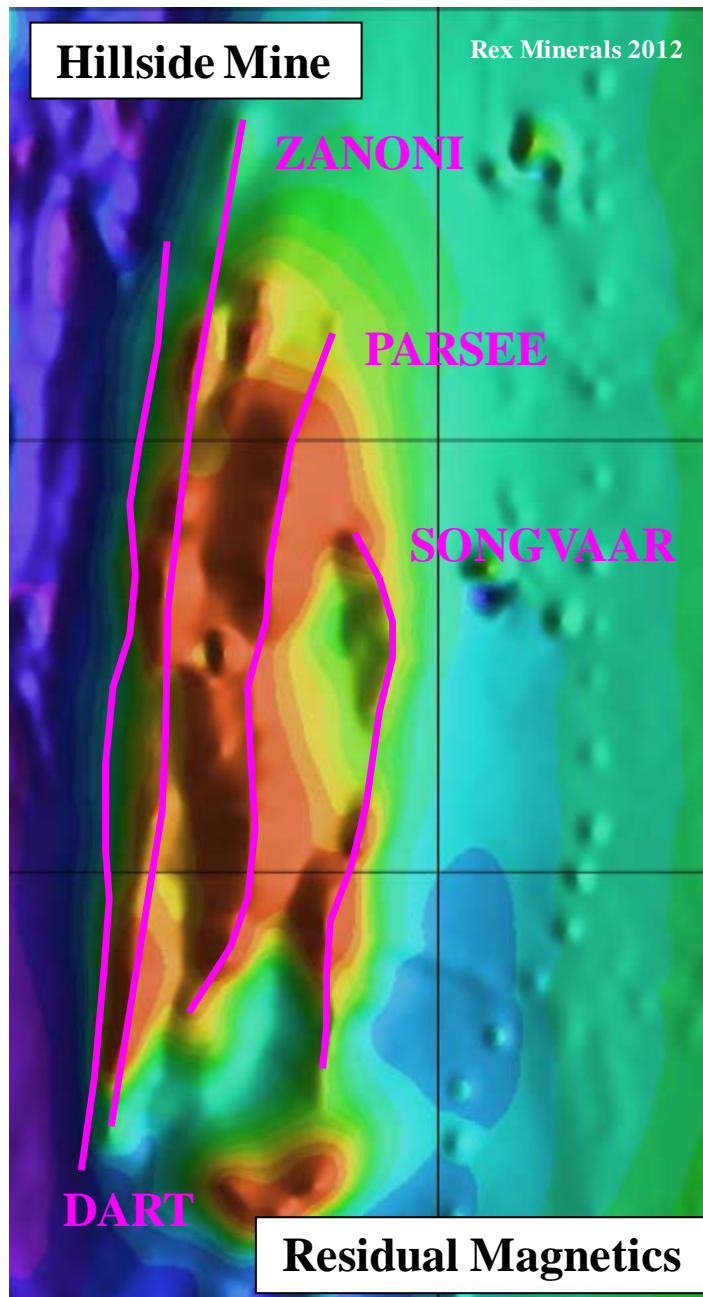


*Figure 4.2. Aeromagnetic survey of the Hillside camp. Line spacing of the magnetic survey is 25 m. Purple lines identify mineralized fault zones.*

The primary copper mineralisation at Hillside is dominated by the copper mineral chalcopyrite, which is typically found in association with magnetite and pyrite, with a minimal presence of hematite. Geology represents folded Paleoproterozoic metasediments, metavolcanics and meta-igneous rocks intruded by granite and gabbro. There is a strong regional metasomatic albite-biotite-actinolite-magnetite

alteration and overprints of local chlorite-potassium feldspar-hematite-magnetite-pyrite alterations. The main magnetite breccia structures dip steeply to the west and high grade primary copper lenses dip steeply to the east within magnetite zones. The estimated true widths of massive copper lenses on the Zanoni mineralization zone are from 1 to 30 meters (Lowe, 2009). Total estimated resources of the Hillside project is 330 million tonnes at 0.8% copper equivalent with shallow high grade (< 200 m) 29 million tonnes at 1.2% copper equivalent (Twining, 2012).

#### **4.2.1. Seismic Acquisition**

The main objective of the Hillside seismic experimental survey was to test the performance of high resolution seismic methods when using a small number of active seismic channels and a portable weight-drop in a hard rock environment to image a regolith structure. Proving such a concept would enable rapid and inexpensive surveys which could allow for its widespread application for exploration of certain type of mineral deposits by using dynamic seismic acquisition systems such as land streamers or ‘draggable’ geophone arrays.

Several seismic technologies were applied during field operations such as: Surface Waves, Refraction Profiling and Reflection data. By using a low-power seismic source, a small number of channels and specific survey geometries it was possible for a crew of 4 people to acquire, in five days (including mobilization), high resolution 2D and a mini 3D surveys. Here only the 2D data of Multichannel Analysis of Surface Waves (MASW) and Refraction Profiling were considered for research of near surface seismic imaging of the regolith structure.

The 48-channel seismic system EX-6 with 10 Hz geophones was used to collect data. The distributed system consists of several acquisition units, each of them collecting 6 channels of data. A 45 kg accelerated weight drop was assembled on a trolley and used as a source of seismic waves. This source was easily moved by two people and was suitable for a highly repeatable shooting (Figure 4.3). The Wireless Triggering Box (WTB) and piezoelectric sensor attached to a force spreading plate were used to synchronise shooting and recording.

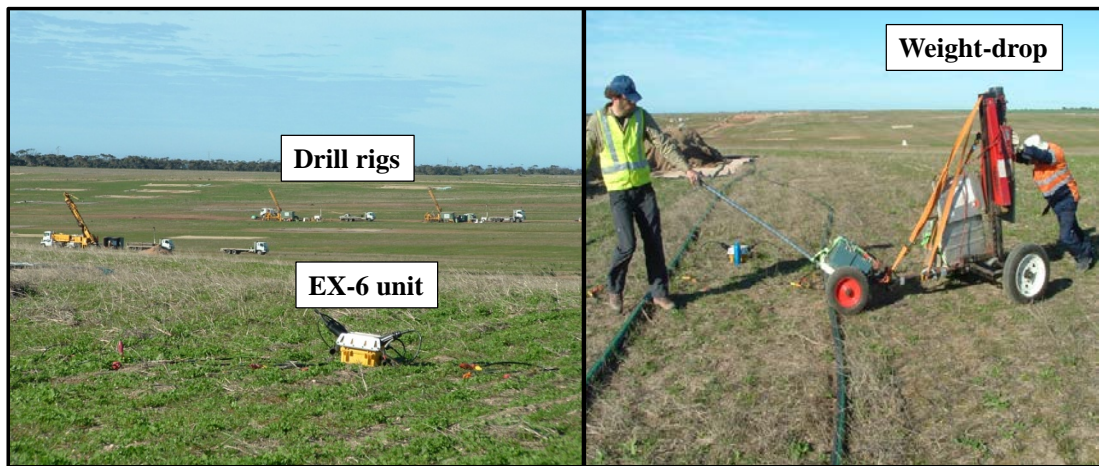


***Figure 4.3. Seismic acquisition at Hillside camp. Left panel: EX-6 unit. Right panel: Accelerated weight drop on a trolley.***

Two short 2D seismic lines were acquired along the same traverse with an overlap of approximately 50 m. The first 200 meters (Line 1) geophone spacing was 1 m, distance between shots was kept at 2 m. Each spread had 48 channels; the offset was 24 m from the first and the last geophone of the spread. Shots were fired through the spread and the spread was then moved by 24 channels. For the next 400 meters (Line 2) geophone spacing was 2 m; shot increment was 4 m (Figure 4.4). Same shooting pattern was implemented. The record length was 2 seconds; sample rate 0.5 ms. Three shots were stacked at each source position. The quality of acquired data was reasonably good for further processing and interpretation (Figure 4.5). The most prominent events on the seismograms correspond to surface and refraction waves.

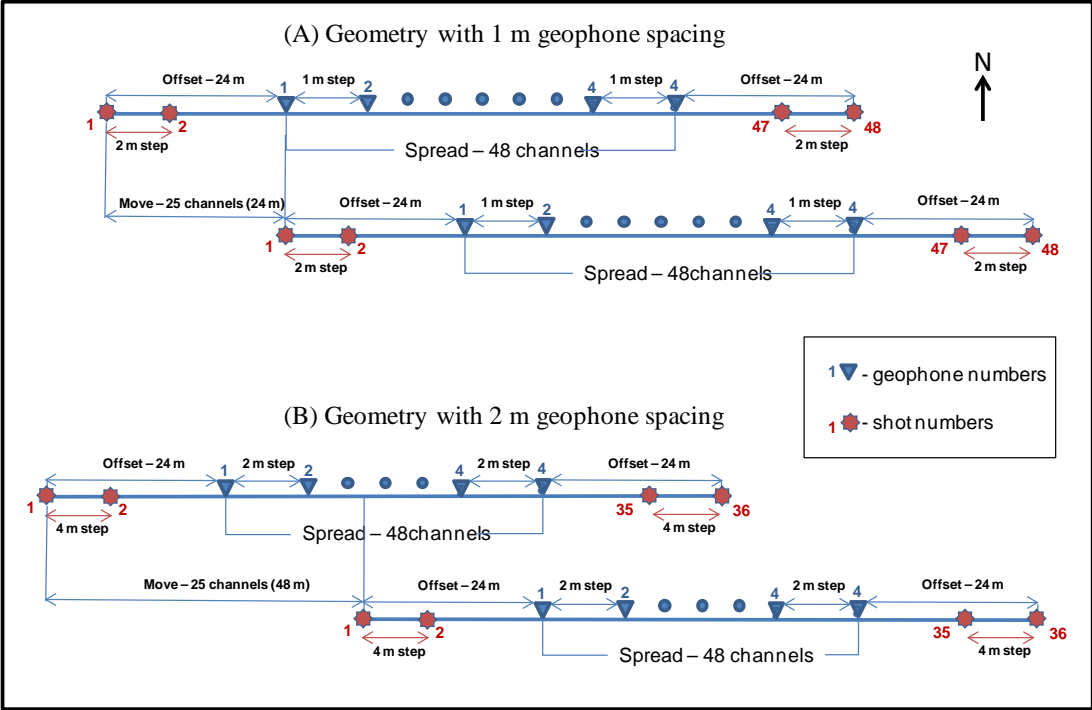
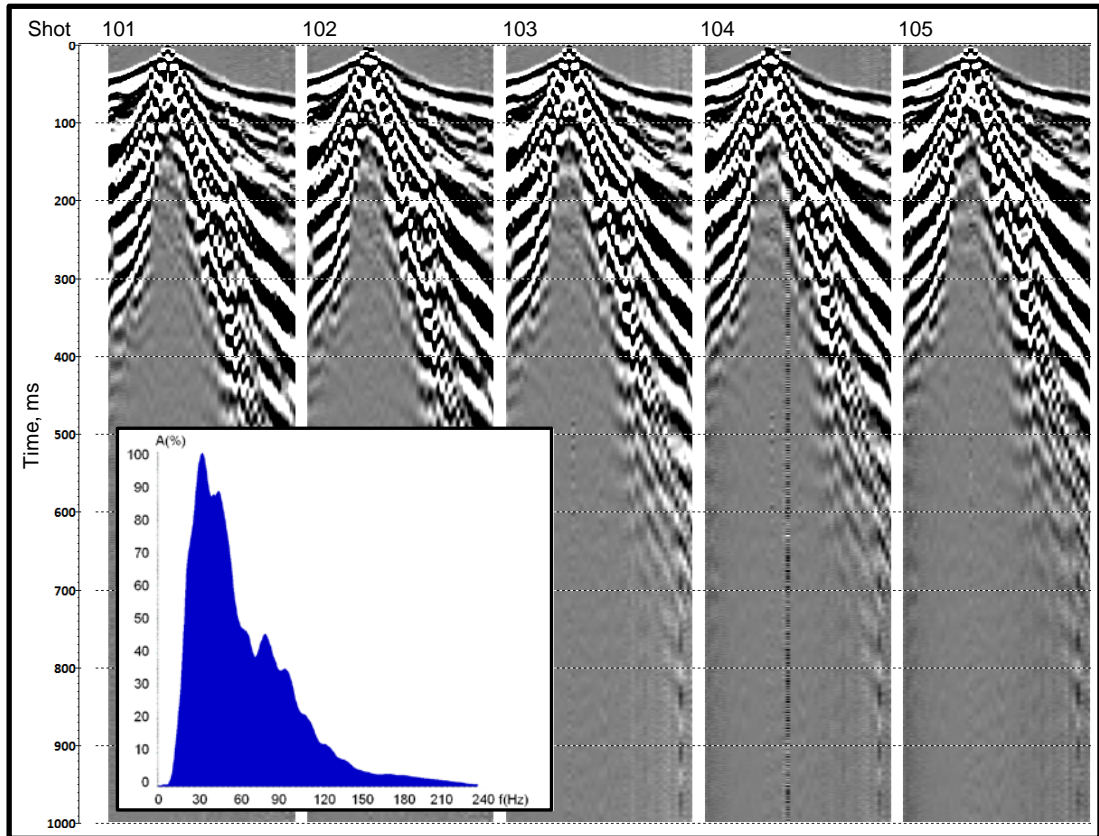


Figure 4.4. 2D Survey geometries. (A) Geometry of Line 1 (1 m geophone spacing); (B) Geometry of Line 2 (2 m geophone spacing).



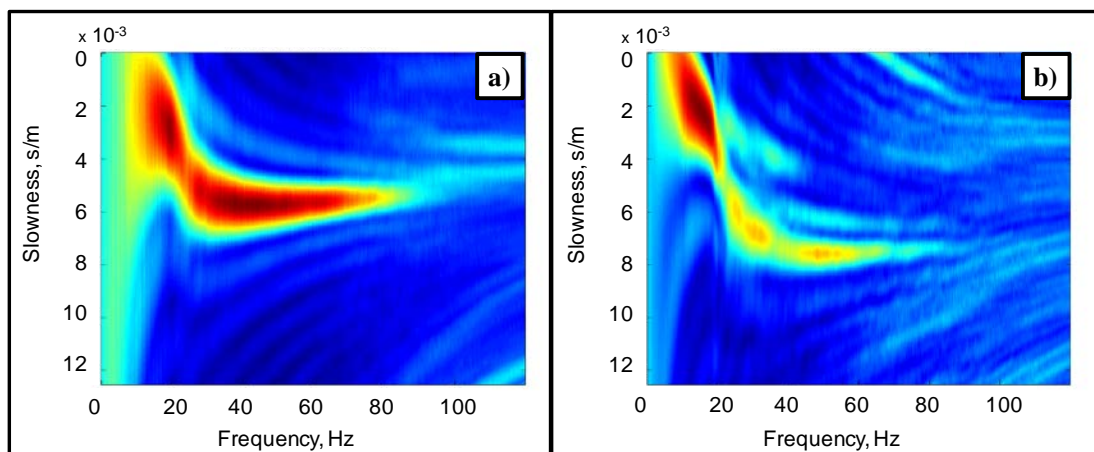
*Figure 4.5. Examples of five 2D raw shot gathers of Line 1 and an example of amplitude spectrum of the first shot gather.*

#### **4.2.2. Multichannel Analysis of Surface Waves (MASW)**

MASW is the seismic method which uses information about a propagation of surface waves to define near-surface structure and rock properties. The main idea of this technology is based on the fact that longer wavelength surface waves influence deeper depths of subsurface materials, so lower wave frequencies correspond to the deeper layer. Ultimately, using the dispersion of wave frequencies with depth, we can get an S-wave velocity section, which will describe a subsurface structure in terms of rock's properties. Depth of investigation usually does not exceed the first ten meters.

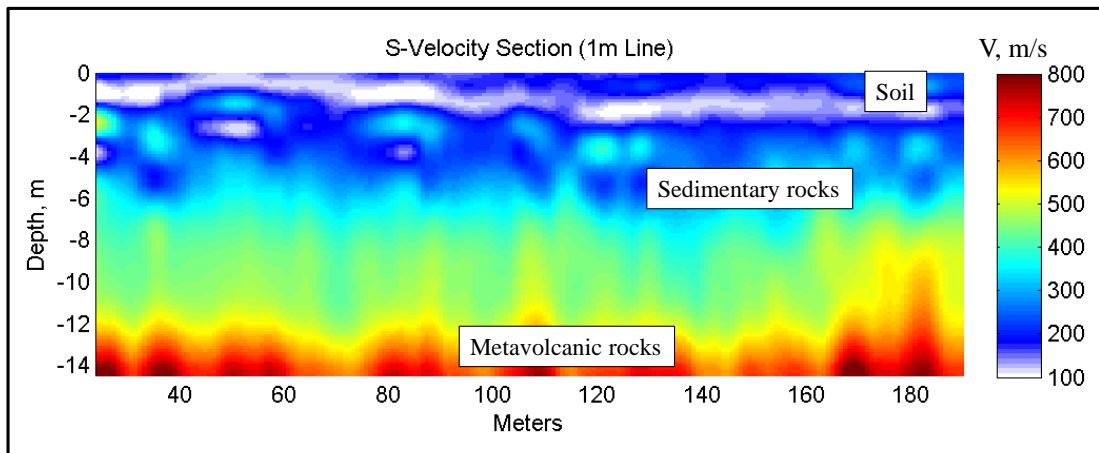
The first processing step involved loading seismograms into a database and assigning survey geometry. Preconditioned seismic data have been exported from the database for the next processing stage. The slant-stack method in frequency domain, presented

by Park et al. (1999), was utilized to calculate the phase velocity spectra for every receiver position; to improve signal to noise ratio the stacking of slowness spectra (Neducza, 2007) was applied for a given receiver window over all shot points. Figure 4.6 shows the examples of two dispersion curves of slowness for both 2D seismic lines. Then, the dispersion curves were picked from slowness spectra and exported for the inversion. The inversion of the surface wave dispersion curves was carried out by the method proposed by Xia et al. (1999) using SurfSeis software to produce a shear-wave (S-wave) velocity profile in depth. S-wave velocity sections show changes of the velocities with depth along survey lines. These changes correspond to the different types of subsurface materials and that information can be used to obtain elastic properties of rocks.

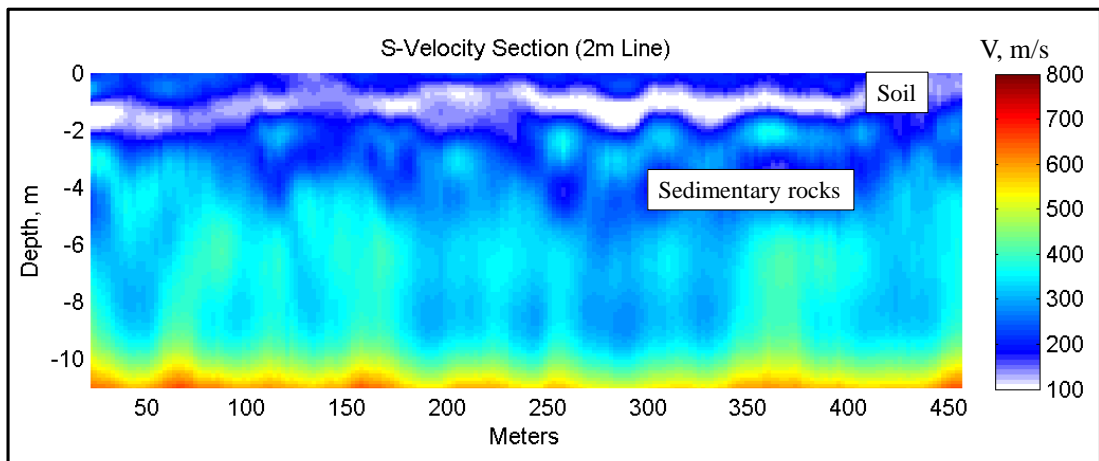


**Figure 4.6. Example of dispersion curves of slowness for both types of geometry: a) 1 m geophone spacing and b) 2 m geophone spacing.**

Two 2D seismic lines recorded with 1 and 2 m geophones spacing were analysed independently. The central frequency of seismograms is approximately 30 Hz (Figure 4.5). The concept of surface waves inversion is based on the fact that different frequencies penetrate to different depths; the low frequencies have greater depth of penetration. Thus one would like to utilise as low frequencies as possible in order to invert to greater depths. In our case the weight drop does not produce low frequencies with sufficient magnitude and geophones used were with natural frequency of 10 Hz, instead of usual 4.5 Hz used for this type of surveys. Consequently the maximum depth of penetration achieved was 15 meters.



**Figure 4.7.** *S-Velocity section for 1 m geophone spacing line.*



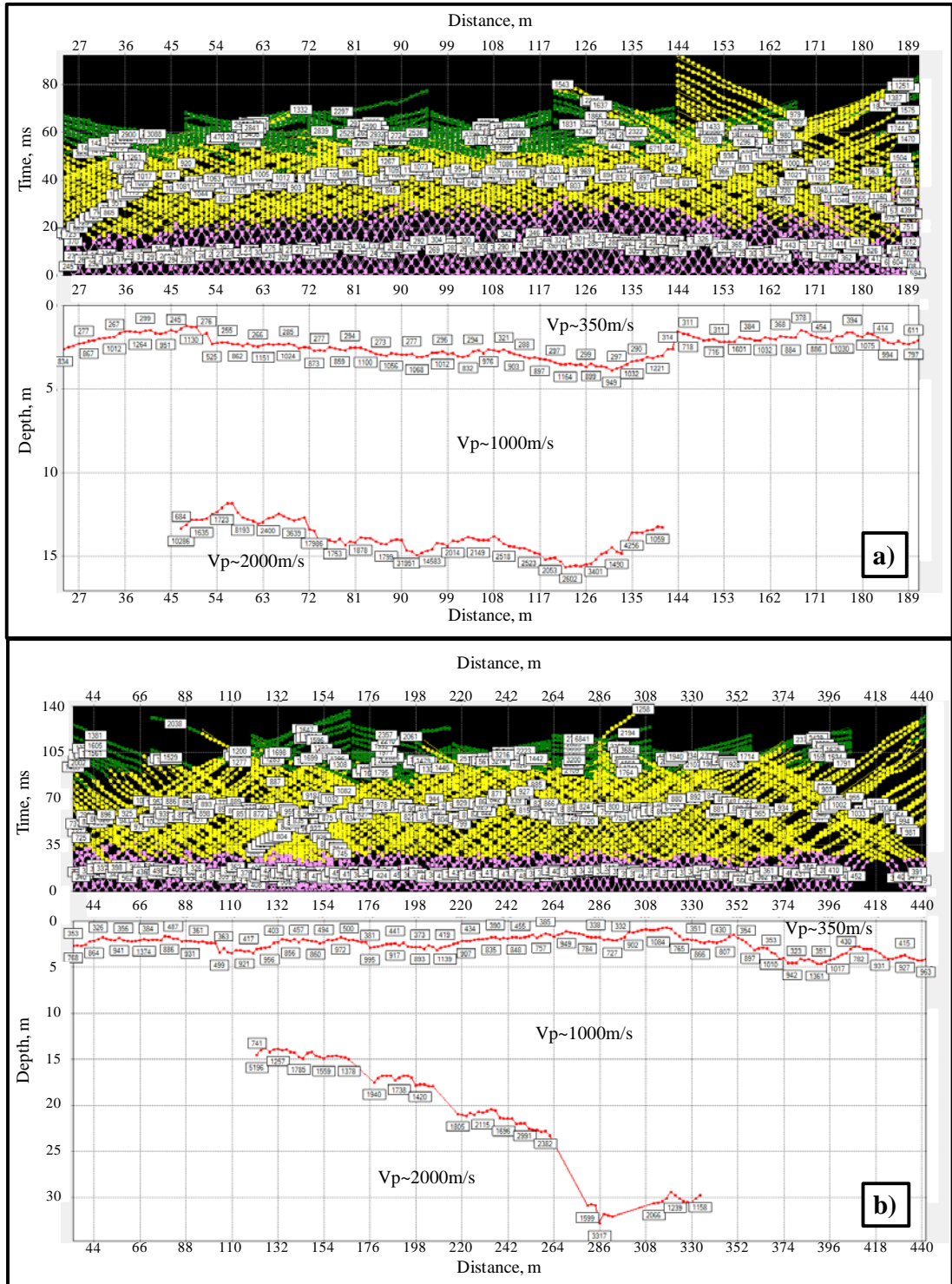
**Figure 4.8.** *S-Velocity section for 2 m geophone spacing line.*

Figure 4.7 and Figure 4.8 show inverted S-wave velocity sections for two lines 1 and 2. A low velocity layer at approximately 1-2 meters depth can be clearly observed and identified as a soil layer. Then surface wave velocities gradually increase with depth that possibly corresponds to sedimentary rocks (sandstones); a sharp rise of velocity values at approximately 12 – 14 meters depth could be related to metasediment-metavolcanic rocks.

### **4.2.3. Refraction Data Analysis**

Refraction seismic methods are based on the measurement of travel time of seismic waves refracted from subsurface interfaces of different velocities. This technique allows us to define boundaries of layers and estimate propagation velocities of P-waves of these layers. Typical velocity model for refraction survey assumes that P-waves move faster in the deeper layers. So, the first breaks on seismograms, which returned back to the surface from subsurface interfaces, correspond to refracted waves. When energy radiates out from a shot point, firstly it is travelling directly through the upper layer (direct arrivals), and also travelling down to and then laterally along higher velocity layers (refracted arrivals) before returning to the surface. This energy is detected on the surface using a linear spread of geophones spaced at regular intervals. After a certain distance from the source point, called the cross-over distance, the refracted signal is observed as a first-arrival signal at a seismogram (overtaking the direct arrival). Data of the travel-times of the direct and refracted signals provide information on the depth profile of the subsurface boundaries.

Field data were loaded to a database and geometry was assigned to the data. The first breaks were picked and edited prior to loading to 'Easy Refraction' software. This module analyses the travel time curves and performs a depth inversion. To reduce triggering delay errors, all time curves were reduced to a common time horizon before the inversion. 'Easy Refraction' module utilizes classical reciprocal method for the inversion (Hagedoorn, 1959). The method inverts for depth and shape of the refraction interfaces as well as the values of the P-wave velocities in the layers.



**Figure 4.9. Time curves and inversion results of refraction wave's analysis. a) For 1 m geophone spacing geometry; b) For 2 m geophone spacing geometry.**

Each line was processed separately. Travel time curves displayed distinctly different apparent velocities as colour coded in Figure 4.9. Travel time inversion

produced a three layer model. The first layer is approximately 2 m thick with average velocity of about 350 m/s, just higher than air wave velocity; the second layer, dipping to the east, has a velocity of about 1000 m/s. The third layer has average velocity of about 2000 m/s. The depth of this layer varies from 14 m to 30 m to the east.

There is a good correlation between two independently analysed seismic lines. Interpreted depth-velocity profiles for both lines are shown in Figure 4.10.

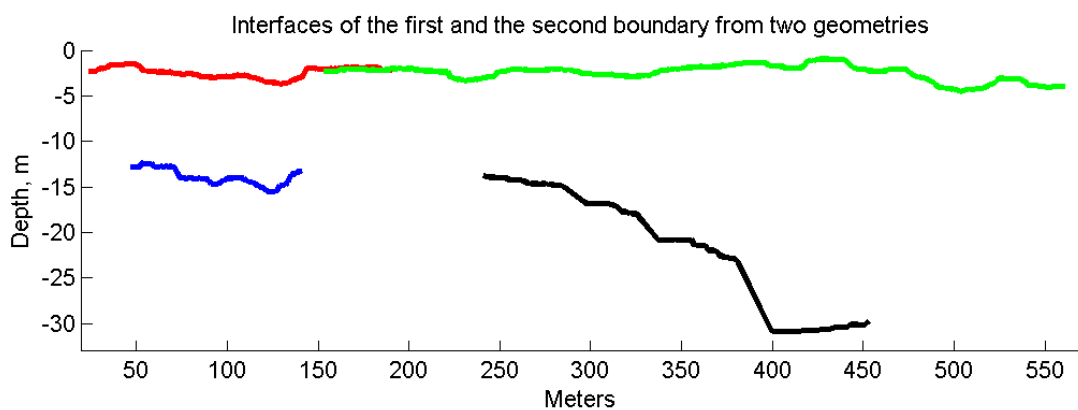


**Figure 4.10.** Refraction data analysis results for two lines. Red and green lines correspond to the bottom of the first layer; blue and black lines correspond to the top of the third layer.

#### 4.2.4. Integrated results of MASW and Refraction Data Analysis

Integrated interpretation of the regolith structure was performed relying on information obtained from both seismic techniques: surface and refracted waves. Layers from P-wave refraction data were subsequently overlaid onto shear velocity profiles obtained before using MASW analysis (Figure 4.11 and Figure 4.12). There is a reliable correlation between the inversion results of two seismic methods. For both cases the upper refraction boundary repeats the shape of the low-velocity layer observed in the S-velocity section.

A geological section of the regolith structure reconstructed from 2D near surface seismic data is shown in Figure 4.13. The first layer represents unconsolidated soil deposits, which are characterized by low seismic velocities of P- and S-waves; the

second layer corresponds to unconsolidated sediments; the third one represents metasediments-metavolcanics rocks. The results are consistent with the information from specific gravity and lithological logs from neighbouring boreholes.

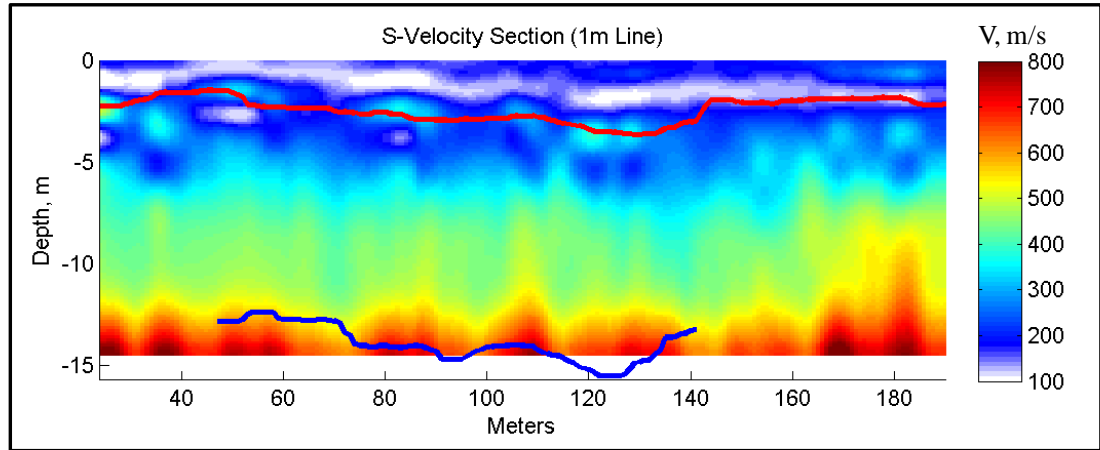


**Figure 4.11.** Refraction interfaces and S-velocity section for 1m geophone spacing geometry. Red line represents the bottom of the first soil layer; blue line shows the top of the third metasediment layer.

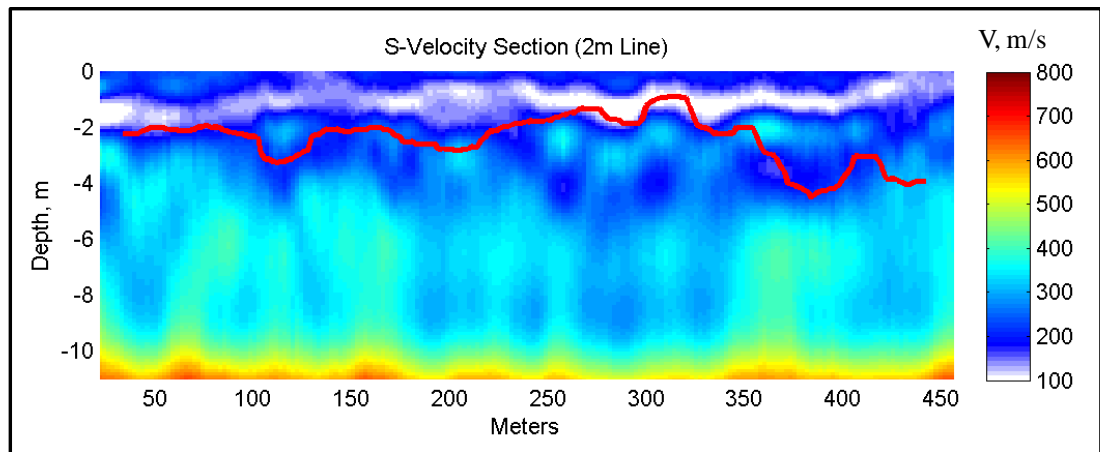


**Figure 4.12.** Refraction interfaces and s-velocity section for 2 m geophone spacing geometry. Red line represents the bottom of the first soil layer.

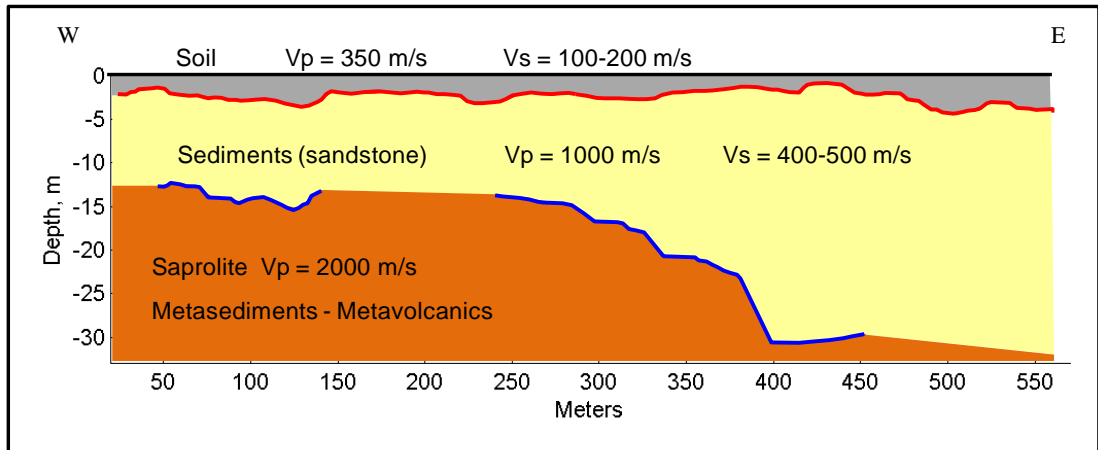


**Figure 4.13.** Geological section of the regolith structure obtained from seismic data.

Within the presented near surface seismic experiment refraction tomographic inversion was done to obtain P-wave velocity model (Yavuz et al., 2012) (Figure 4.14). From P- and S-wave velocity profiles, assuming constant densities the elastic parameters can be computed. The following dynamic parameters were estimated: Young's modulus, Poisson's ratio, Bulk modulus and Shear modulus. These elastic attributes could be used for geotechnical purposes in the mine design and development.

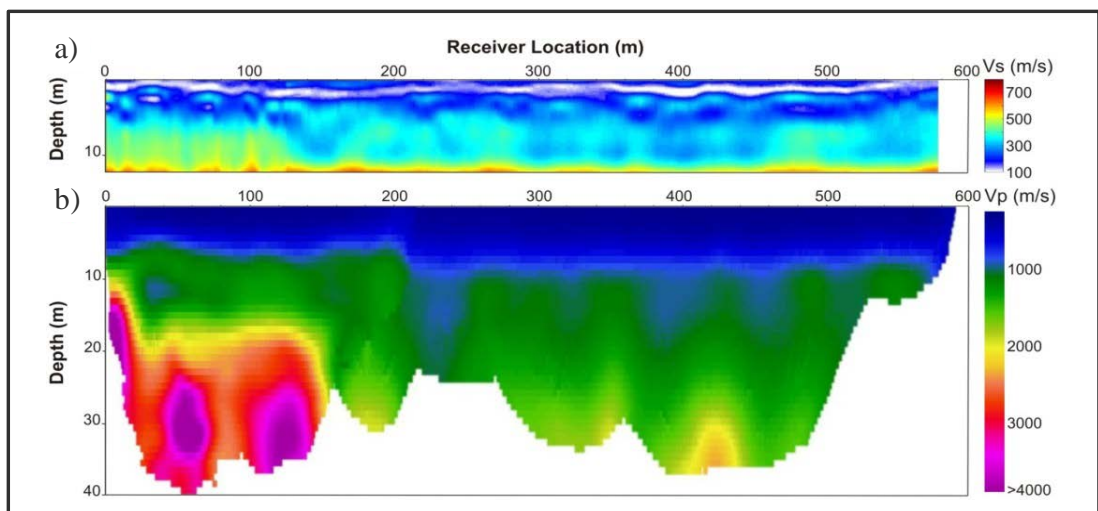


**Figure 4.14.** a) Shear wave profile obtained from MASW and b) P-wave velocity obtained from refraction tomography (Yavuz et al., 2012).

### ***4.3. Near Surface Seismic Imaging Summary***

The presented near surface experiment combined different seismic technologies: MASW and refraction wave analysis, to delineate regolith structure at Hillside mining camp. The main objective of this research study was to test if a cost-effective seismic survey can provide useful information to mining operations on certain mineral deposit styles.

Within short time frame (5 days including mobilization), a small seismic crew acquired diverse 2D seismic data. Simultaneous acquisition of both refraction and surface wave data proved to be useful for the regolith exploration. Good agreements were achieved between P and S-wave velocity profiles. Moreover, geotechnical parameters of regolith were recovered using the refraction tomographic inversion results. Such comprehensive information about regolith can support different mining tasks from exploration of new shallow deposits to designing and development of excavation plans and construction of pits.

The obtained results suggest that there is high potential for the application of seismic methods for exploration of the regolith at hard rock sites. Moreover, considering the quality of the results obtained with low channel count and low fold the application of dynamic acquisition systems such as land streamer or druggable geophone strings may have the potential for providing useful information for exploration and mine planning at hard rock camps.

## **5. Velocity Independent Imaging for Hard Rock Environments**

A velocity model for the subsurface is an essential component in most conventional seismic migration algorithms. However, velocity information is often unavailable, and obtaining this information from the seismic itself may be a difficult task. This is often the case in hard rock environments, which include complex faults, fracture zones, steep dips and rock alterations. Additionally, this type of environment is often characterized by low reflectivity and high ambient noise, since most of the seismic exploration for minerals is conducted across “brown” fields, in an attempt to define extensions of existing mineralizations. Consequently, defining a velocity field over sub-vertical structures and complex, fractal boundaries with intrinsically low signal-to-noise ratio and lack of borehole information is difficult and alternative data processing strategies need to be employed. For such situations, imaging methods that do not require an input velocity model are desirable.

### ***5.1. Velocity-Less Prestack Time Migration***

In the past few decades, many researchers have published results from velocity-independent seismic time migration techniques. The majority of these imaging approaches are based on the evaluation of the local dips of seismic events (horizontal slownesses). Several papers that discuss the use of slownesses for constructing velocity independent imaging have been published during the last 75 years. The concept of controlled directional sensitivity, e.g. estimating local slopes from pre-stack data and using them to estimate migration velocities and locations, first appeared in Rieber (1936) and Riabinkin (1957). Sword Jr (1987) summarized these concepts as a method of controlled directional reception. The idea of velocity independent imaging for the migration of horizontal reflectors was suggested in a paper by Ottolini (1983b); he presented a method for building the image by applying the time dips of the seismic data at every point on the registered data. Fomel (2007) expanded Ottolini’s concept; he used information about local event slopes from common-midpoint and common-offset domains to obtain the complete reflection

geometry. Cooke et al. (2009) used horizontal slownesses not only to perform time imaging and estimation of velocities, but also for the suppression of multiples. Bóna (2009) presented a velocity-less prestack time imaging algorithm, where only one (common-shot or common-receiver) domain is required; however he needed to calculate both the first and second derivatives of the travel-time.

In this chapter a velocity-less prestack time migration approach has been studied on application to the hard rock seismic exploration. Herein, the term – ‘velocity-less’ – defines the prestack imaging algorithm with simultaneous estimation of a velocity model. An application of the method of controlled directional reception is discussed further. This prestack time migration algorithm does not require an initial velocity model. The presented algorithm is based on an estimation of horizontal slownesses (local event slopes) that are used to produce the migration attributes (the location of the migrated events as well as the migration velocities). The calculated attributes allow us to map seismic amplitudes from the prestack data domain into the time migrated image.

### 5.1.1. Implementation of the Velocity-Less Algorithm

The examined prestack time migration algorithm is based on the assumption of hyperbolic offset-traveltime curves. This imaging technique relies on estimation of local event slopes for common-shot and common-receiver domains and obtaining the values of attributes: migration velocity ( $V$ ), vertical travel-time ( $t_0$ ) and horizontal coordinate of the migrated reflection point ( $x_m$ ). The equations for these parameters were derived for 2D geometry by Cooke et al. (2009) from the travel-time equation (double-square-root equation) for reflections in effective homogeneous media:

$$x_m = x_s - (x_r - x_s)p_s \frac{t - (x_r - x_s)p_r}{t(p_r - p_s) + 2(x_r - x_s)p_s p_r}, \quad (5-1)$$

$$V^2 = \frac{x_s - x_m}{tp_s} + \frac{x_r - x_m}{tp_r}, \quad (5-2)$$

$$t_0 = \frac{|x_s - x_m|}{V} \sqrt{\frac{1}{V^2} - p_s^2} \quad (5-3)$$

Here,  $p_r$  and  $p_s$  are values of horizontal slownesses measured in common-shot and common-receiver gathers respectively;  $x_s$  and  $x_r$  are the locations of source and receiver;  $t$  is the travel-time of the migrated event (Figure 5.1). The equations (5-1) – (5-3) represent a system of three equations with three unknown migration attributes. For every event in the time domain, the travel-time and locations of shots and receivers are known, and  $p_r$  and  $p_s$  can be derived from seismic data. The solution of the presented system allows us to obtain the velocity model and at the same time the output migration locations  $t_0$  and  $x_m$  for every sample from the input dataset (Figure 5.1). As a result, every amplitude of each trace from the input dataset has a definite pair of image coordinates  $t_0$  and  $x_m$ . To create the final result every single input amplitude sample has been added onto a single point of the migrated image using the coordinates given by expressions (5-1) and (5-3). In contrast to the Kirchhoff prestack time imaging, the reflection amplitude is not distributed over an ellipse defined by velocity and geometry; instead it is mapped directly onto the calculated image point. Thus, amplitude and phase corrections (Yilmaz, 2001), which account for the angle dependence of amplitudes (obliquity factor), spherical spreading, and wavelet shaping, were not included.

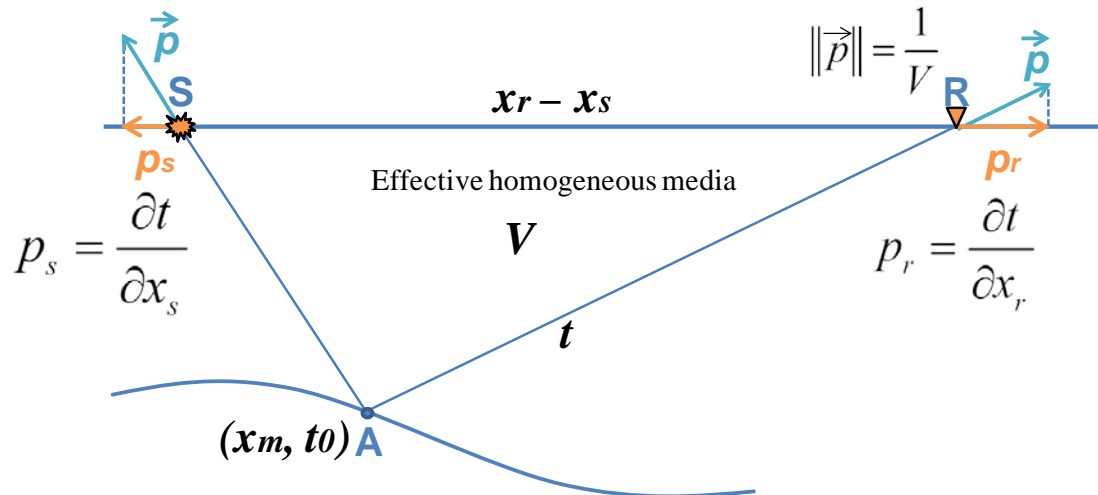


**Figure 5.1.** Horizontal slownesses  $p_r$  and  $p_s$ .  $S$  is a shot point,  $R$  is a receiver location,  $A$  is a reflection point.

In the special case of a local slope equal to zero the equations for the migration attributes was derived from geometrical considerations. When  $p_s$  approaches zero,

two equations could be defined from the geometry set up (Figure 5.2). The expression for the path SAR:

$$Vt = \sqrt{\frac{V^2 t_0^2}{4} + (x_r - x_s)^2} + \frac{Vt_0}{2} \quad (5-4)$$

From the similarity of triangles the following expression is defined:

$$V \sqrt{\frac{V^2 t_0^2}{4} + (x_r - x_s)^2} = \frac{(x_r - x_s)}{p_r} \quad (5-5)$$

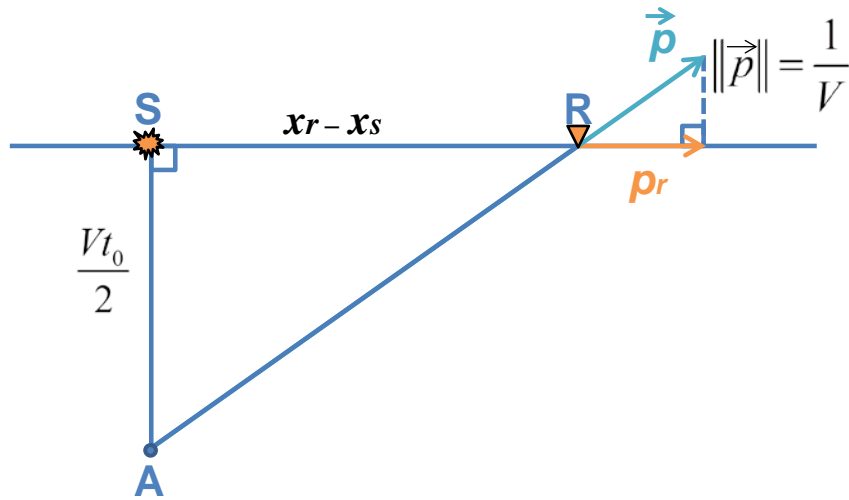


**Figure 5.2. Geometry set up. S is a source location, R is a receiver location, A is a reflection point.**

From equations (5-4) and (5-6) the attributes of a velocity and vertical travel-time could be easily derived. The following system represents three expressions for the attributes in case  $p_s$  equal to zero:

$$x_m = x_s, V^2 = \frac{2d}{tp_r} - \frac{d^2}{t^2}, t_0 = \frac{V^2 t^2 - d^2}{2tV^2}, \quad (5-6)$$

Here  $d = x_r - x_s$ .

From the similar geometrical set up, when  $p_r$  is equal to zero, the migration parameters are obtained from the following equations:

$$x_m = x_r, V^2 = -\frac{2d}{tp_r} + \frac{d^2}{t^2}, t_0 = \frac{v^2 t^2 - d^2}{2tV^2}. \quad (5-7)$$

The method is not designed to handle the case of both local slopes  $p_r$  and  $p_s$  approaching the same value, which corresponds mostly to the zero offset case; the zero-offset data are excluded from the migration process. When  $p_r$  and  $p_s$  have equal values, there is not enough information to recover the location of the reflection point.

A good estimation of the values of horizontal slownesses  $p_r$  and  $p_s$  is necessary for this migration algorithm. There are a number of techniques used to calculate the local event slopes for every point in the seismic dataset. Ottolini (1983a) suggested the local slant stack method; Fomel (2002) described an extension to a plane-wave destruction algorithm of (Claerbout, 1992); Schleicher et al. (2009) further extended the method of plane-wave destructors. The algorithm that was selected is based on a semblance analysis (Neidell and Taner, 1971) of local slant stacks (Harlan et al., 1984; Ottolini, 1983a). This algorithm gives the most stable and robust data for determining local event slopes.

The estimation of local event slopes is implemented by using the semblance approach. The horizontal slownesses  $p_s$  and  $p_r$  are computed as the spatial components of a normal vector to the tangent plane of the travel-time surfaces. In particular, the algorithm is implemented as follows. For every trace in the shot-receiver space, the neighbouring traces within a certain radius ( $R$ ) are selected. Then for each pair of local slopes  $p_s$  and  $p_r$  from a specified range, the corresponding time shifts for each of the selected traces are computed and the semblance of the time-shifted traces in a chosen running time window is calculated. For each sample the slopes corresponding to the maximum semblance are found. These slopes correspond to the values of slownesses in common-shot and common-receiver gathers  $p_s$  and  $p_r$ . The described implementation does not require reciprocal shot-receiver geometry (Cooke et al., 2008) and can handle any 2D seismic acquisition setups.

Hard rock seismic data often have low signal to noise ratio and complex geology structure with a lot of steeply dipping objects. To increase signal to noise ratio, the additional summation along the estimated local slopes is introduced prior to migration of the input sample onto the final image. For geometries with conflicting

dips, the algorithm selects the dip that corresponds to the maximum of the estimated semblance. The values of  $p_r$  and  $p_s$  are always associated with the same dipping event because they are projections of the same normal vector on the fitted tangent plane (this might not be the case if  $p_r$  and  $p_s$  are estimated independently).

## ***5.2. Application to the Basic Models***

The presented velocity-independent imaging algorithm has been tested on several 2D synthetic models of varying complexity. First of all, to test the accuracy of the approach, the algorithm was applied to two convolution models: a dipping reflector and a syncline model with constant velocities.

The first example is a dipping reflector. To construct the seismograms, a zero-phase, 30 Hz dominant frequency wavelet was convolved with spike-traces of unit amplitude. The shot-gathers were calculated for two hundred receivers and shots using a ray-tracing method; the spacing between both receiver and shot positions was 10 m; shots were located in the same position as the receivers. The velocity of the upper medium was 3000 m/s. The dipping angle of the reflection interface was  $20^\circ$ . One-second long seismic traces were computed. As noted above, the horizontal slownesses were estimated by using semblance. Using these values of the horizontal slownesses and the arrival time of each sample, the migration attributes (velocity ( $V$ ), vertical travel-time ( $t_0$ ) and horizontal coordinate ( $x_m$ )) were calculated. The attributes  $t_0$  and  $x_m$  define the location of migrated data; each sample was placed in the final image in accordance with these two parameters. Dimensions of the migrated image were defined by a half of the receiver increment in spatial direction and half of the sampling rate in temporal direction.

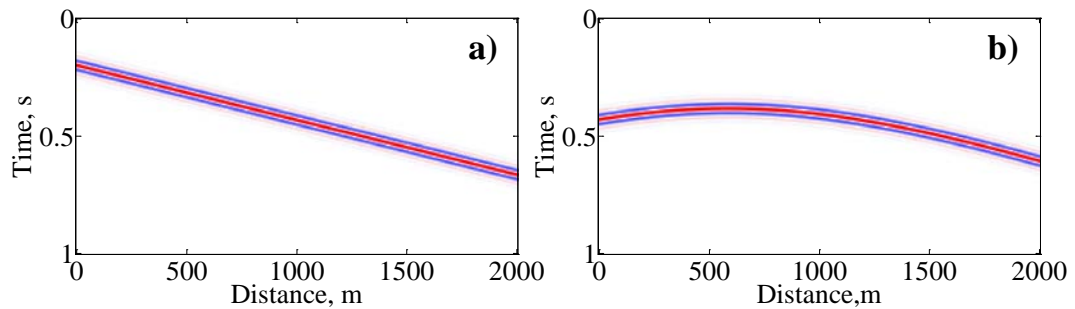


**Figure 5.3. Convolution model of a dipping interface. a) True position of a dipping interface in time scale and b) example of a shot gather at 1000 m.**

The real position of the dipping interface in time domain is shown in Figure 5.3a; Figure 5.3b shows an example of a shot gather of the examined model. In this case the local event slopes were extracted using a radius of 25 m that gave up to 21 traces to analyse in the spatial dimension and a 5 sample window in the temporal direction. An example of the resulting horizontal slowness ( $p_r$ - and  $p_s$ -values) is given in Figure 5.4b and 5.4c for a fixed source at location 1000 m. Figure 5.4a shows a distribution of semblances for the same shot gather.

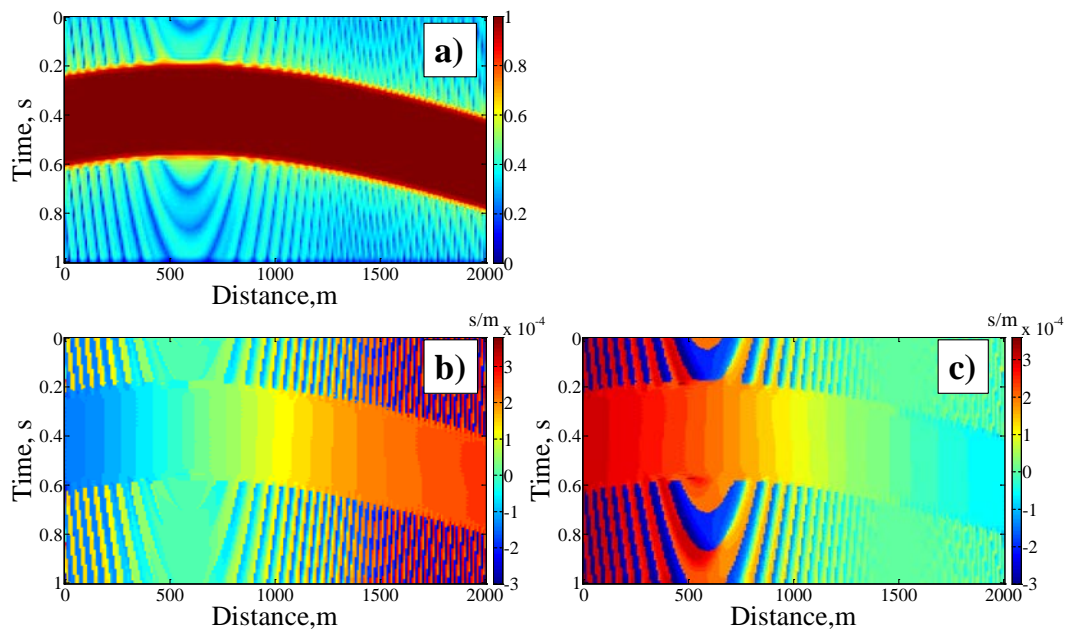


**Figure 5.4.** Horizontal slownesses for the model of a dipping interface. a) A semblances section for the shot gather at 1000 m, b) a section of  $p_r$  – values for the shot gather at 1000 m and c) a section of  $p_s$  – values for the shot gather at 1000 m.

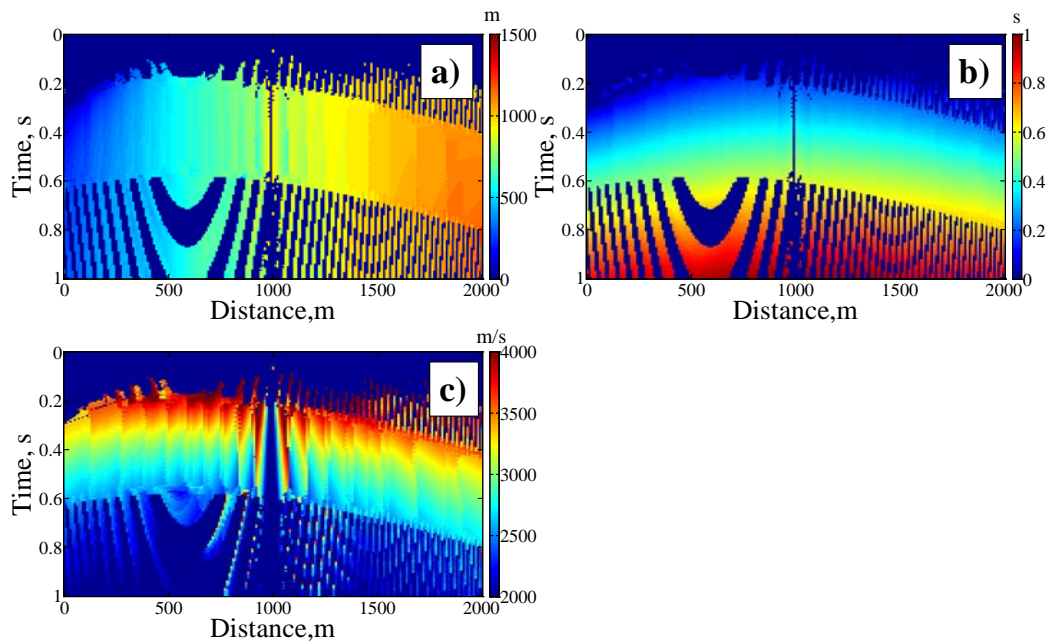


**Figure 5.5.** Migration attributes for the model of a dipping interface. a) A migrated  $x$  coordinate attribute for the shot gather at 1000 m, b) a migrated  $t_0$  attribute for the shot gather at 1000 m and c) a migrated velocity attribute for the shot gather at 1000 m.

An example of the computed migration attributes for the shot gather at 1000 m distance is shown in Figure 5.5. Figure 5.6a shows the migrated image of the dipping reflector, the slope and position of the interface are the same as on the true model section (Figure 5.3a). The velocity distribution obtained from the data is given in Figure 5.6b, only the velocities at locations to which more than 15 samples contribute from different input traces are plotted.

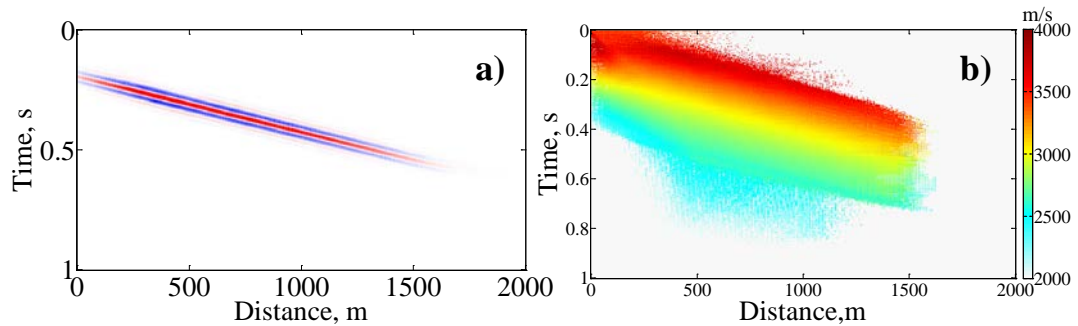


**Figure 5.6. Migration results of the convolution model of a dipping interface. a) Migrated image of an interface of noise-free data (25 m radius and 5 time samples window for slopes estimation). b) Velocity distribution along the dipping reflector (shown only velocities at locations to which more than 15 samples contribute from different input traces).**

In order to study the stability of the method in the presence of noise, random noise of 30% was added to the spike-traces before convolution with the wavelet, resulting in noisy data with the same frequency range as the noise-free data. An example of the seismogram containing a noise level of 30% is shown in Figure 5.7a. At first, the horizontal slownesses were estimated using the same parameter as for the noise-free data (a radius of 25 m that gave up to 21 traces to analyse in the spatial dimension and a 5 sample window in the temporal direction). An example of the distribution of semblance maxima, which is used for the local slopes computation, is shown in Figure 5.7b. The  $p_r$ - and  $p_s$ -values for a shot gather of noisy data are shown in Figure 5.7c and Figure 5.7d respectively. Figure 5.8 shows the calculated migration attributes: horizontal coordinate ( $x_m$ ), vertical travel-time ( $t_0$ ) and velocity ( $V$ ).

The migrated image of a dipping reflector of data with 30% noise level is shown in Figure 5.9a. The image from the noisy data is slightly blurred, but the dip and position of the boundary are recovered correctly. Figure 5.9b illustrates the velocity distribution along the dipping interface, only the velocities at locations to which more than 15 samples contribute from different input traces are shown.

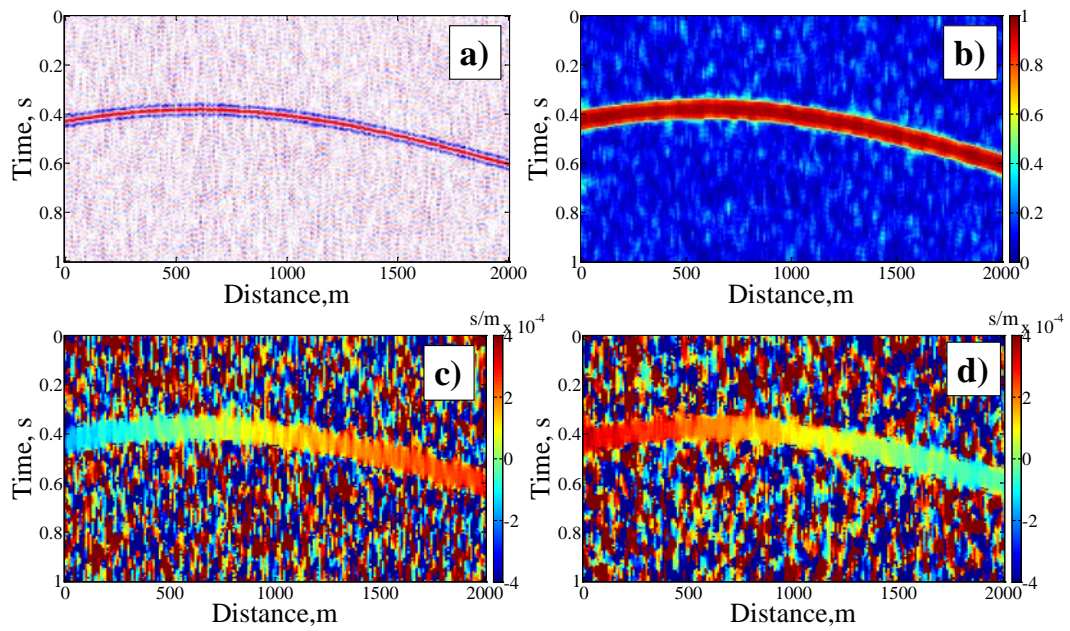


**Figure 5.7.** Convolution model of a dipping interface of data with 30% noise level. *a) Example of a shot gather at 1000 m, b) a semblances section for the shot gather at 1000 m, c) a section of  $p_r$  – values for the shot gather at 1000 m and d) a section of  $p_s$  – values for the shot gather at 1000 m. (25 m radius and 5 time samples window for slopes estimation).*

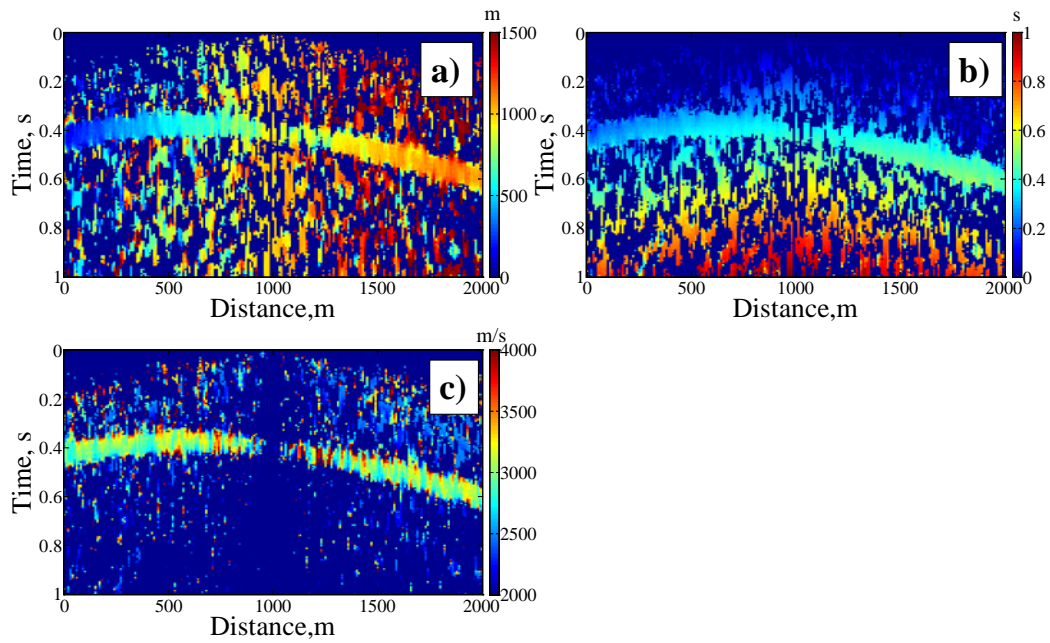


**Figure 5.8.** Migration attributes for the model of a dipping interface of data with 30% noise level (25 m radius and 5 time samples window for slopes estimation). a) Amigrated x coordinate attribute for the shot gather at 1000 m (Figure 5.3a), b) a migrated  $t_0$  attribute for the shot gather at 1000 m (Figure 5.3a), and c) a migrated velocity attribute for the shot gather at 1000 m (Figure 5.3a).

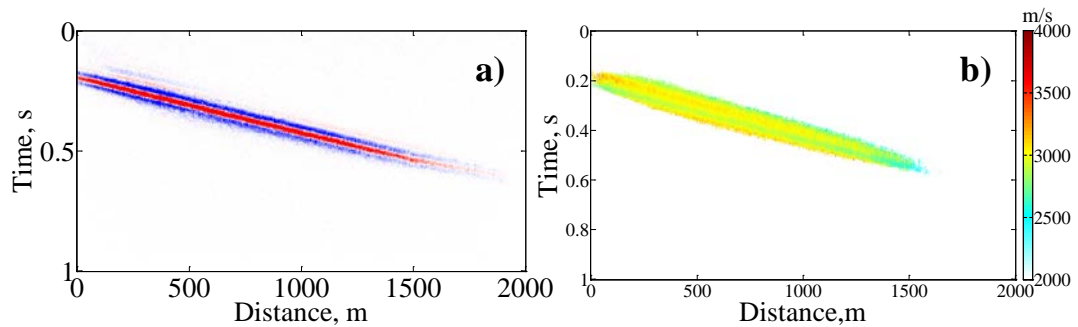


**Figure 5.9.** Migration results of the convolution model of a dipping interface of data with 30% noise level (25 m radius and 5 time samples window for slopes estimation). a) Migrated image of an interface of data with 30% noise level. b) Velocity distribution along the dipping reflector (shown only velocities at locations to which more than 15 samples contribute from different input traces).

To enhance the image quality and test migration parameters the spatial and temporal windows were increased. The radius was chosen to be 75 m (that gives up to 177

traces to analyse) and the time window enlarged up to 15 samples. The distribution of semblance maxima is displayed in Figure 5.10a. Figure 5.10b and 5.10c shows the results of computation of local slopes  $p_r$  and  $p_s$  from noisy data with expanded spatial and temporal estimation parameters. With larger windows, the distribution of horizontal slownesses appears much smoother (Figure 5.10b and 5.10c) as well as migration attributes in Figure 5.11. Figure 5.12a displays the migration result from noisy data with expanded spatial and temporal estimation parameters. The utilization of the larger windows allowed obtaining a clear image from the noisy seismograms. The lower part of the interface is not plotted on the final images in all cases, because there were no geophones in the presented geometry setup and therefore no reflection energy from that area. Figure 5.12b shows the velocity distribution along the dipping reflector (shown only velocities at locations to which more than 15 samples contribute from different input traces); a weighted average value is used in cases when multiple points contribute to the same location onto the velocity panel from different input traces. The velocity along the dipping interface corresponds to the true value of 3000 m/s.

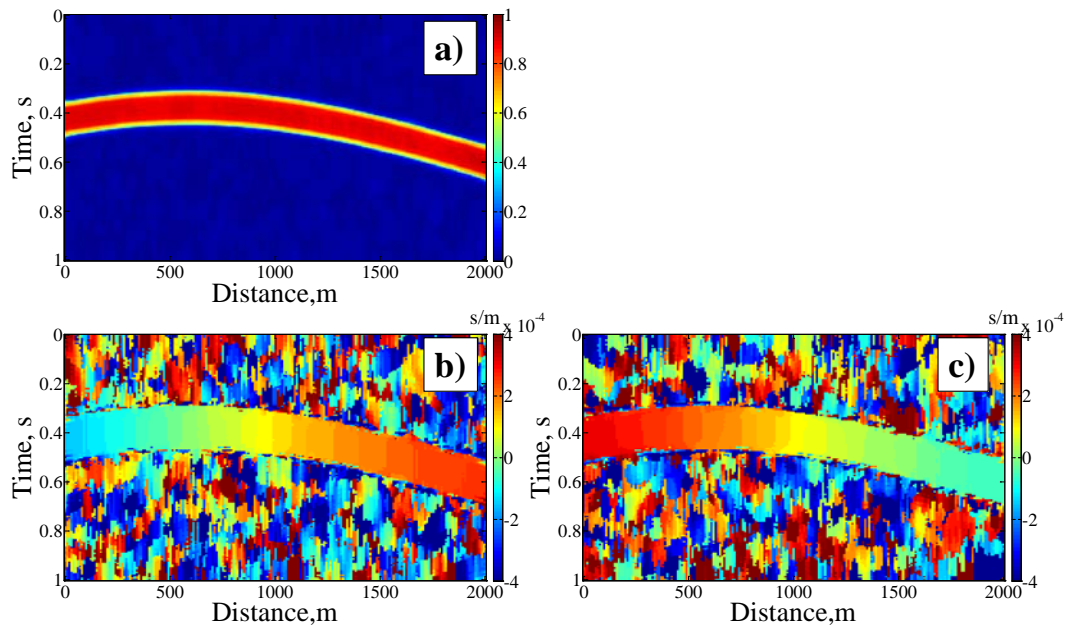


**Figure 5.10.** Horizontal slownesses for the model of a dipping interface of data with 30% noise level (75 m radius and 15 time samples window for slopes estimation). a) A semblances section for the shot gather at 1000 m, b) a section of  $p_r$  – values for the shot gather at 1000 m and c) a section of  $p_s$  – values for the shot gather at 1000 m.

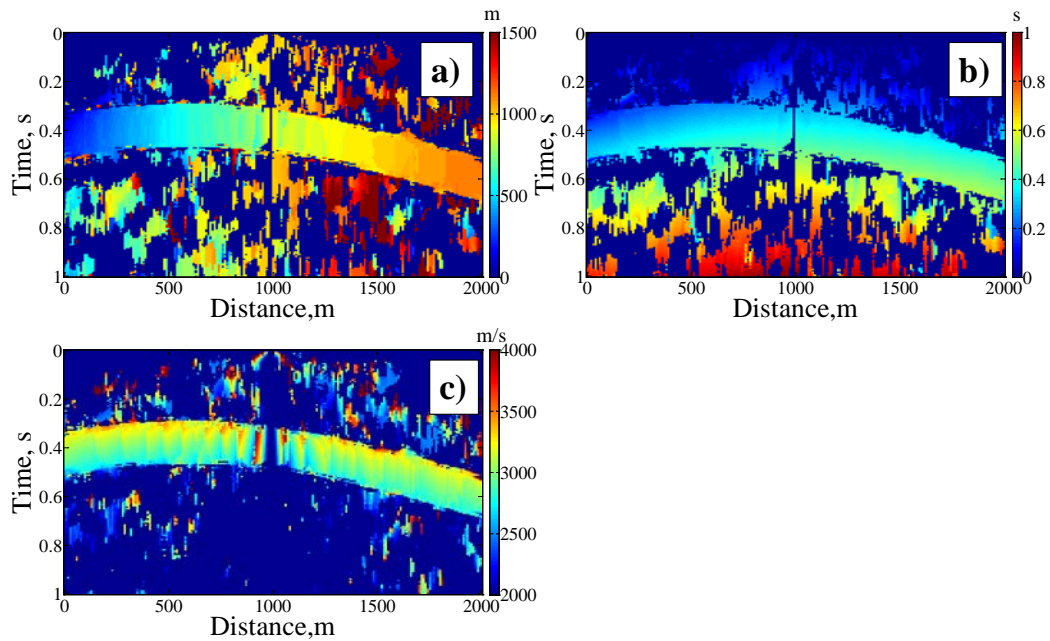


**Figure 5.11.** Migration attributes for the model of a dipping interface of data with 30% noise level (75 m radius and 15 time samples window for slopes estimation). a) A migrated  $x$  coordinate attribute for the shot gather at 1000 m (Figure 5.3a), b) a migrated  $t_0$  attribute for the shot gather at 1000 m (Figure 5.3a and. c) a migrated velocity attribute for the shot gather at 1000 m (Figure 5.3a).

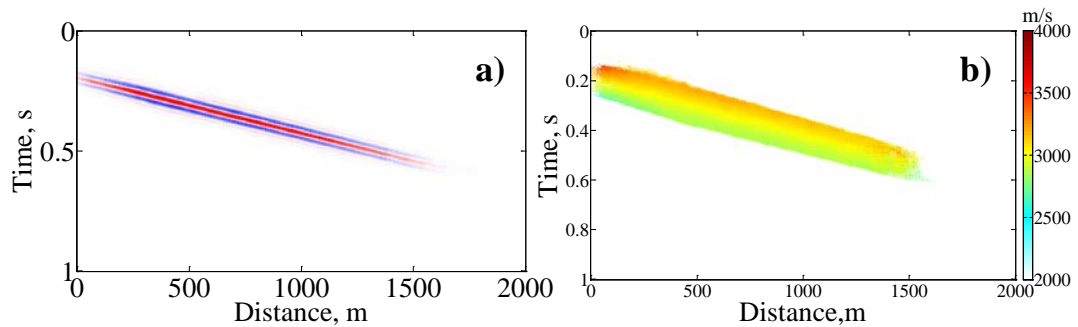


**Figure 5.12.** Migration results of the convolution model of a dipping interface of data with 30% noise level (75 m radius and 15 time samples window for slopes estimation). a) Migrated image of an interface of data with 30% noise level. b) Velocity distribution along the dipping reflector (shown only velocities at locations to which more than 15 samples contribute from different input traces).

The second basic model is a syncline. The same geometry setup was used to obtain the seismograms for the fold model. The velocity of the upper medium was 3000

m/s. The parameters of the wavelet and spike-traces were similar to those in the previous example. Two cases – without noise and 30% noise –were modelled. The actual position of the syncline in the time domain is shown in Figure 5.13a. An example of a shot gather at the location 1000 m is shown in Figure 5.13b. To extract the horizontal slownesses from the noise-free data, we applied the same parameters (25 m radius and a 5 sample time window), for the noisy data we also examined two setups similar to the previous model.

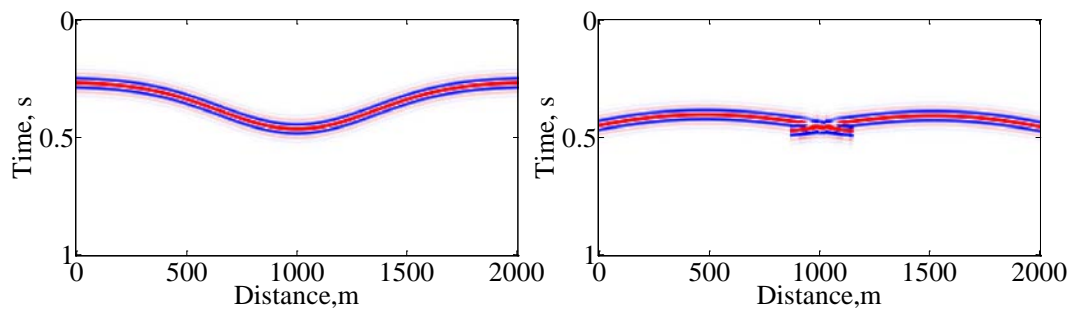


**Figure 5.13. Convolution model of a syncline. a) True position of a syncline in time scale and b) example of a shot gather at 1000 m.**

Figure 5.14b illustrates a semblance maxima distribution of a shot gather at 1000 m. The examples of local slopes estimation  $p_r$  and  $p_s$  are shown in Figure 5.14c and 5.14d respectively. The distribution of the migration attributes for the same shot gather is displayed in Figure 5.15. The migrated image of the syncline is shown in Figure 5.16a. The syncline shape is recovered completely, and it is correctly located. On the migrated images of the syncline, the amplitude distribution along an interface is uneven. This can be explained by the various amount of energy that is reflected from different parts of the model, not by errors in dip estimations. Figure 5.14a shows the distribution of the reflected energy from the spike syncline model (unit amplitude along the interface). The number of points coming from the input data to a certain location on the migrated image is shown. To produce this picture a unit amplitude model and true local slopes were used. The depth of the fold and the slopes of its sides match the actual model.

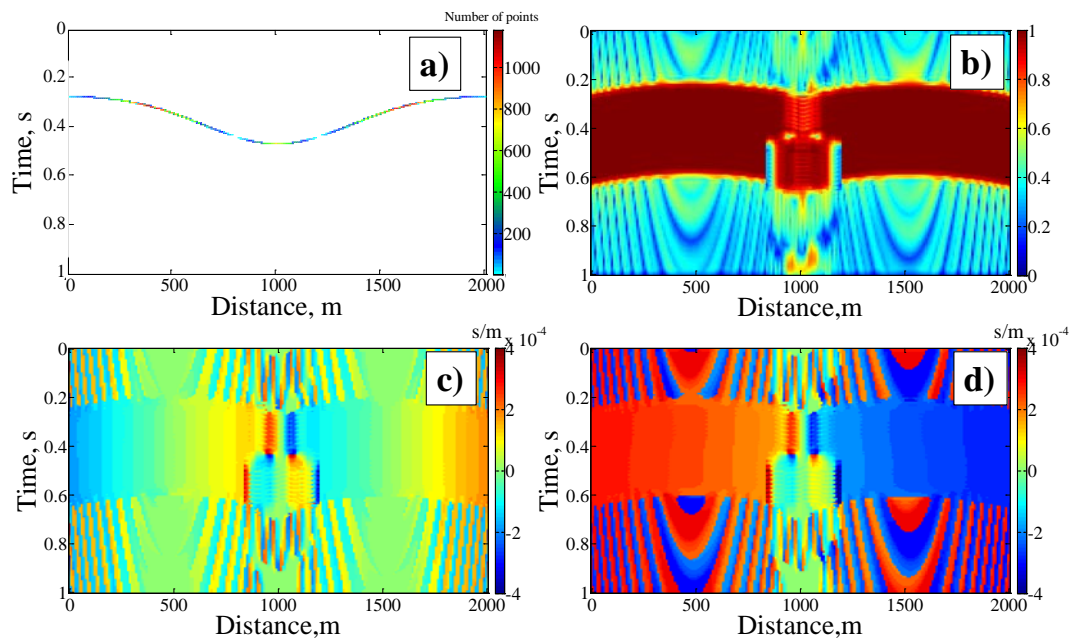


**Figure 5.14. Convolution model of a syncline. a) Energy distribution from the unit amplitude syncline model. Shown how many points are coming from the input data to a certain location on the image. True slopes were used for the migration, b) a semblance section for the shot gather at 1000 m, c) a section of  $p_r$  – values for the shot gather at 1000 m and d) a section of  $p_s$  – values for the shot gather at 1000 m.**

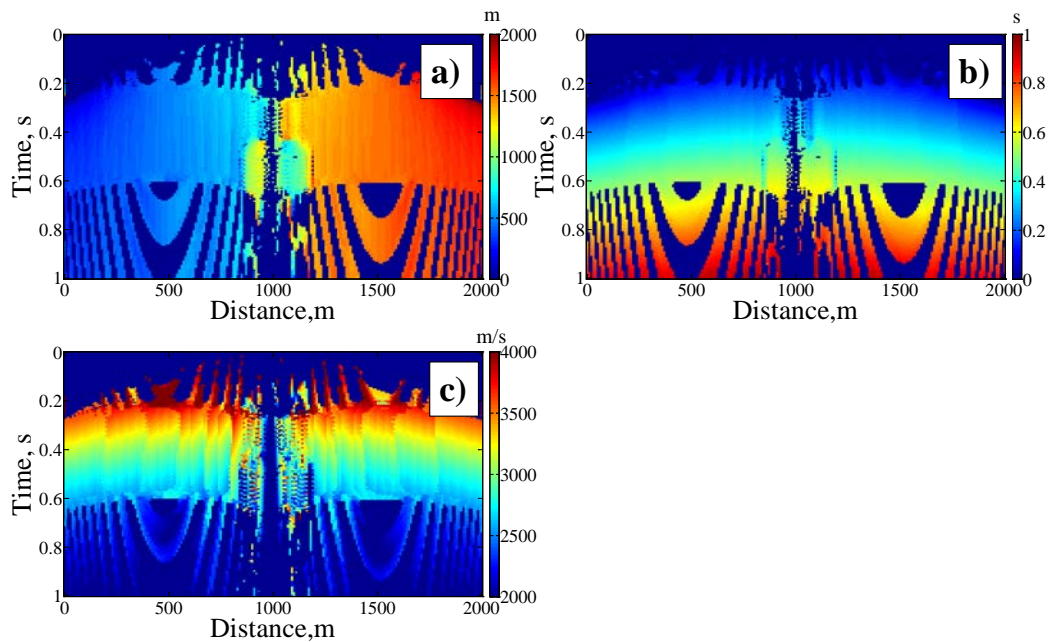


**Figure 5.15.** Migration attributes for the model of a syncline. a) A migrated  $x$  coordinate attribute for the shot gather at 1000 m, b) a migrated  $t_0$  attribute for the shot gather at 1000 m and c) a migrated velocity attribute for the shot gather at 1000 m.

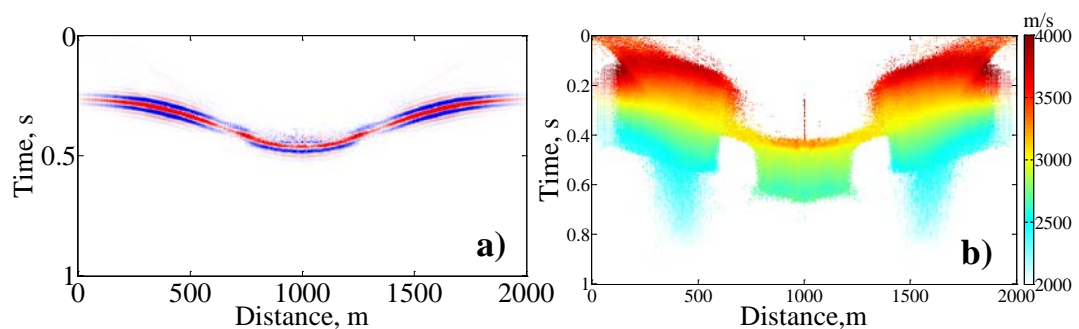


**Figure 5.16.** Migration results of the convolution model of a syncline. a) Migrated image of a syncline of noise-free data (25 m radius and 5 time samples window for slopes estimation). b) Velocity distribution along the syncline (shown only velocities at locations to which more than 15 samples contribute from different input traces).

The following modelled case is a syncline convolution model with the presence of noise. Random noise of 30% was added to the model; the same frequency band was

kept as for the noise-free data. The seismogram of the syncline model including a noise level of 30% is shown in Figure 5.17a. For the noisy data two setups of the local slope estimation, similar to the previous dip interface model, were also examined. At first, the horizontal slownesses were extracted with parameters: 25 m spatial radius and a 5 sample time window. Figure 5.17b displays an example of the semblance distribution for a shot gather at 1000 m. The obtained  $p_r$  and  $p_s$ -values for the same seismogram are shown in Figure 5.17c and Figure 5.17d respectively. The calculated migration attributes for a shot gather at 1000 m are given in Figure 5.18.

The migrated section of the fold of data with 30% noise level is shown in Figure 5.19a. The bottom of the syncline is blurred, but the location and shape of the fold are reconstructed accurately. Figure 5.19b shows the final velocity model as a distribution of values along the syncline surface (only the velocities at locations to which more than 15 samples contribute from different input traces are shown), the true velocity of 3000 m/s is recovered alongside the fold interface.

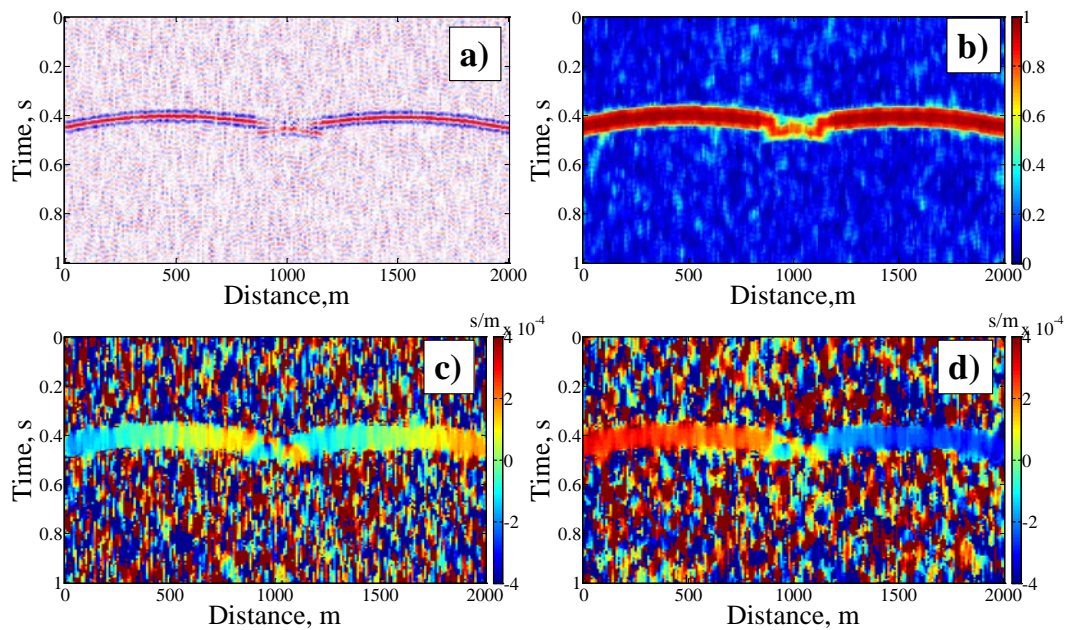


**Figure 5.17.** Convolution model of a syncline of data with 30% noise level. a) Example of a shot gather at 1000 m, b) a semblance section for the shot gather at 1000 m, c) a section of  $p_r$  – values for the shot gather at 1000 m and d) a section of  $p_s$  – values for the shot gather at 1000 m. (25 m radius and 5 time samples window for slopes estimation).

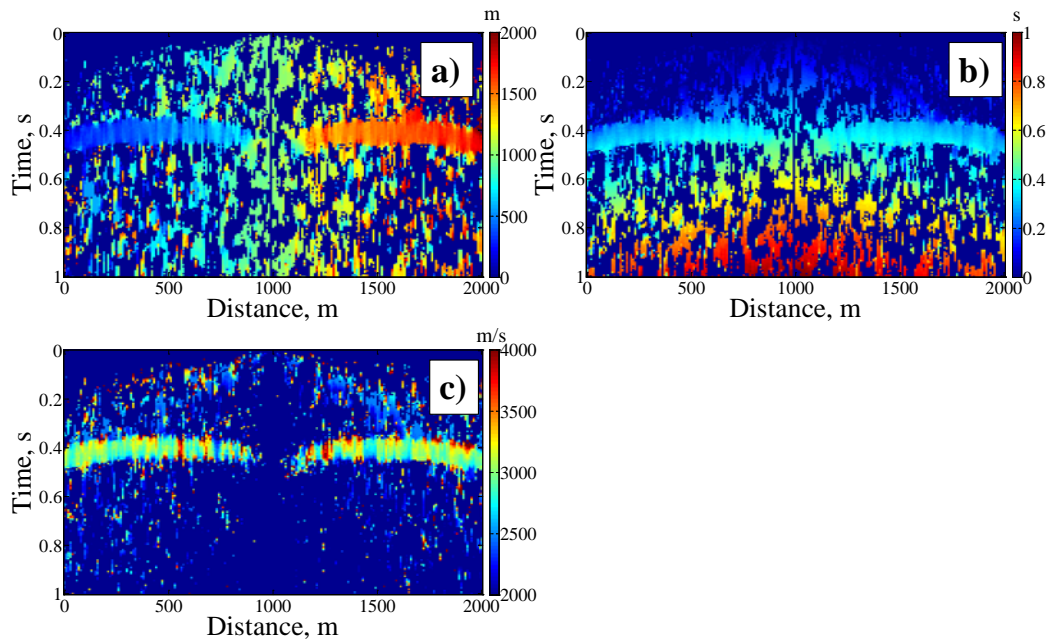


**Figure 5.18.** Migration attributes for the model of a syncline of data with 30% noise level (25 m radius and 5 time samples window for slopes estimation). a) A migrated x coordinate attribute for the shot gather at 1000 m (Figure 5.17a), b) a migrated  $t_0$  attribute for the shot gather at 1000 m (Figure 5.17a) and c) a migrated velocity attribute for the shot gather at 1000 m (Figure 5.17a).

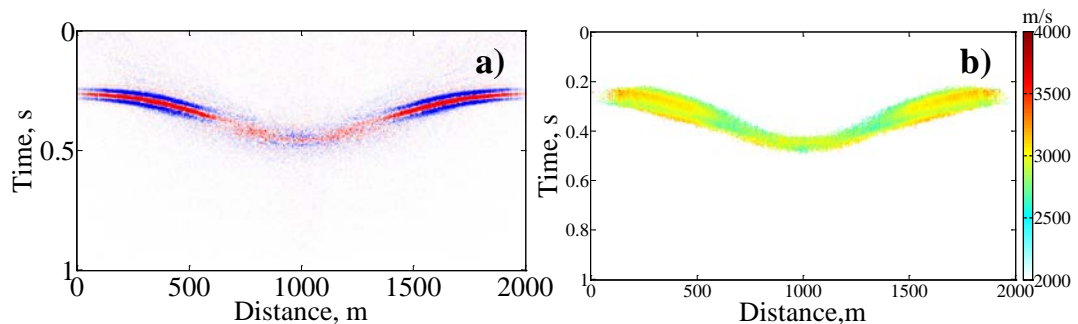


**Figure 5.19.** Migration results of the convolution model of a syncline of data with 30% noise level (25 m radius and 5 time samples window for slopes estimation). a) Migrated image of a fold of data with 30% noise level. b) Velocity distribution along the syncline (shown only velocities at locations to which more than 15 samples contribute from different input traces).

To help recovering the syncline shape completely the enlarged searching window was applied for an estimation of local slopes. The similar, to the dip interface noisy

data, setup – spatial radius 75 m (up to 177 traces to analyse) and temporal width of 15 samples – was used to improve the syncline migrated image. The smooth panels of examples of horizontal slownesses  $p_r$  and  $p_s$  for the shot gather at 1000 m are shown in Figure 5.20b and Figure 5.20c. Semblance distribution for the same seismogram is displayed in Figure 5.20a. The distribution of the migration attributes for the shot gather at 1000 m are shown in Figure 5.21; they appear more consistent along the syncline interface.

Figure 5.22a shows the migration result of the syncline of noisy data with expanded searching parameters for local slopes calculation. The fold is imaged completely, and it is correctly located. The velocity distribution obtained from the noisy data is shown in Figure 5.22b; displayed only the velocities at locations to which more than 15 samples contribute from different input traces.

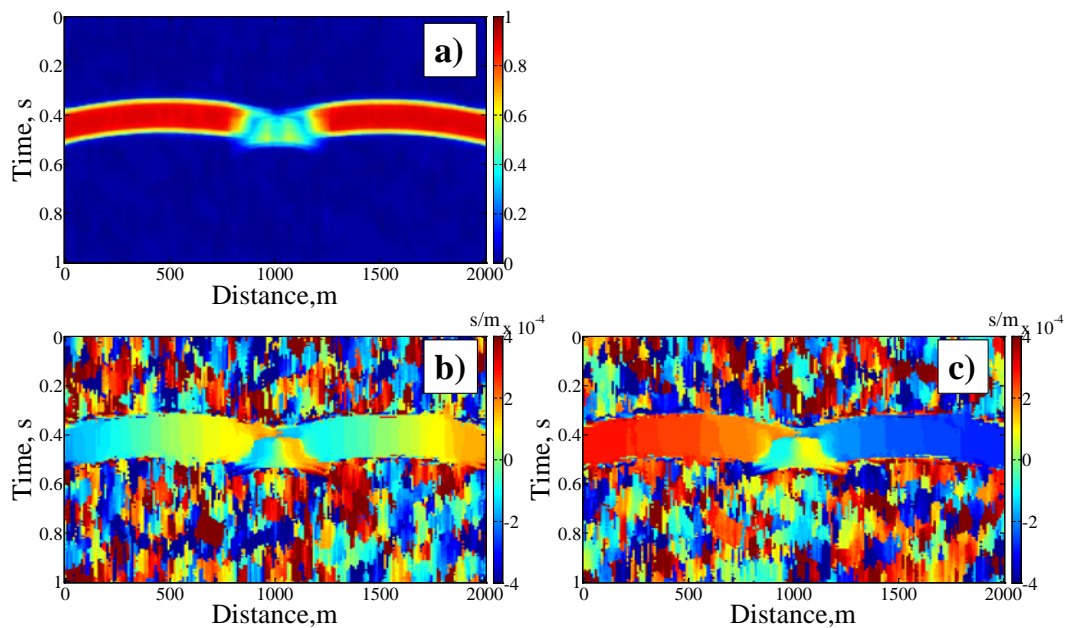


**Figure 5.20.** Horizontal slownesses for the model of a syncline of data with 30% noise level (75 m radius and 15 time samples window for slopes estimation). a) A semblance section for the shot gather at 1000 m (Figure 5.17a), b) a section of  $p_r$  – values for the shot gather at 1000 m (Figure 5.17a) and c) a section of  $p_s$  – values for the shot gather at 1000 m (Figure 5.17a).

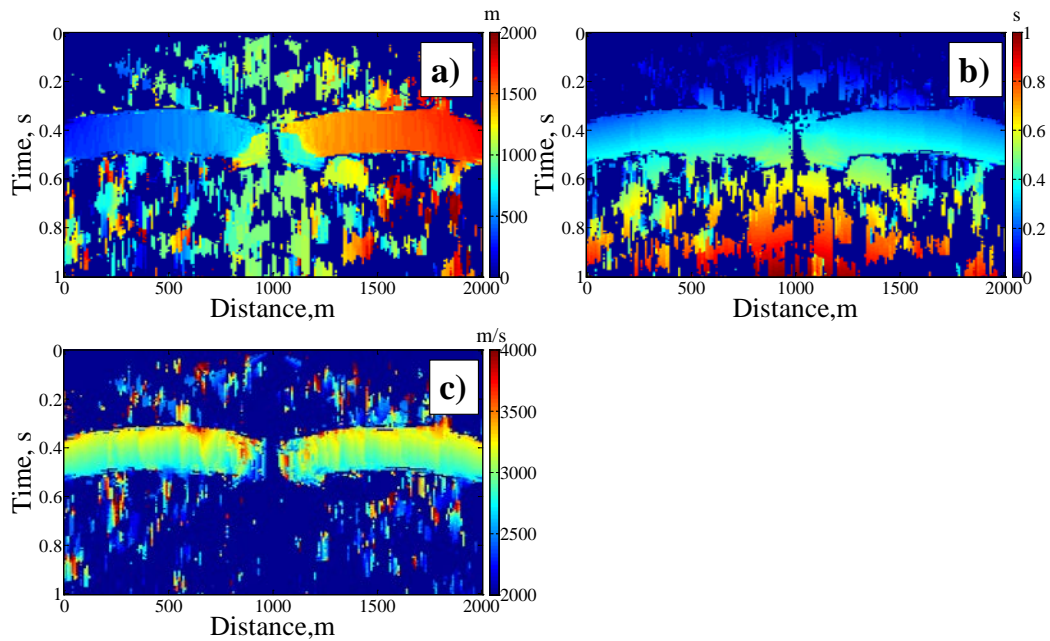


**Figure 5.21.** Migration attributes for the model of a syncline of data with 30% noise level (75 m radius and 15 time samples window for slopes estimation). a) A migrated x coordinate attribute for the shot gather at 1000 m (Figure 5.17a), b) a migrated  $t_0$  attribute for the shot gather at 1000 m (Figure 5.17a) and c) a migrated velocity attribute for the shot gather at 1000 m (Figure 5.17a).

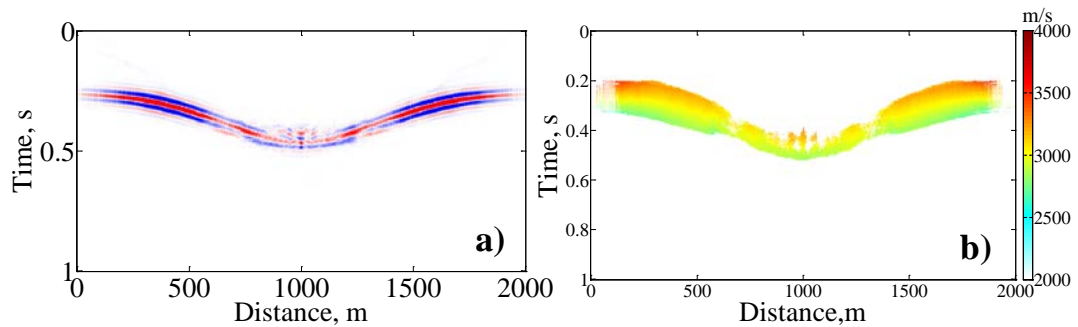


**Figure 5.22.** Migration results of the convolution model of a syncline of data with 30% noise level (75 m radius and 15 time samples window for slopes estimation). a) Migrated image of a fold of data with 30% noise level. b) Velocity distribution along the syncline (shown only velocities at locations to which more than 15 samples contribute from different input traces).

The results of the migration for both basic models are sufficiently promising for seismic applications. Both interfaces, the dipping reflector and syncline, were

reconstructed correctly. The presented examples reveal that the imaging algorithm is able to handle data in the presence of high levels of random noise. The seismic wavelength, source-receiver geometry and signal to noise ratio should be considered when selecting the spatial and temporal width of slopes estimation window. The slope dependant summation and tuning the searching parameters for slownesses estimation can significantly improve the quality of the final image. The accuracy of estimation of the local event slopes, and as a result, the quality of the final image, depends on the quality and coherency of the input data.

### **5.2.1. Errors in Slopes Estimation**

Computation of horizontal slownesses is a crucial step of the presented imaging algorithm. The computation of horizontal slownesses has been implemented in MatLab code using the semblances analysis (Neidell and Taner, 1971). This approach produces the most adequate and robust determination of local slope's values.

In order to show how errors of slownesses estimation influence the final result, the syncline model (similar to the second example of basic models) with unit amplitudes was taken for study. The true local slopes were considered in the analysis. Using real values of slownesses the migration attributes were computed and the migrated image of the fold shape was reconstructed. Figure 5.23a shows the migrated fold; colours refer to the amount of energy that has been summed back to a certain location of the syncline interface from the unit inputs. Then the trough was rebuilt from the over- and underestimated  $p_r$  and  $p_s$  values. Figure 5.23b displays the final image of the syncline when 10 per cent overestimated slownesses values were taken for attributes computation; Figure 5.23c illustrates the fold's shape from the case of 10 per cent underestimated local slope's values as an input to migration process. It can be seen, that images are getting blurred, because the reflection energy distributes (mostly scatters above the trough when slopes are getting bigger than true values and below in the opposite example) at the migrated panel around the interface location rather than along it. The case with random distribution of 10 per cent errors in horizontal slownesses values was introduced as well and the result of syncline reconstruction is

shown in Figure 5.23d. In this example the amplitudes are more or less evenly spread out around the fold boundary.

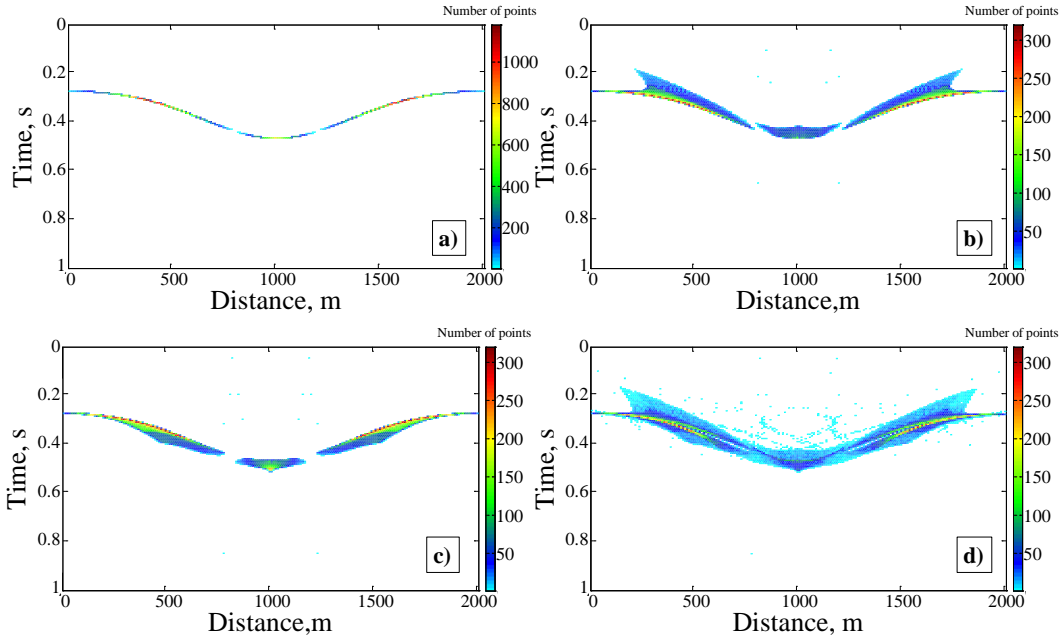


**Figure 5.23. Migrated sections of the syncline model with unit amplitudes. Colours show the energy distribution from the unit amplitude syncline model. Shown how many points are coming from the input data to a certain location on the image. a) Image from true values of local slopes for migration. b) Image from 10% overestimated values of local slopes for migration. c) Image from 10% underestimated values of local slopes for migration. d) Image from random distribution of 10% errors in values of local slopes for migration.**

These examples show that the quality of final migrated images is strongly dependent on the accuracy of estimation of local event slopes. The algorithm has several parameters, which can be tuned to obtain the most reasonable outcome. One of them is a range of horizontal slownesses, which has to be defined prior to the estimation process. Limits of this interval have to cover the possible velocity range; the increment of the searching interval has to be small enough to provide accurate slope estimation and has not to be too fine to overly slow down the computational process. The second parameter is a size of a running window (radius and number of time samples) for slopes calculation. As has been shown in the previous chapter, this setup is able to improve the final image quality in the presence of random noise. All

parameters have to be tested on a part of seismic data before launching the migration process for a whole dataset.

### ***5.3. Synthetic Dataset Based on Realistic Geological Model***

The presented prestack time migration was applied to a model that simulates real geological conditions. The synthetic data were generated by a finite-difference method using TesseralCS-2D modelling software. This model is based on the geology of the Sunrise Dam – Cleo gold deposit in Western Australia (Brown et al., 2002). The Sunrise Dam operation is about 55 km south of Laverton, 220 km NNE of Kalgoorlie, and 770 km NE of Perth, in the Eastern Goldfields province of the Yilgarn Craton. The constructed model is shown in Figure 5.24. The host rocks are represented by volcanoclastic formations overlain by a variable depth slow velocity regolith. The model has shallow to steep dipping shear zones, mafic and felsic intrusions, interbedded dolerite, and Banded Iron Formations (BIFs). The main gold mineralization is confined to shear zones and to high grade discrete quartz carbonate narrow veins. There are spatial correlations between felsic porphyry dikes and gold mineralization lodes. The porphyry dikes and their margins preferentially control the location of these zones, and they are parallel to the porphyry dike. Ore zones are best developed within BIFs and are characterized by pyrite replacement of magnetite-rich layers (Brown et al., 2002).

Hard rock seismic exploration in Western Australia is still not widespread and there is a limited knowledge of seismic and sonic velocities in the area. P-wave velocities (Table 1) were approximated from root-mean-square (RMS) stacking velocities used in the reprocessing of the Anglo Gold Ashanti regional seismic line which passed over part of the Sunrise Dam deposit (Urosevic and Evans, 2007). In some cases velocities and densities were obtained from the literature (Telford et al., 1990) or selected from a TesseralCS-2D parameter menu for corresponding rock types. This menu has a library of minimum, average and maximum elastic parameters for common sedimentary, metamorphic and igneous rock types. The values of the velocity and density for every unit are represented in Table 1.

A total number of 181 receiver locations along the surface was used, the distance between the receivers was 5 m; shots were located at the same positions as the receivers. A Ricker wavelet with a central frequency of 80 Hz was chosen as the source signal. Acoustic full-waveform modelling was used to obtain synthetic seismograms. The sampling rate was 0.5 ms and the record length was 1 second. To compare the actual locations of the geological features and the targets of the model with the final results of the time migration, the velocity model was converted to time domain, as shown in Figure 5.25. The (RMS) velocities of the hard rock model were computed from the depth velocity distribution and are shown in Figure 5.26.

#	Rock Unit	Vp m/s	Density (kg/m <sup>3</sup> )
A	Regolith	2200	2000
B	Volcaniclastic	5500	2800
C	Mafic intrusion	6200	3500
D	Banded Iron Formation	6200	2750
E	Dolerite	6400	2900
F	Felsic Porphyry	6700	3100
G	Fault	5800	2650
H	Shear Zone	5000	2600

*Table 1. Velocity-Density table for the 2D geology model.*

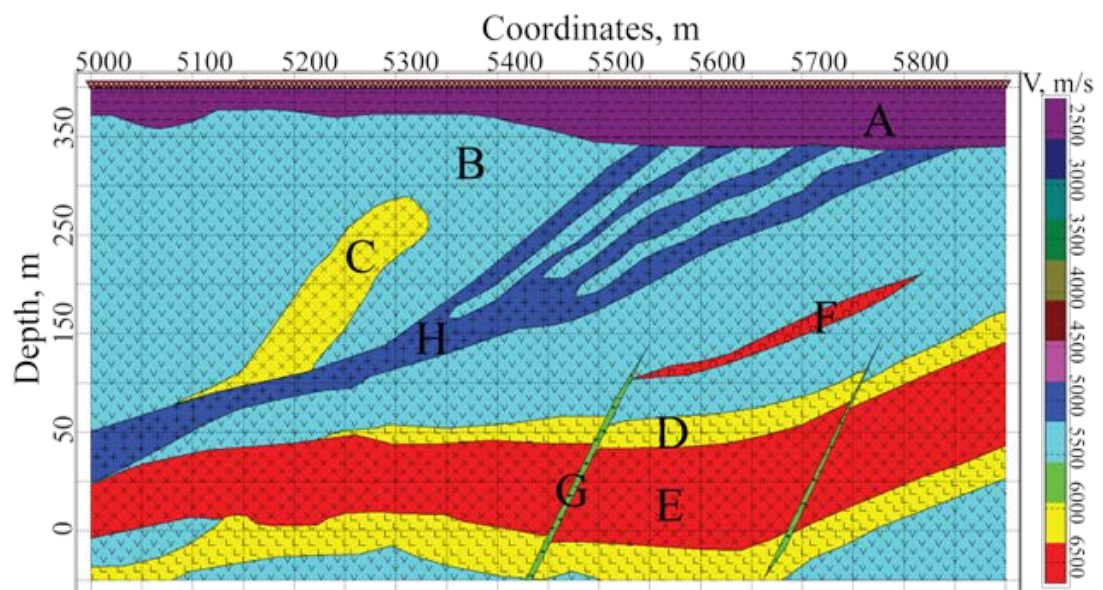


*Figure 5.24. 2D hard rock velocity model, which was used to generate a synthetic seismic dataset. (rock type letters are defined in Table 1)*

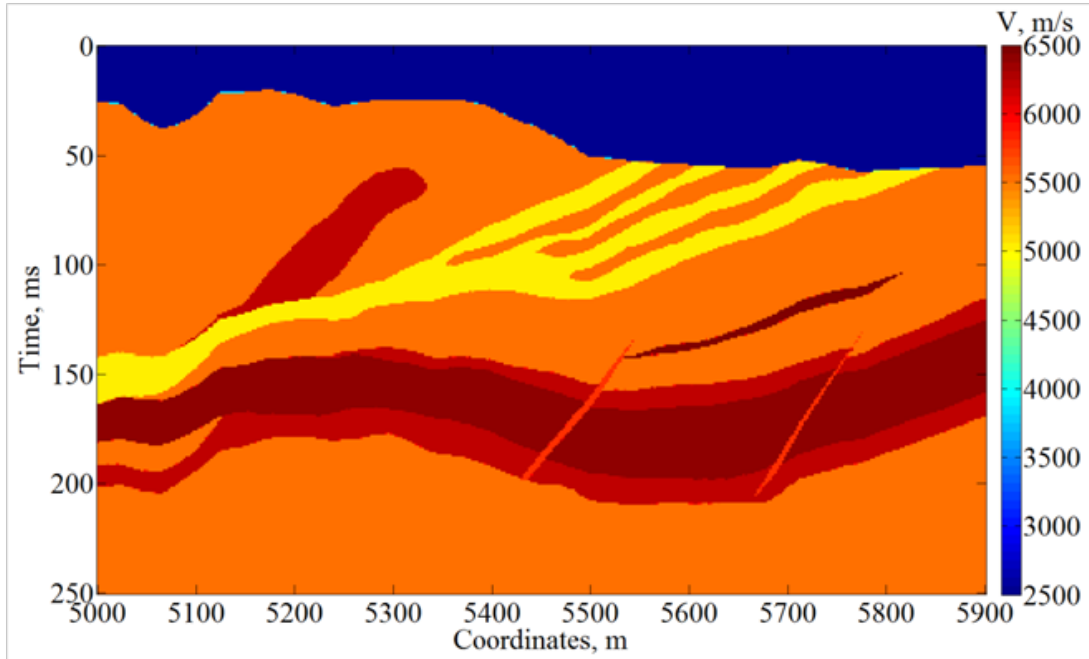


**Figure 5.25.** 2D hard rock velocity model converted to time domain.

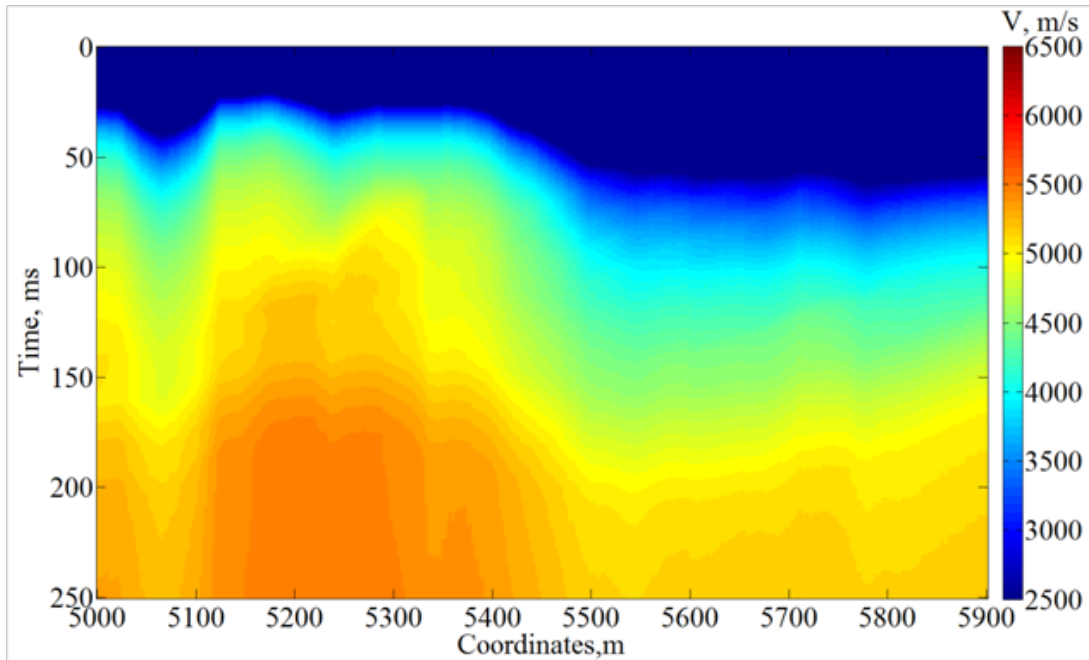


**Figure 5.26.** 2D section of the RMS velocities.

To compute the values of local event slopes, the imaging algorithm has been launched with the following setup: a spatial radius of 25 m was selected (giving up to 81 traces to analyse); a time window of 5 samples was taken for the temporal size of

a running window. An example of semblances for the shot gather at 5500 m, which are used for identification of a correct slope, is shown in Figure 5.27a. The estimated distribution of horizontal slownesses for the same gather is displayed in Figure 5.27b and Figure 5.27c. The migrated attributes (coordinate of the reflection point, vertical travel time and velocity) for the referred shot gather is shown in Figure 5.28.

No pre-processing was applied to the synthetic seismograms prior to the imaging step using the migration algorithm. The velocity analysis and mapping of the amplitudes to the final image are part of the same process. This allows avoiding manually processing the velocity model estimation and makes the migration automated. Figure 5.29 shows the smoothed section of migration velocities obtained by the algorithm; in the case when multiple points contribute to the same location from different input traces, a weighted average is used in the final velocity model; the range of migration velocities corresponds to the actual velocity distribution (Figure 5.25).

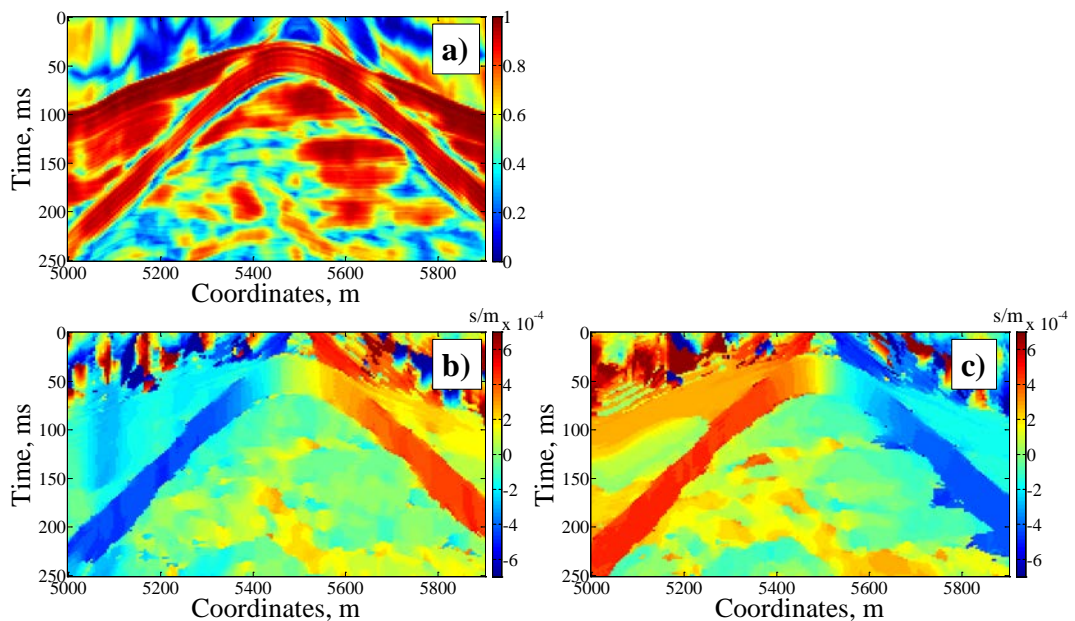


**Figure 5.27. 2D synthetic geological model. Shot gather at 5500 m. a) A semblance section, b) a section of  $p_r$  - values and c) a section of  $p_s$  - values.**

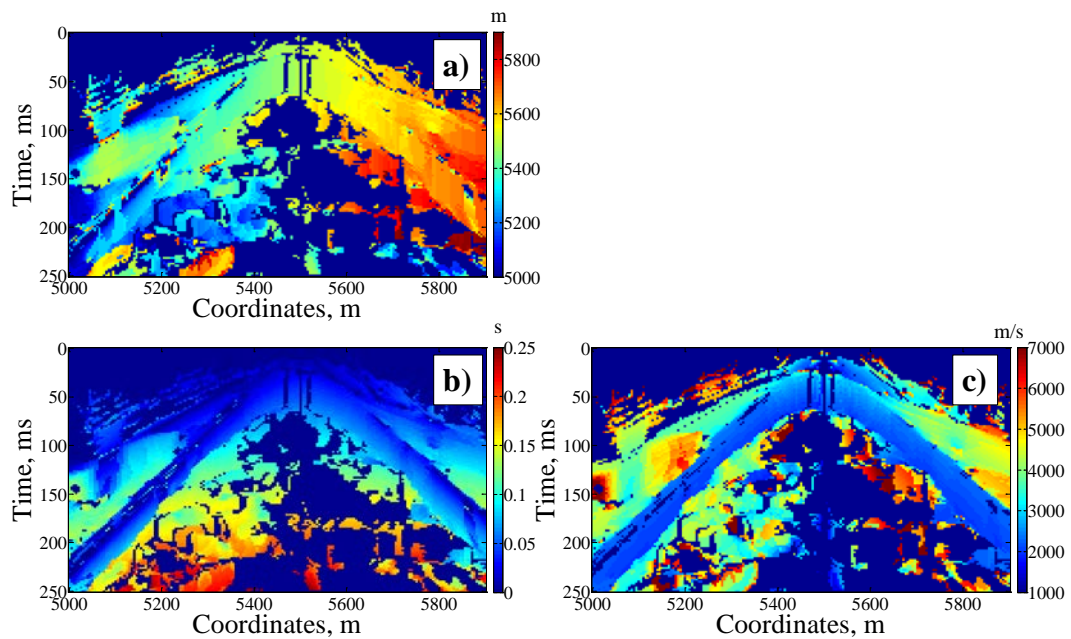


**Figure 5.28. 2D synthetic geological model. Shot gather at 5000 m. a) A migrated  $x$  coordinate attribute, b) a migrated  $t_0$  attribute and c) a migrated velocity attribute.**

The final migrated section of the 2D geological synthetic model is presented in Figure 5.30. The amplitudes of the dataset were collected and summed into the image according to the corresponding values of the attributes: vertical travel-time and horizontal reflection point location. Figure 5.31 illustrates the migrated image overlaid on the true velocity model. The interface between regolith and volcanoclastic rocks is displayed clearly. The top of the mafic intrusion can be distinguished easily; the steep sides of this intrusion are not visible, because most of the reflected energy is not recorded by the receivers. The whole felsic porphyry body is distinctly observed. The shear zones can also be traced on the migrated section. We can see that all the main geological targets, which are correlated with the gold mineralization zones (the felsic dyke and shear zones), can be clearly identified on the final image.

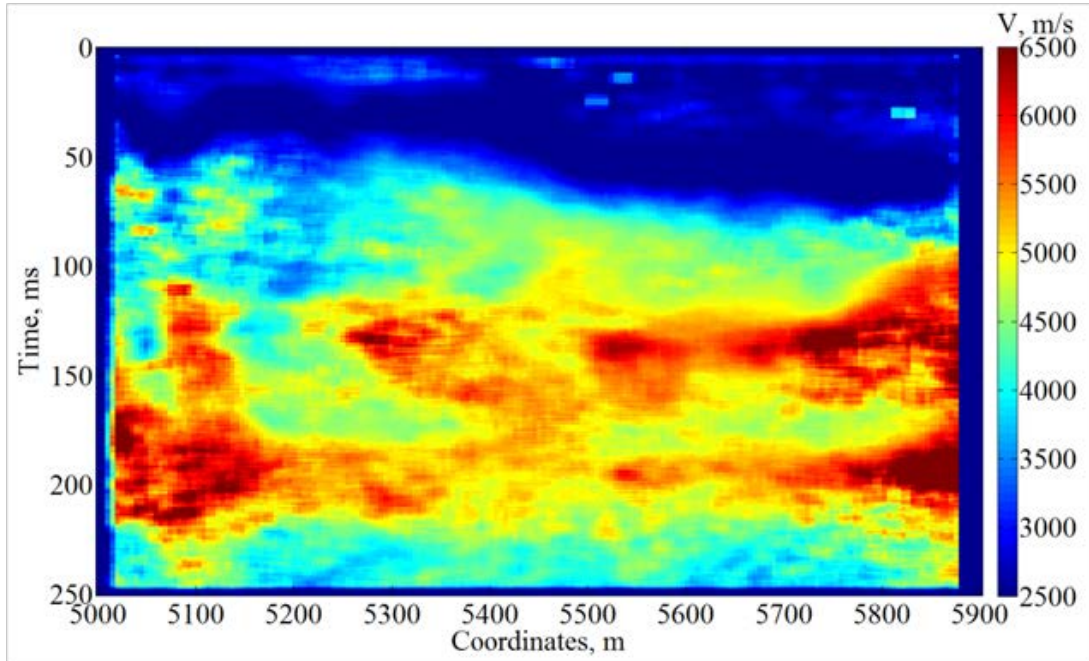


*Figure 5.29. Section of the migration velocities.*

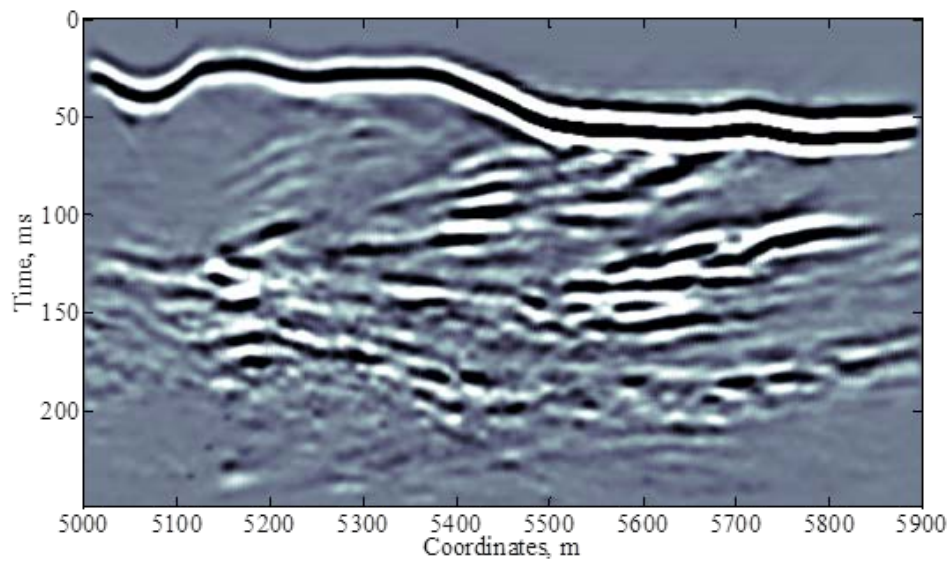


*Figure 5.30. The final image of the prestack time migration from the 2D hard rock geology model.*

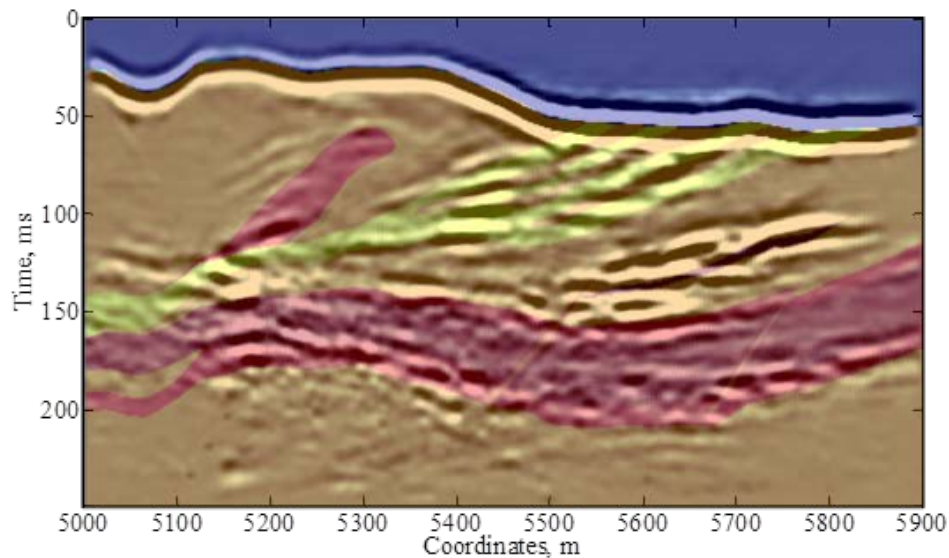


*Figure 5.31. The prestack migration image from the 2D hard rock geology model. Actual velocity model is overlaid onto the migrated section.*

### **5.3.1. Comparison with Kirchhoff Prestack Time Migration**

The next step of the study was to compare the result of the presented prestack time migration algorithm with a conventional Kirchhoff prestack time migration (PSTM). The migration velocities, which were obtained during the presented imaging process, were used as an input velocity model for the Kirchhoff PSTM. The final stack section of the PSTM is shown in Figure 5.32. The comparison of the Kirchhoff migration result with the actual model is presented in Figure 5.33. Both final migration images (Figure 5.30 and Figure 5.32) are comparable in terms of showing the main features and structures of the geological section. The Kirchhoff migrated image appears to be more continuous in several locations; the top of the banded iron formation is better pronounced on the PSTM section. These results demonstrate that the final migrated section from the presented algorithm is of reasonable quality and that this approach can be used in a hard rock seismic processing workflow as an automatic tool to obtain an input velocity model for the Kirchhoff PSTM.

In order to compare with a standard workflow, conventional processing of the synthetic data to obtain the stacking velocities was performed. The velocity analysis

was done after applying DMO corrections in Promax processing software; a section of the obtained stacking velocities is shown in Figure 5.34.

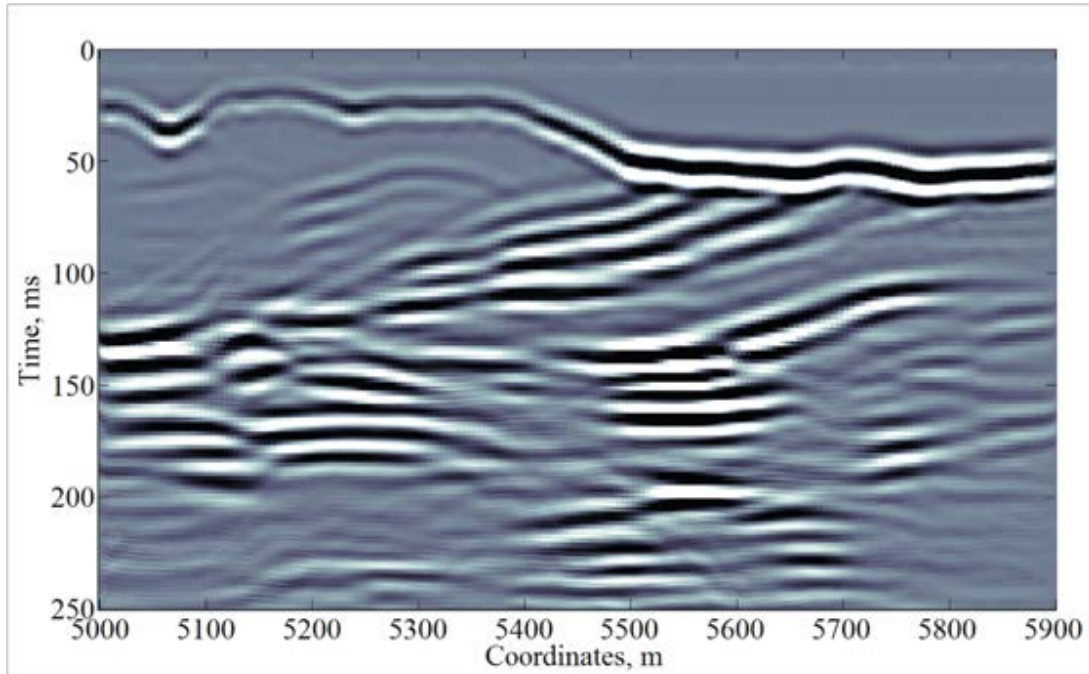


*Figure 5.32. Kirchhoff PSTM image from the 2D hard rock synthetic model. Migration velocities from the presented migration were used as an input velocity model.*

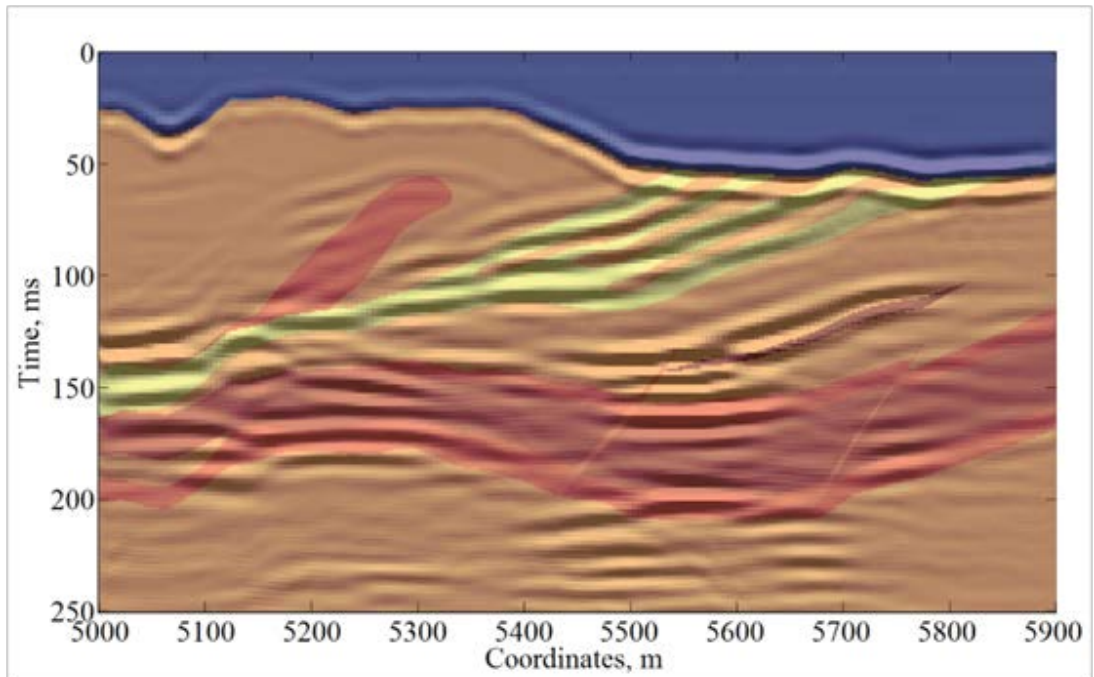


*Figure 5.33. Kirchhoff PSTM image from the 2D hard rock synthetic model. Migration velocities from the presented migration were used as an input velocity model. Actual velocity model is overlaid onto the migrated section.*

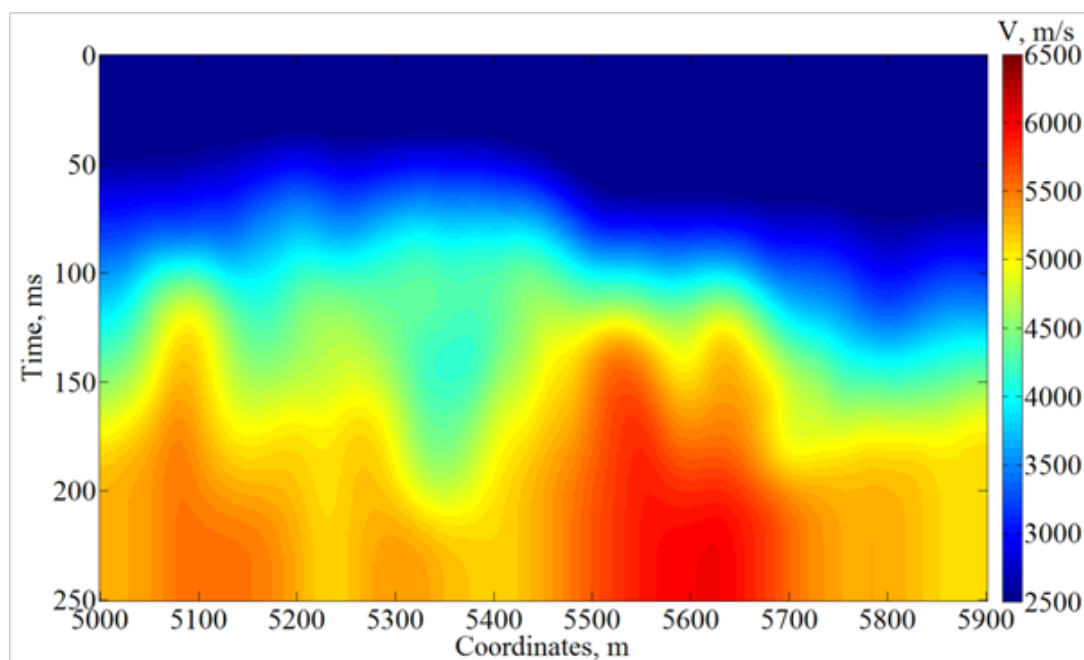


**Figure 5.34.** 2D stacking velocity model, which was obtained from a velocity analysis after applying DMO corrections.

The stacking velocity model was then used as an input model for the Kirchhoff PSTM; the result of that migration is shown in Figure 5.35. Comparing Figure 5.35 with Figure 5.32 shows that the results of both Kirchhoff migration sections are almost identical. Figure 5.36 shows an overlap of the PSTM image and the actual model. The migrated section with the stacking velocities clearly indicates the interfaces and features of the geological model. The main outcome of this study is that the migration velocities resulting from the proposed imaging process can be successfully used as an input velocity model for conventional migration techniques. The initial velocity analysis routine can be excluded from the processing flow. Such a modified workflow should be useful for hard rock seismic exploration, because in these environments the velocity spectra are usually incoherent and it is difficult to obtain an appropriate velocity model.

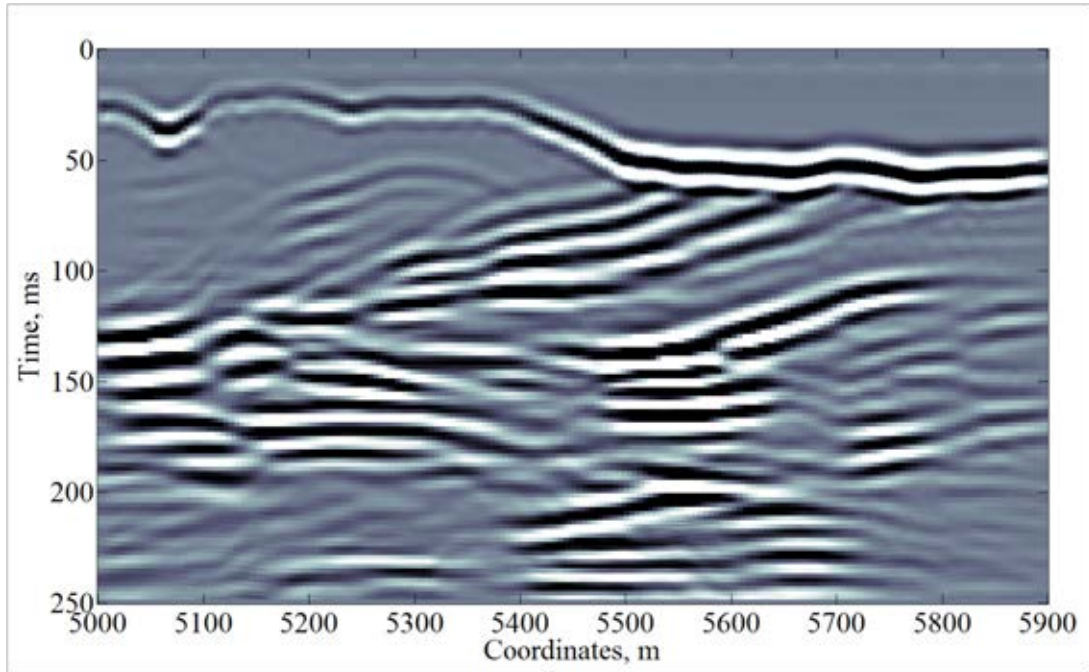


*Figure 5.35. Kirchhoff PSTM image from the 2D hard rock synthetic model. Stacking velocities from the velocity analysis were used as an input velocity model.*

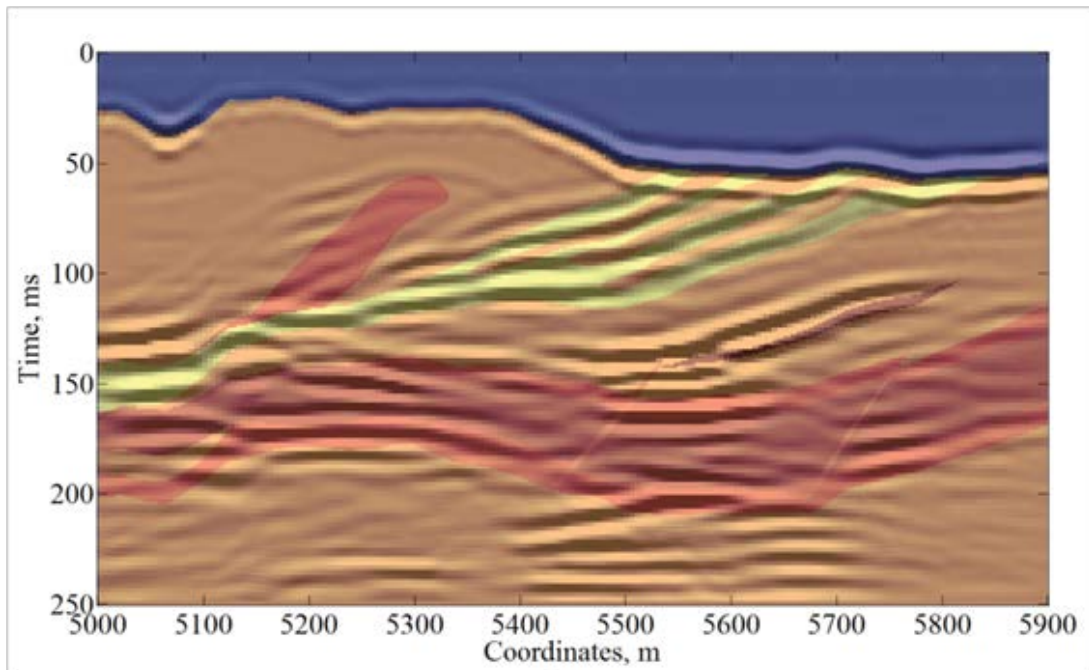


*Figure 5.36. Kirchhoff PSTM image from the 2D hard rock synthetic model. Stacking velocities from the velocity analysis were used as an input velocity model. Actual velocity model is overlaid onto the migrated section.*

The presented prestack time migration has been tested on several synthetic examples to assess the potential of applying this imaging technique to hard rock seismic exploration. The presented algorithm estimates the local slopes in common-shot and common-receiver domains using an assumption of hyperbolic offset-traveltime curves (Cooke et al., 2009). This assumes hyperbolic reflection responses; a deviation from this assumption could cause errors in the estimation of migration attributes. The horizontal slownesses contain comprehensive information about the geometry of reflections. These local event slopes allow calculating migration velocities, vertical travel-time and horizontal coordinates of the migrated locations for every input sample of the prestack data and directly mapping the events into the time-migrated image. The accuracy of the final migrated images strongly depends on the quality of estimation of the horizontal slownesses. Among the several possible approaches, the semblance approach has been chosen to obtain the local slopes, as it provides the most stable and robust results. Nevertheless, as was shown on the convolution examples, the accuracy of this estimation largely depends on the coherency and quality of the input data, but can be enhanced by an appropriate choice of searching parameters. The summation along the obtained local slopes, which has been included into implementation, has improved the quality of the final images.

Computationally, this imaging technique is relatively fast. The most time consuming part is the estimation of the local slopes of the seismic events, which is dependent on the used method. Mapping the seismic events from the input data to the migrated section goes in parallel with attributes calculation and amplitude–phase corrections; this procedure is almost instantaneous in comparison with slope estimation. Also, this migration avoids the manual velocity analysis process. Moreover there is a possibility of progressively building the velocity field and migration image in real time, particularly for certain 2D seismic geometry setups. The application of velocity-independent migration algorithms is especially important to hard rock seismic exploration in areas with high velocity and complex structures.

#### ***5.4. 2D Field Data Example – St Ives Mine Site***

The field data application was tested on a 2D seismic line. The seismic data were acquired at the St Ives goldfield. The St Ives district is located near Kambalda, 60 km south of Kalgoorlie in the Eastern Goldfields Province of the Yilgarn Craton in Western Australia. The considered seismic 2D profile SI-NJ1 (North Junction) is highlighted as a red line in Figure 5.37. The seismic line was part of a high-resolution seismic test program for Gold Fields Limited and Placer-Dome Asia Pacific in 2002 – 2004. The survey area is placed on the southern tip of the Norsemen-Wiluna greenstone belt of the Yilgarn Craton.

The Yilgarn Craton is an Archaean greenstone sequence formed of basalts, ultramafics and interflow sediments. These formations are found mainly in a regional-scale north–northwest extended Kambalda Anticline, which is immersing to the south direction. Gold mineralization in the St Ives complex is associated commonly with shear zones and faults, which are provided migration paths for hydrothermal fluids. The major regional structure is the 200-km-long Boulder-Lefroy shear zone (Torey, 1970; Weinberg et al., 2004). The local structures, such as the Playa shear zone, are also abundant sources of gold and nickel mineralization. Gold usually appears within thrust/shears but also is associated with stock-works, vein arrays, and in breccia zones. Gold occurrences are also often revealed near intermediate and felsic porphyry dykes (Drummond et al., 2000; Li, 2009; Moss and Scott, 2001; Vearncombe, 1998). In such a complex environment structural and lithological knowledge is crucial for gold exploration.

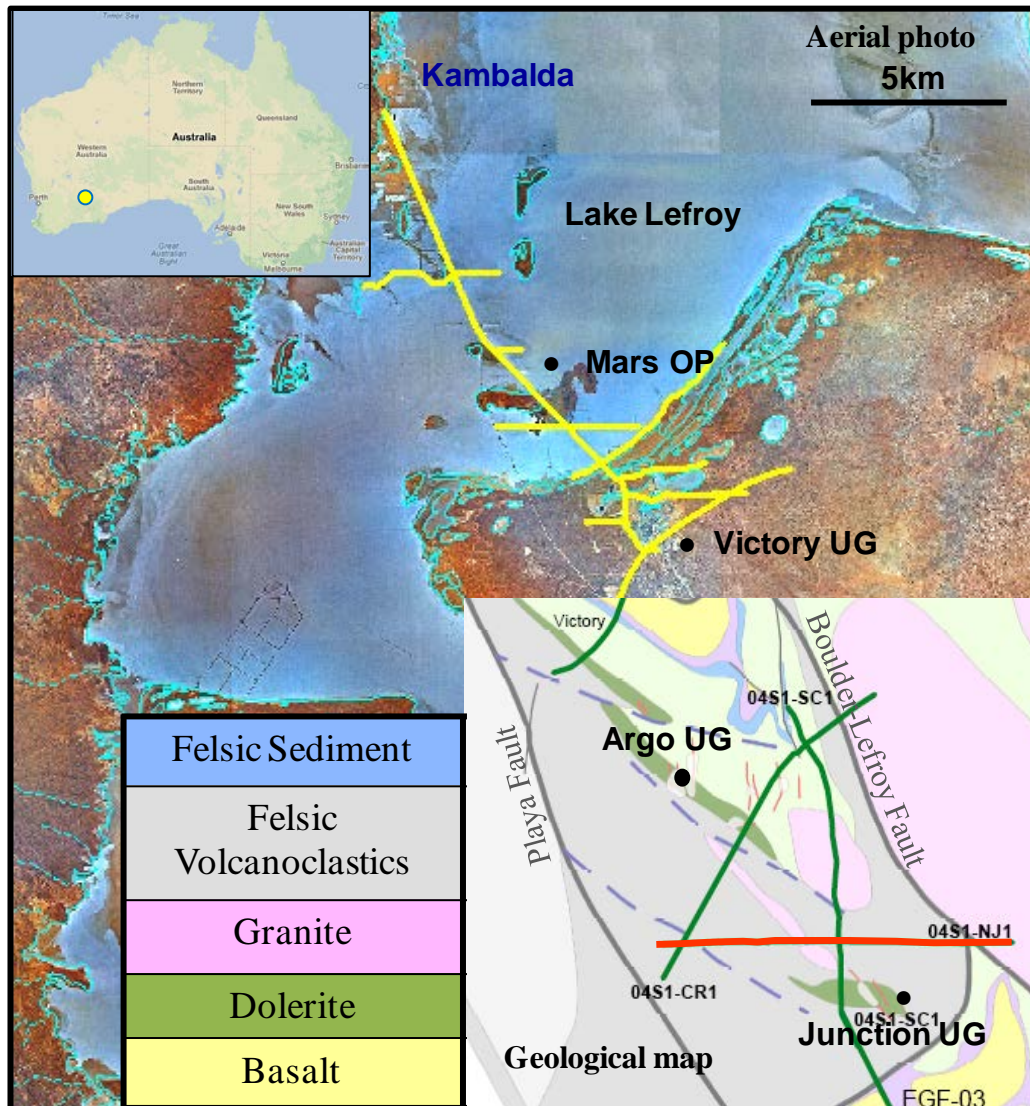


**Figure 5.37.** Location of the 2D seismic line SI-NJ1 (North Junction) – red line. The St. Ives gold camp in Western Australia. Yellow and green lines are 2D seismic profiles. (Harlan et al., 1983; Stolz et al., 2004).

The tested 2D seismic line is totally of 10.8 kilometres long. Two Hemi60 Vibroseis' were utilized to collect seismic data; geophone spacing was 10 meters, shot increment 10 meters. Acquisition parameters for the SI-NJ1 (North Junction) seismic line are listed in Table 2.

The seismic data have had rather variable quality and low signal to noise ratio as is typical for hard rock environments in Australia. For application of the presented prestack time imaging the processed dataset has been taken for an input. Processing

of the SI-NJ1 line was focused to preserve the reflection continuity. The acquired traces were edited and following procedures were applied to address the regolith heterogeneities and remove coherent and random noise: refraction and residual statics, muting, single and multi-channel filtering and amplitude corrections. Figure 5.38 shows typical processed shot gathers, each shot record is about 2.4 km long. Only the top 1000 ms of the dataset were considered for the input to the migration algorithm.

Instrument	ARAM24 NT recording system
Sample rate	1 millisecond
Record length	4 seconds
Source type	2× Hemi60
Shot Interval	20 and 10 meters
Receiver Interval	10 meters
Receiver Array	12 geophones inline
Spread	240 groups per shot record
Coverage	60 and 120 fold

**Table 2.** Acquisition parameters for the SI-NJ1 (North Junction) seismic line.

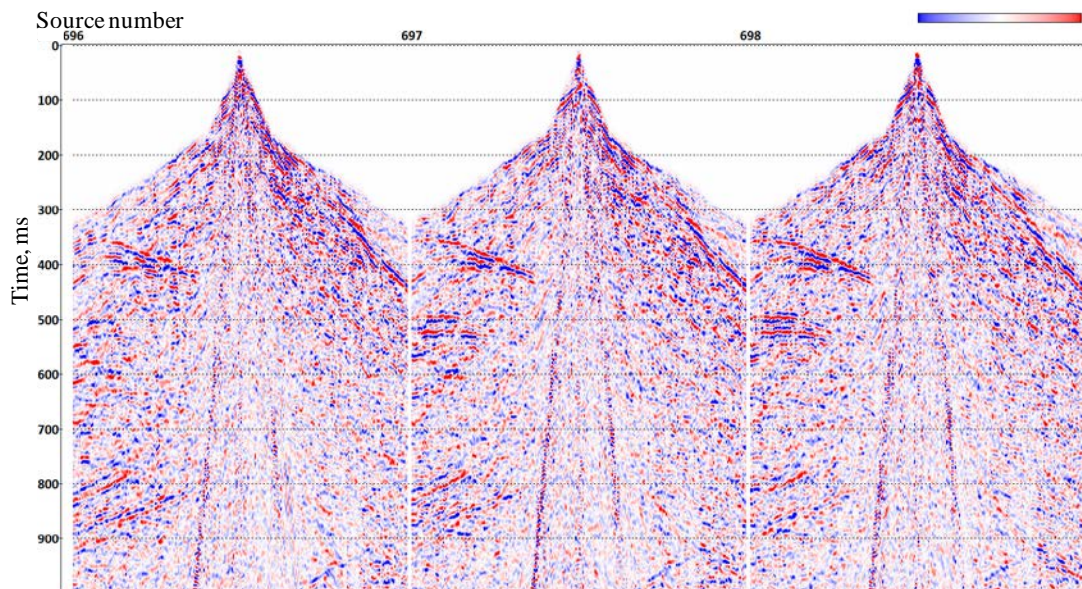


**Figure 5.38.** Processed shot records from the SI-NJ1 (North Junction) seismic line.

The field hard rock seismic data requires an accurate selection of the migration parameters. To deal with relatively high noise level a quite large searching window has been chosen for the local slopes estimation. To select neighbouring traces a radius of 100 meters (that gave up to 319 traces to analyse) was set up and 30 time samples were picked for the temporal direction. Figure 5.39 shows the velocity model obtained from the prestack imaging algorithm. The section defines different velocity patterns, which correspond to various rock formations. The final migrated section is presented in Figure 5.40. The seismic image defines deep geological structures as well as the regolith interface. Faults, shear zones and granite intrusions are identified on the section. The ‘sketch’ interpretation has been made based on regional geology information and seismic signal patterns. The strong dipping reflection from dolerite is clearly observed on the image, a number of reflections within the basalts formation define its structure. However, exact indication of lithological units and gold mineralization zones requires further analysis. Borehole logs and core measurements have to be used to calibrate seismic and analyse properties of reflected events.

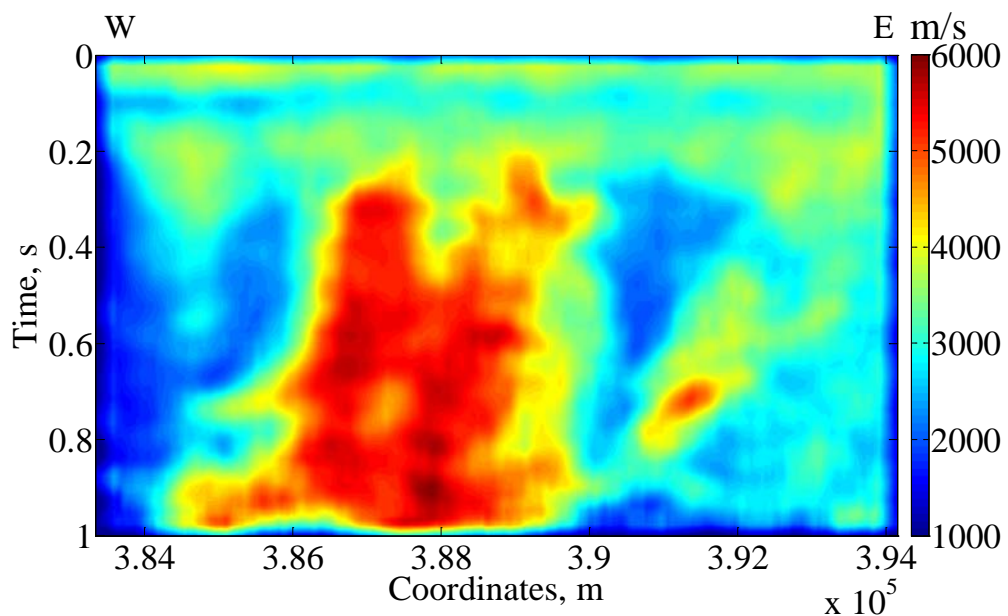


**Figure 5.39. Smoothed velocity model of the SI-NJ1 (North Junction) seismic line. St Ives mining camp.**

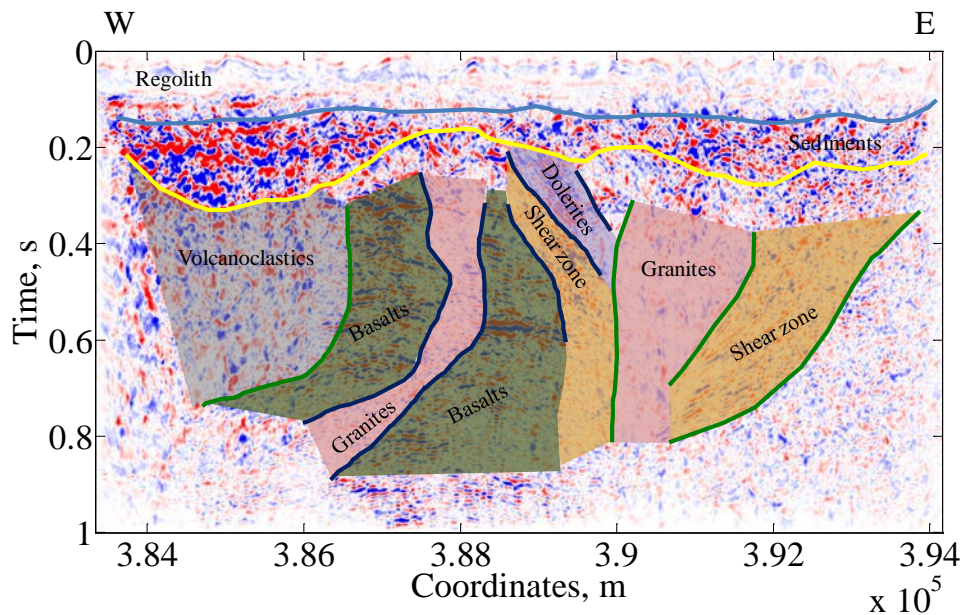


**Figure 5.40.** Migrated section of the SI-NJ1 (North Junction) seismic line. St Ives mining camp.

### 5.5. Velocity Independent Imaging Summary

The presented prestack time imaging algorithm has been studied on basic synthetic models and on a 2D synthetic model with simulated realistic geological settings, and applied to a real seismic 2D line acquired at the Kambalda region, Western Australia. The method is based on the estimation of local event slopes and recovers the actual location of the reflection point from that information.

The imaging technique has a number of benefits. The main benefit is that no input velocity model is required. This is important especially for hard rock sites, where information about velocities is often incomplete. In fact, a reasonably accurate velocity model is derived during the migration process. An additional benefit is that the estimated velocity model can be used as input for conventional migration techniques.

Careful tuning of migration parameters and introduced summation along the derived local slopes allow handling seismic data in the presence of high level random noise. This is a significant advantage for hard rock seismic exploration where data are commonly with a low level of signal to noise ratio. The quality of the final images

highly relies on a coherency of input data. Pre-processing with focusing on preservation of reflections should be performed prior to the migration. The migration considers only reflection and diffraction events, so any other coherent energy should be removed to avoid misleading errors in the results. Influence of anisotropy on results of the velocity-less migration has not been investigated in this study. However, the implemented method, which is based on estimation of the local slopes, seems can take into account the deviation of a reflected wave hyperbola from an isotropic case during the velocity derivation process.

There are no doubts that the pre-stack depth migration (PSDM) is superior to time-imaging approaches in complex hard rock geology. However, this technique is not easy to apply in such conditions due to a usually low signal-to-noise ratio in hard rock seismic data. The PSDM method is quite sensitive to the accuracy of the input velocity model. As was mentioned above obtaining the correct velocity estimation in severely noise data is a difficult task. I think at the moment the main obstacles for the PSDM to become a standard imaging method are: generally poor quality of data, difficulties in the velocity building, requirements of quite expensive iterative computations and lack of practical implementations. The time migration is more reliable to variations in the velocity model; imaging of the deep structures is not affected by inaccurate velocity estimations of shallow formations. And again the cost reason is playing a significant role in mineral seismic exploration for considering a particular migration method.

In hard rock environments strong reflection usually occurs from massive ore bodies; in such situations the current approach can provide a direct detection of mineral targets. Seismic surveys should be properly designed to be able to measure reflection energy from ore deposits, especially in cases with steeply dipping objects. Successful application of the presented algorithm to hard rock exploration requires a thorough analysis of a-priori geological information and seismic data.

## **6. Diffraction Imaging for Hard Rock Environments**

Hard rock seismic exploration is usually dealing with rather complex geological environments. These types of environments are usually characterized by a large number of local heterogeneities such as subvertical faults, fracture zones, and steeply dipping interfaces. The seismic data from such environments often have a poor signal to noise ratio caused by various reasons: rugged topography, heterogeneous structure of the regolith, high velocity contrast between overburden rocks and base formations, high ambient noise in case of the brownfield exploration etc. In such situations, the processing algorithms that are capable of handling data with a low signal to noise ratio and are able to image geological discontinuities and subvertical structures, are essential for reflection seismic exploration in hard rock environments.

### ***6.1. Diffraction Imaging***

Noise suppression and signal enhancement often involves summation or mixing of seismic traces along offset-traveltime curves. This approach is utilized in the classical normal moveout correction followed by stacking (Binns, 2004), common-reflection-surface (CRS) stack (Lydon, 1983), multifocusing (Lydon, 1988), a large variety of imaging methods based on Kirchhoff summation (Lydon, 1988) or even path-integral summation (Lipton, 2008). A broad overview of these methods has been given by Landa (2007). All of these techniques exploit the fact that the stacking of samples over a travel time curve should enhance signal to noise ratio for a particular event. Increasing the number of traces which are used for the summation can improve – with certain assumptions (Rietsch, 1980) – the quality of the noise suppression. This is a well exploited fact causing steady increase in the number of seismic channels in modern hardware and the nominal fold of the seismic surveys. The other example of the same approach is multifocusing that, compared to the conventional common-middle-point stacking, provides a multiple increase in data fold obtained through a better approximation of the travel time curve for reflections.

However, these algorithms often involve summation of a large number of traces with different levels of signal and noise; adding traces that have relatively low signal to

noise ratio does not necessarily improve the final image. To overcome this problem, a number of approaches have been proposed to exclude or weight traces based on their signal to noise ratio during the migration (or summation). Liu et al. (2009) proposed a stacking method based on a local correlation attribute and weighting traces prior to the common-middle-point summation. Berkhout and Palthe (1980) proposed an idea of limiting the Kirchhoff summation operator to disregard those parts of the record that are covered by coherent noise. Nemeth et al. (2000) published an algorithm of analysing the actual arrival paths of the propagating waves to split the signal and coherent noise.

Landa and Keydar (1998) presented an alternative imaging approach to deal with high noise level conditions. They used diffracted waves rather than specular reflections, and calculated the semblance function (Taner and Koehler, 1969) instead of a simple summation along the offset-traveltime curves of the diffracted waves. They also incorporated the semblance-based post-stack velocity analysis into their algorithm. Recently, Alonaizi et al. (2012) extended this algorithm into 3D zero-offset/stacked data case. In order to achieve this, they introduced an azimuth of linear/edge diffractors as an additional scanning parameter. They also showed that the semblance-based diffraction imaging is significantly more stable to the presence of random noise compared to the standard Kirchhoff migration.

The importance of diffraction for detection of geological heterogeneities has been studied for a long time and used as a tool that helps seismic interpretation. Krey (1952) demonstrated the value of diffraction for faults detection. A significant amount of research on numerical and field seismic data has been performed to study characteristics of seismic diffractions. The diffraction response and diffraction properties for zero-offset sections have been deduced by Trorey (1970); studies for a case of nonzero separation of source and receiver were presented in several publications (Berryhill, 1977; Trorey, 1970). The separation techniques of the diffraction events from the specular reflections have been published by a number of authors, as well as the utilization of diffractions for a structural imaging and velocity analysis. Harlan et al. (1983) reported the diffraction separation algorithm with use of that information for velocity estimation. Landa et al. (1987) proposed a method of

the diffractions detection in a common-offset domain. Kanasewich and Phadke (1988) presented a procedure to locate discontinuities in the common-fault-point (CFP) stacked section. Khaidukov et al. (2004) suggested a focusing-defocusing diffraction imaging, which aims to focus reflections to their imaginary source points and mute them from the full wavefield and subsequently obtain diffraction shot gathers. The method incorporated the coherency measurements and diffraction analysis proposed by Vermeulen et al. (2006) to improve the reliability of fault detection.

In this chapter an alteration of the 3D Kirchhoff post-stack migration algorithm and diffraction imaging are described. The modification utilizes coherency attributes obtained by the diffraction imaging algorithm in 3D to weight or steer the main Kirchhoff summation. The coherency attributes form the 3D volumes of focused diffraction energy that provides valuable information for hard rock exploration to detect subvertical objects and image other subsurface heterogeneities. The improvement in Kirchhoff migration increases quality of the final seismic images by excluding noise during the summation process.

## ***6.2. D-volumes and Steered Migration***

The study considers the 3D post-stack Kirchhoff time migration situation. A reflected wave from an interface can be viewed as a superposition of the waves diffracted from every point of the interface. This means that the offset-traveltime curve of the diffracted waves is tangent to the offset-traveltime curve of the specular reflection. Therefore all Kirchhoff migration algorithms comprise several common steps (Bancroft, 2007):

1. For each output location define a travel time curve for the diffracted wave;
2. Compute a weighted sum of the input samples along this travel time curve;
3. Place this sum into the output location;
4. Apply a wave-shaping filter.

For the 3D post-stack case, the data corresponding to a given reflected or diffracted wave belongs to a 3D-hypersurface. Conventionally, at the second step, the summation will occur along the complete diffracted wave travel time hypersurface, possibly with some corrections for the aperture. This surface is tangent to the actual travel time surface of the specular reflection only along a certain contact curve/point. All corresponding input samples along the surface will contribute to the summation while the actual signal energy is concentrated along one curve/direction only (shaded in light blue in Figure 6.1).

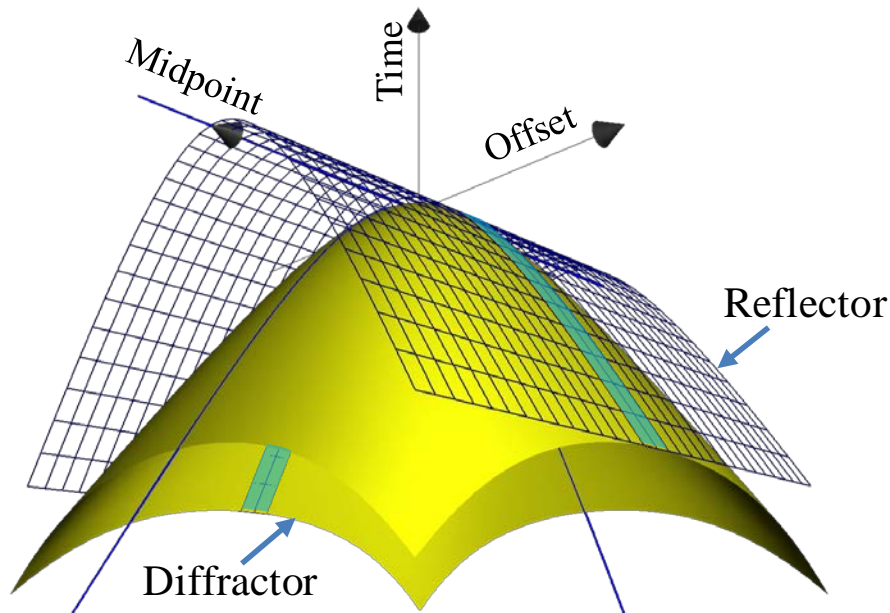


**Figure 6.1.** *Diffraction (yellow hypersurface) and reflection (blue celled surface) travel time surfaces. Tangent contact of the diffraction surface to the reflection surface is shaded in light blue.*

The main idea of the presented algorithm is to detect this direction and give the higher summation weights to the input samples close to this direction. By doing this, those areas of the diffracted wave travel time hypersurface that do not have sufficient signal energy and consequently decrease the signal to noise ratio of the output is effectively excluded. The 3D diffraction imaging technique proposed by Alonaizi et al. (2012) has been used to determinate these directions.

The workflow of the modified 3D post-stack Kirchhoff migration algorithm is provided below:

1. For each output location define an offset-traveltime curve of the diffracted wave given by:

$$t = \sqrt{t_0^2 + \frac{4l^2}{V_{NMO}^2}}, \quad (6-1)$$

where  $t_0$  is the corresponding zero-offset two-way travel time,  $l$  is the lateral offset from the scatterer and the velocity  $V_{NMO}$  is the stacking velocity obtained from velocity analysis (here we use usual Kirchhoff time migration assumptions, extension to the depth migration case is trivial).

2. For each horizontal direction (azimuth)  $\alpha$  select the portion of this travel-time surface limited by a lateral offset  $h$  from the straight line passing through the scatterer in this direction (Figure 6.2), then use the input data taken from the time window around the surface to compute the semblance:

$$W(\alpha) = \frac{\sum_{k=-m}^m (\sum_{i=1}^N f_{s(t,i)+k,i})^2}{N \sum_{k=-m}^m \sum_{i=1}^N f_{s(t,i)+k,i}^2}, \quad (6-2)$$

where  $i$  is the trace number,  $s(t,i)$  is the sample number which corresponds to the diffracted wave travel time  $t$  in the  $i^{th}$  trace,  $f_{j,i}$  is the  $j^{th}$  sample of the  $i^{th}$  trace,  $2m$  is the time window (given by the number of samples) and  $N$  is the number of traces in the selection.

3. Compute a weighted sum of the input samples along this travel time curve using  $W(\alpha)$  as a weighting function.
4. Place this sum into the output location.
5. Apply a wave-shaping filter.

Diffracted waves contain valuable information about subsurface structure; they are capable of detecting scattered objects which are smaller than the recorded wavelength. Hard rock environments usually include a lot of discontinuities of different kind (faults, fracture and alteration zones, etc.) and often they are aligned

with mineralization occurrences and become an exploration target. Thus, the ability to delineate such objects is beneficial for mineral exploration.

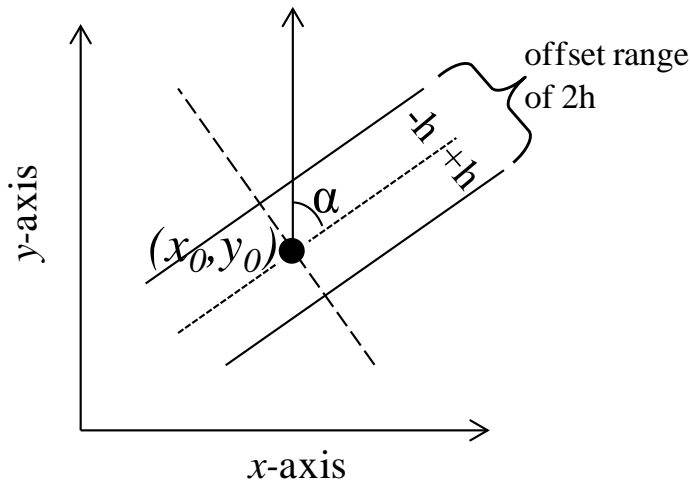


**Figure 6.2.** Selection of the travel time surface portion for the semblance calculation (plane view) (2D projection of Figure 6.1).  $\alpha$  is a horizontal azimuth,  $h$  is a lateral offset, the dashed line is where the diffraction traveltime is split for phase change.

Herein, the method of focusing the diffraction energy from scattering points on the common-diffractor-point volume (D-volume) (Alonaizi et al., 2012; Landa and Keydar, 1998) has been used to trace local heterogeneities. The approach is defined by a procedure of measuring the coherency along a diffraction hyperboloid using semblance function (equation 6-2), and it enhances the amplitude of the seismic signal at the location of the local diffractors on the D-volume. Diffractions from linear elements are formed by superposition of signals along hyperboloids generated from every scatter point on the object. In the case of edge diffractions, there is the 180 degree phase change across the diffraction traveltime apex (Figure 3.9a) (Trorey, 1970). This fact can be used in order to separate diffractions from other wavefield components and to distinguish the diffraction produced from the edges of structural objects and mineral bodies.

The maximum semblance values (equation 6-2) obtained for every sample of the image form the D-volume, which is used for detection of geological targets. Diffraction from elongated objects is represented by overlapping of signals along diffraction hyperboloids. In such cases, only a part of every diffraction surface that is contributing to the total envelope of the overlapped hyperboloids along the linear segment has to be focused. The maximum semblance values are used to form the D-volume in order to emphasize orientation of the diffraction linear objects (fault, fracture zones). The robustness of the D-volume imaging in the presence of band-limited random noise for resolution in time (vertical resolution) has been shown by Alonaizi et al. (2013). Two types of D-volume can be defined: the first one is the volume computed with the phase change taken into account; another one evaluated without consideration of that phenomenon. Computation of the phase shift D-volume requires flipping of the signal polarity along a line passing through the image point in the direction of the selected azimuth at the second step of the migration workflow. Both types of the D-volumes can serve as an effective tool for reliable detection of local heterogeneities, linear and subvertical objects. The variant with the phase change consideration emphasizes the edges of truncated interfaces and local geological objects.

### ***6.3. Synthetic Data Example***

To evaluate the capability of the proposed steered migration algorithm, the method was applied to a synthetic 3D data set. The synthetic 3D model consists of 200 in-lines and 100 cross-lines; bin size is 10 by 10 meters. Seismic wave velocity is constant and equal to 2000 m/s. The model includes one horizontal interface and six reflectors with various dip angles. The range of dips is from  $10^\circ$  to  $60^\circ$ , with increment ten degrees (Figure 6.3). The synthetic data set is constructed by convolution of spike-traces with the zero-phase wavelet with the frequency band conventional for a seismic data acquisition (5-70 Hz). The migration algorithm is tested on this synthetic dataset in the presence of a high level of band-limited random noise. The amplitude spectrum of the noise is the same as the amplitude spectra of the signal, which results in constant signal to noise ratio for the entire frequency range. Figure 6.4 shows two cross-sections of the 3D synthetic cubes; the left one is a

noise free section, the right one is the section with 50% of random noise added to the dataset.

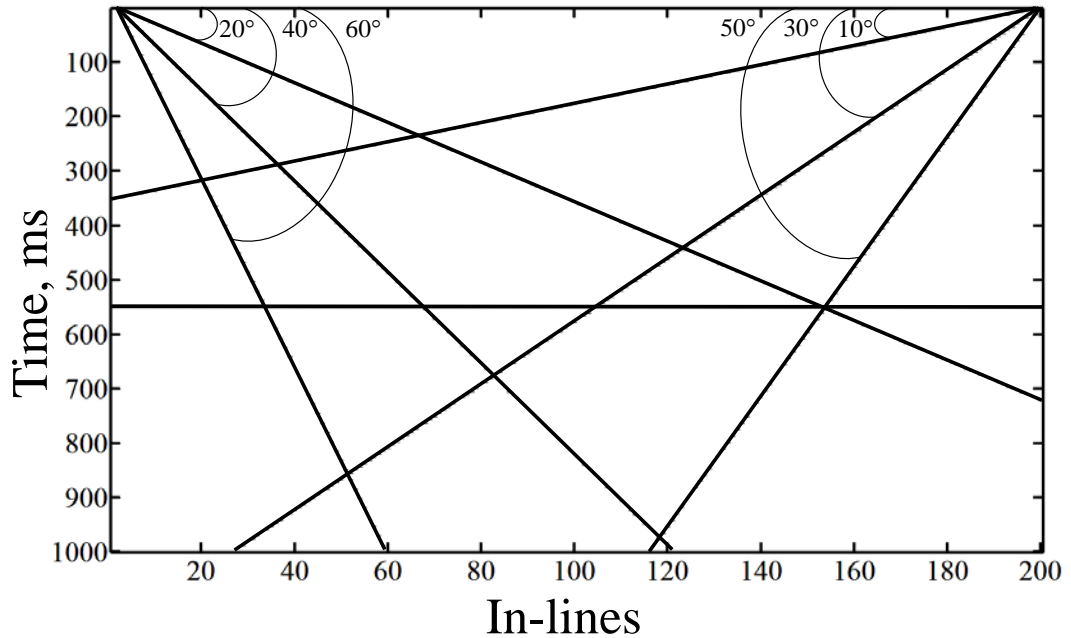


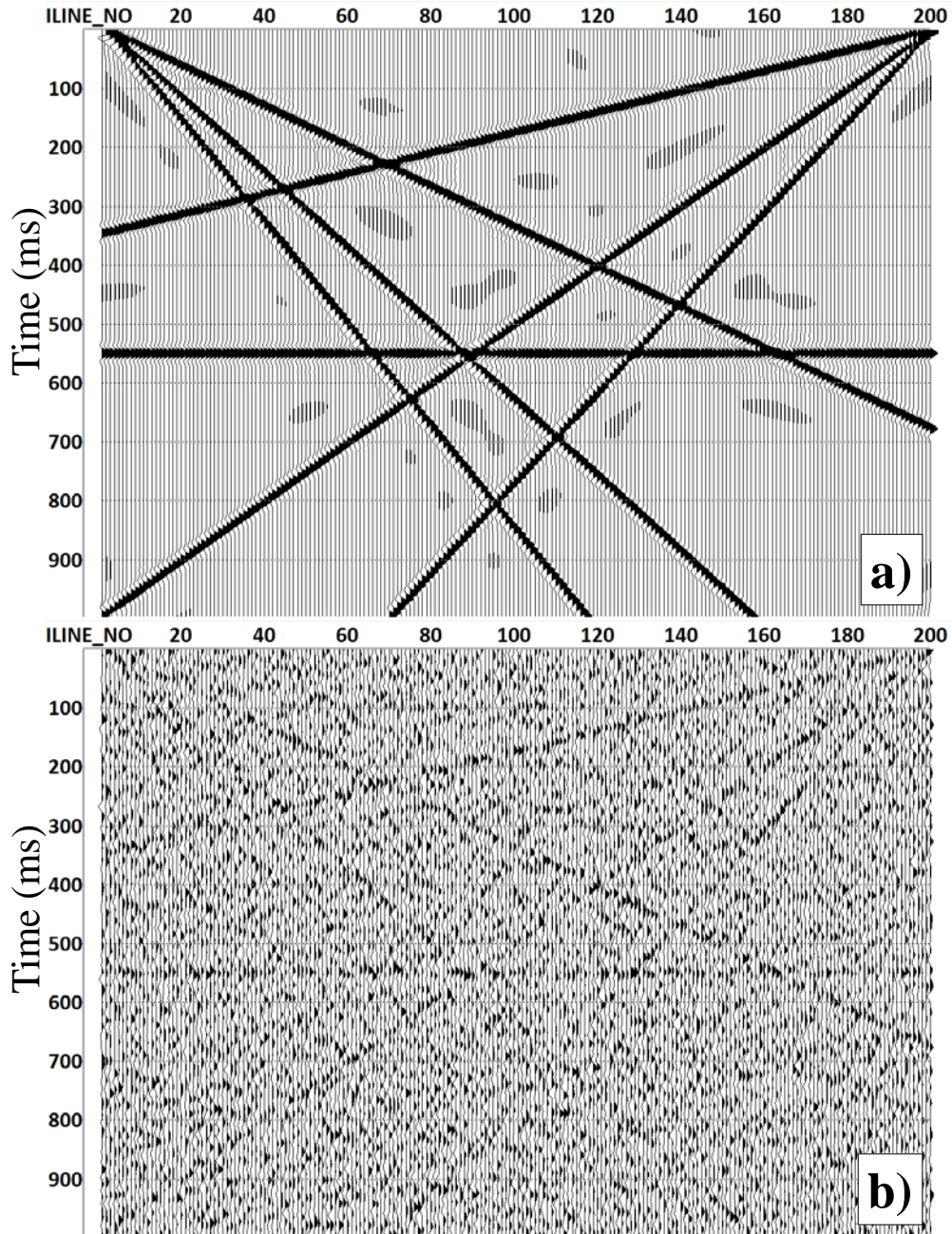
**Figure 6.3.** *Cross-line section of the model for the generated synthetic data set.*

In order to study the stability of the method to presence of a band-limited random noise, the steered Kirchhoff migration and standard Kirchhoff migration were applied to the synthetic dataset. The following parameters have been used for the steered algorithm:

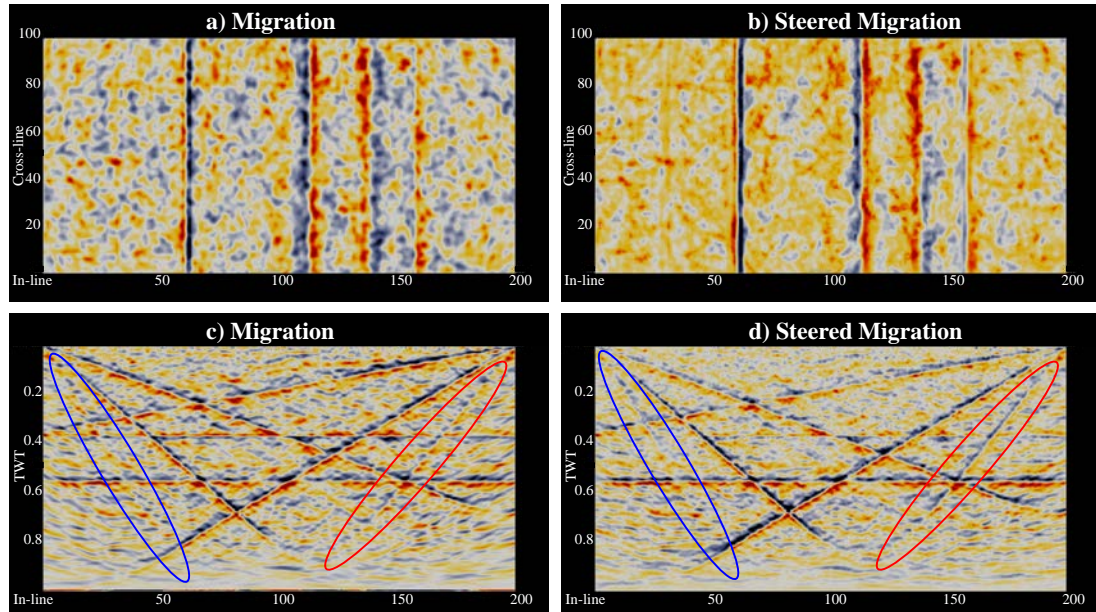
- angle increment for diffraction azimuth scanning  $\alpha$  is  $5^\circ$ ,
- lateral offset limit for the searching directions  $h$  is 50 m,
- time window used for semblance function calculation is 30 ms.

Figure 6.5 shows a comparison of these imaging approaches. Figure 6.5a and 6.5b show a 500 ms time slice of the migration results of the conventional and steered approaches respectively. Data on the steered migration time slice look less noisy and smoother; the interfaces are sharper and well-defined. Figure 6.5c and 6.5d show the vertical cross-section of the migrated data. The steered migration section appears with less noise artefacts and all horizons are clearly detectable. The biggest

improvement is in the imaging of the steeply dipping interfaces. The steepest interfaces with  $50^\circ$  and  $60^\circ$  slopes are highlighted with red and blue circles respectively.



*Figure 6.4. (a) Noise free cross-line section of the synthetic dataset. (b) The same section after adding 50% of random noise.*



**Figure 6.5.** Comparison of the standard Kirchhoff migration and the steered Kirchhoff migration of the 3D synthetic data with 50% of random noise. (a) Time-slice (500 ms) of the standard Kirchhoff migration. (b) Time-slice (500 ms) of the steered Kirchhoff migration. (c) Cross-section of the standard Kirchhoff migration. (d) Cross-section of the steered Kirchhoff migration. The steepest interfaces with  $50^\circ$  and  $60^\circ$  slopes are highlighted on the cross-sections in red and blue circles, respectively.

#### 6.4. Field Example 1 – O’Callaghans Mine Site

The field 3D seismic dataset was acquired at the O’Callaghans mine site in the Pilbara region, Western Australia (Figure 6.6). This site is associated with a neoproterozoic polymetallic laterally extensive skarn deposits confined to dome structures (Rowins, 1998). The O’Callaghans’ skarn formation is located about 350 meters below surface on top of the granite block and overlying by the limestone sequence, and it has thickness approximately 5 to 70 meters. The deposit contains a high grade of tungsten, copper, lead and zinc. The estimated tungsten resources are one of the world’s largest (Li, 2009).

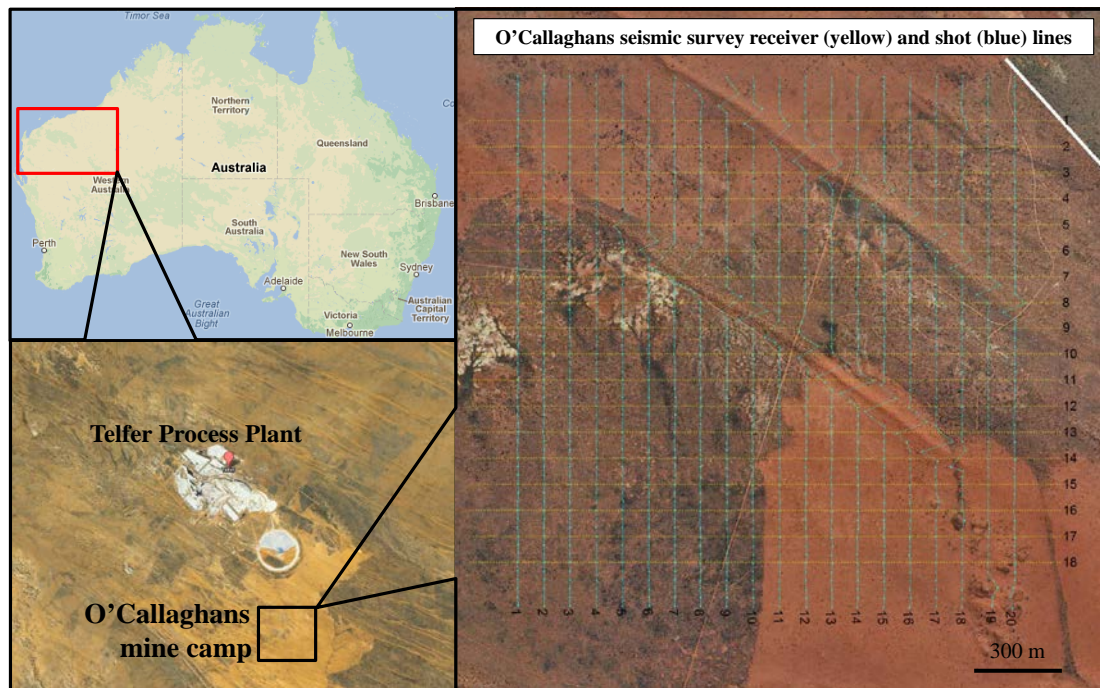


**Figure 6.6.** Location of the 3D seismic survey at the O'Callaghans mine site (Western Australia) (Images provided by Google Earth 2011).

The survey area was approximately 3.8 km<sup>2</sup>; a F10 Hurricane weight drop was used as a seismic source for the acquisition. The parameters of the seismic survey are shown in Table 3. Geology of the mining site is characterized by the presence of a deep and heterogeneous regolith zone and a complex underground structure. The seismic data had a low signal to noise ratio. The following processing steps were done to produce the final 3D migrated seismic cube: refraction static corrections and residual reflection static were applied to equalise travel times through the low velocity weathered regolith layer; amplitude corrections, single-channel and 2D filtering were used to increase signal to noise ratio. The velocity model estimation was performed taking zero-offset vertical seismic profiling data into account. 3D velocity model was built as an input for the steered migration. The DMO corrections were applied for layer's dips to improve continuity of interfaces.

Source	1425 kg Weight drop
Number of source points	1989
Source spacing	30 m
Source line spacing	90 m
Number of Receiver lines	18
Receiver line spacing	90 m
Receiver point spacing	10 m
Record length	3 s
Sample rate	2 ms

**Table 3. Acquisition parameters used for the 3D seismic surveys acquired at O'Callaghans mine site.**

The steered migration algorithm was applied to the DMO-corrected stacked 3D seismic volume. The 3D stacking velocity volume was used for the migration. The following calculation parameters for the steered approach have been chosen: the angle increment for diffraction azimuth scanning is  $5^\circ$ , the lateral offset limit for the searching directions is 50 m, and the time window to estimate the semblance around the diffracted travel time curve is 30 ms.

Figure 6.7 shows a comparison of the vertical slices (xline 88) of the 3D seismic dataset obtained using the standard Kirchhoff migration and the steered imaging technique. The steered migration image looks cleaner; the reflections (dome's flanks) at the upper part of the section appear as continuous events. Figure 6.8 presents a comparison of the 178 ms time slices of the 3D seismic volume obtained with the standard Kirchhoff migration algorithm, steered Kirchhoff approach and D-volume from the diffraction imaging technique. As can be seen most of the subsurface features and objects, which are observed on both D-volume and steered Kirchhoff migration images, are traced on the ordinary Kirchhoff time migrated section as well. The D-volume image shows the concentration of the diffraction energy on sharp heterogeneities. Many small faults and fractures are identified on the D-volume time slice. The steered migration slice has much better quality in terms of signal to noise ratio; a number of objects, which could be identified as faults, are reliably traced on the image. From these comparisons it is apparent that the steered imaging approach

reduces the noise and significantly improves quality of the migrated images. Results from the steered migration have higher potential for a successful interpretation.

To confirm that the maximum semblance values shown in the D-volume attribute do actually agree with locations of the linear diffraction objects (faults, edges), a point on the D-volume of O'Callaghans dataset at the time slice 178 ms and located on the in-line 72 and cross-line 25 was chosen for consideration. The maximum semblance value at that point against azimuths was then plotted and compared with a time slice extracted from the D-volume of the same data (Figure 6.9). The maximum semblance value changes significantly with azimuth; the highest values correspond to the north-south direction. This coincides with the positioning of the possible fault.

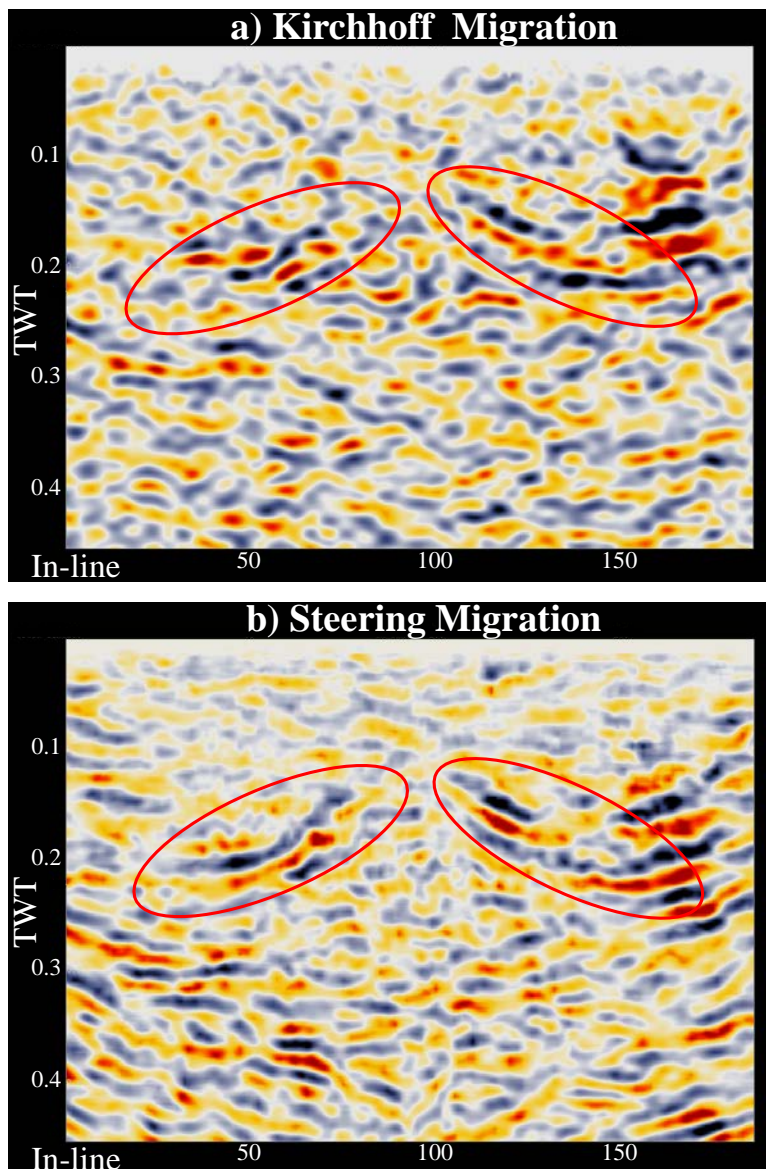


*Figure 6.7. Comparison of a vertical slice (xline 88) of the 3D seismic volume obtained with (a) standard Kirchhoff migration and (b) steered Kirchhoff migration. Red circles highlight improvement of imaging the dome's flanks.*

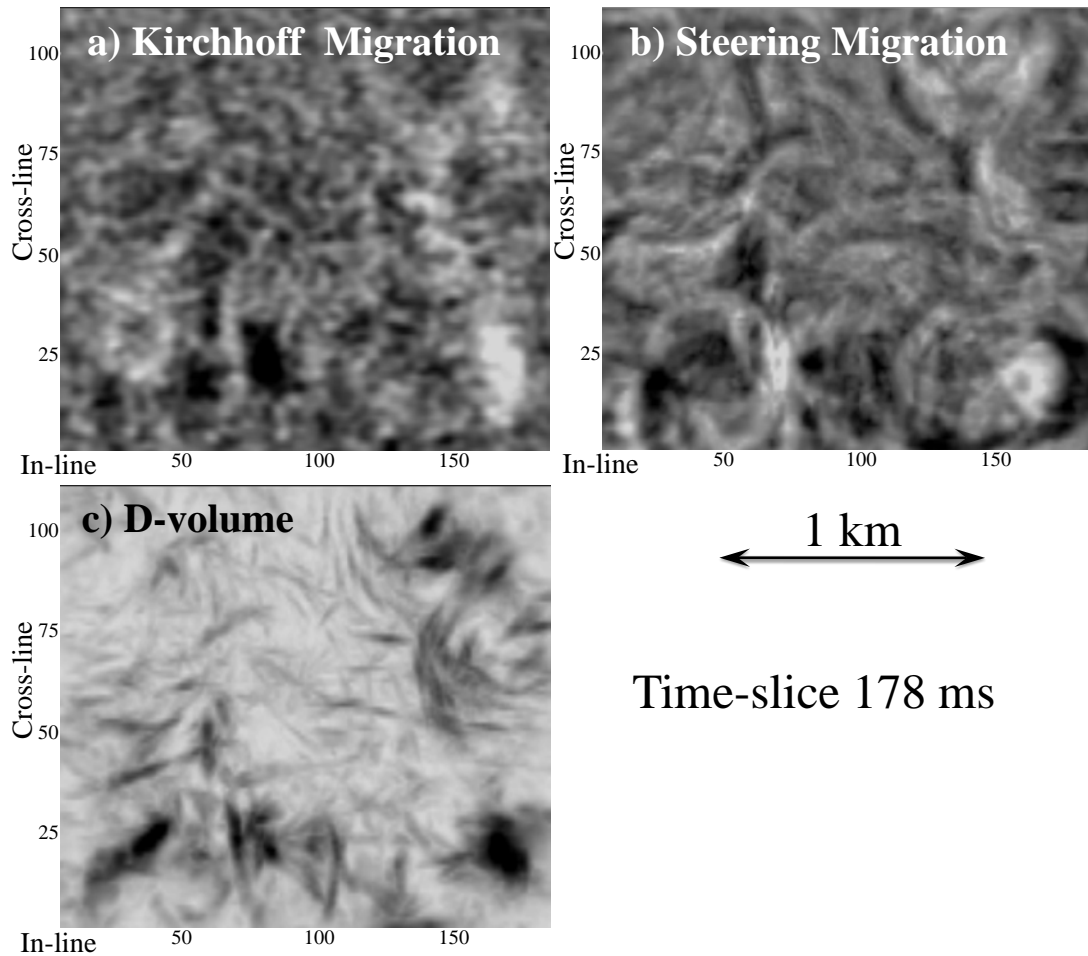


**Figure 6.8.** Comparison of time-slice (178 ms) of the 3D seismic volume obtained with (a) standard Kirchhoff migration, (b) steered Kirchhoff migration and (c) diffraction imaging technique (D-volume).

Figure 6.10 presents the steered migration section of the cross-line 88 with the geological interpretation. The potential mineralized skarn formation is delineated on the image and overlaid by clastic carbonate strata. The skarn metamorphism is caused by a granite intrusion. The O'Callaghans' proximal skarn-style mineralization represents a polymetallic mineral zone, which is mainly enriched by copper, zinc, lead and tungsten.

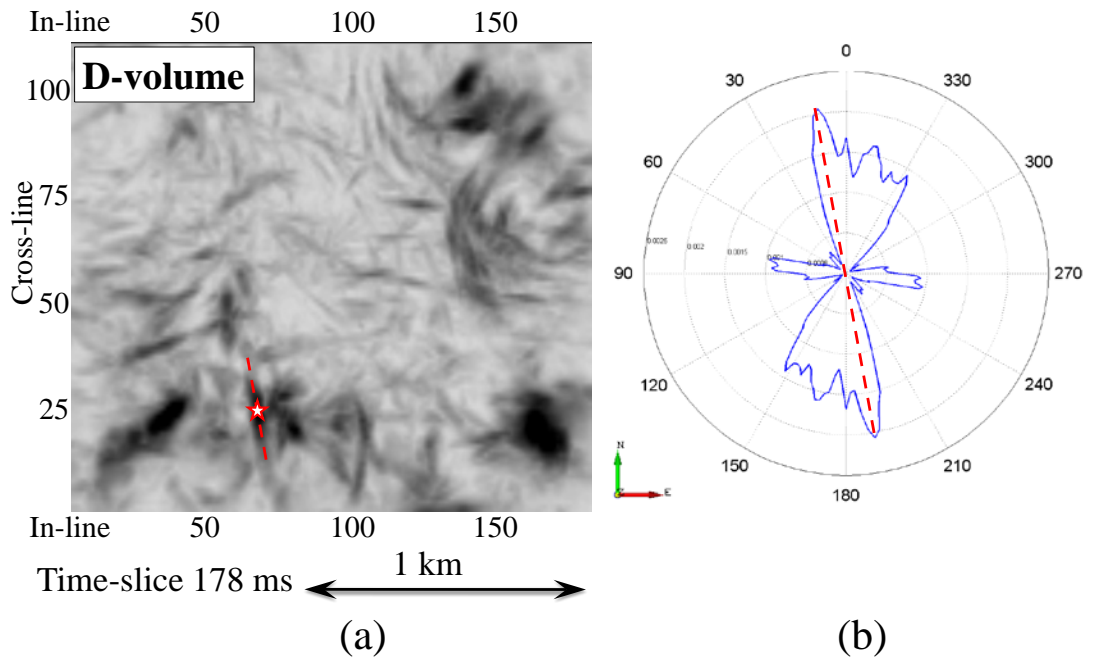


**Figure 9.** (a) A point-star at the time slice 178 ms, located at in-line 72 and cross-line 25 and (b) the maximum semblance values of that point as a function of azimuth indicating the orientation of the diffraction object. The maximum semblance values show the direction of the possible fault.

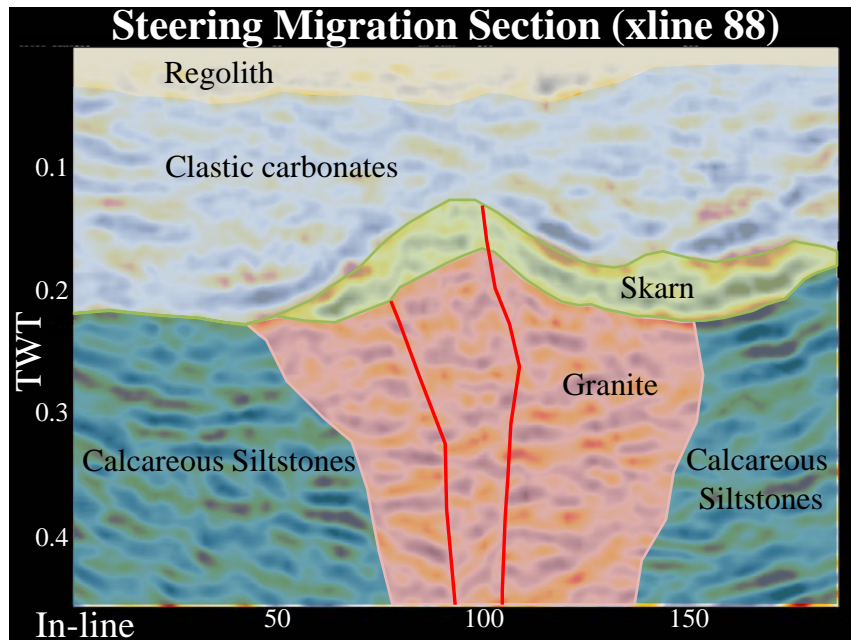


*Figure 6.10. Steered Migration Section (Xline 88). Geological interpretation is overlaid onto the migrated image. Red lines are faults.*

### **6.5. Field Example 2 – Hillside Mine Site**

The field 3D seismic dataset was acquired at Hillside mine site, located on the Yorke Peninsula (South Australia). This is the same mining camp, where the 2D seismic experiment, described in Chapter 4.2, was carried out. The copper-gold mineralization areas are associated with subvertical fault zones (Figure 4.2). One of the main objectives of the 3D seismic survey was to image and define steeply dipping multiple faulting patterns, fracture and alteration zones.

The survey covered 0.85 km<sup>2</sup> and the data were acquired from east to west. The seismic data were acquired with a 10 m shot and 5 m receiver spacing through the 5 patches that has an overlap of 50%. Figure 6.11 shows a CDP fold map. An EX-6 distributed seismic system with 96-channels and SM24 10 Hz geophones were used to acquire the seismic data. The distributed system consists of several acquisition units, each of them collecting 6 channels of data. 20 solar panels were used to supply

necessary energy to the survey equipment. A 720 kg F9 Hurricane accelerated weight drop was assembled on a bobcat and used as a source of seismic waves. A Wireless Optical Triggering Box (WTB) and piezoelectric sensor attached to a force spreading plate were used to synchronise shooting and recording. The length of the record was 2 seconds; sample rate was 2 ms. The acquisition parameters of the seismic survey are listed in Table 4. The processing of the acquired 3D seismic dataset was focused on overcoming the regolith heterogeneities and increasing signal to noise ratio. To compensate travel times through the low velocity weathered regolith overburden the refraction static corrections and residual reflection static were applied to the seismic volume. The following processing procedures were used to address noise issues: amplitude compensations, single-channel and 2D filtering. The DMO corrections were applied for objects' slopes to improve quality of stacked data.

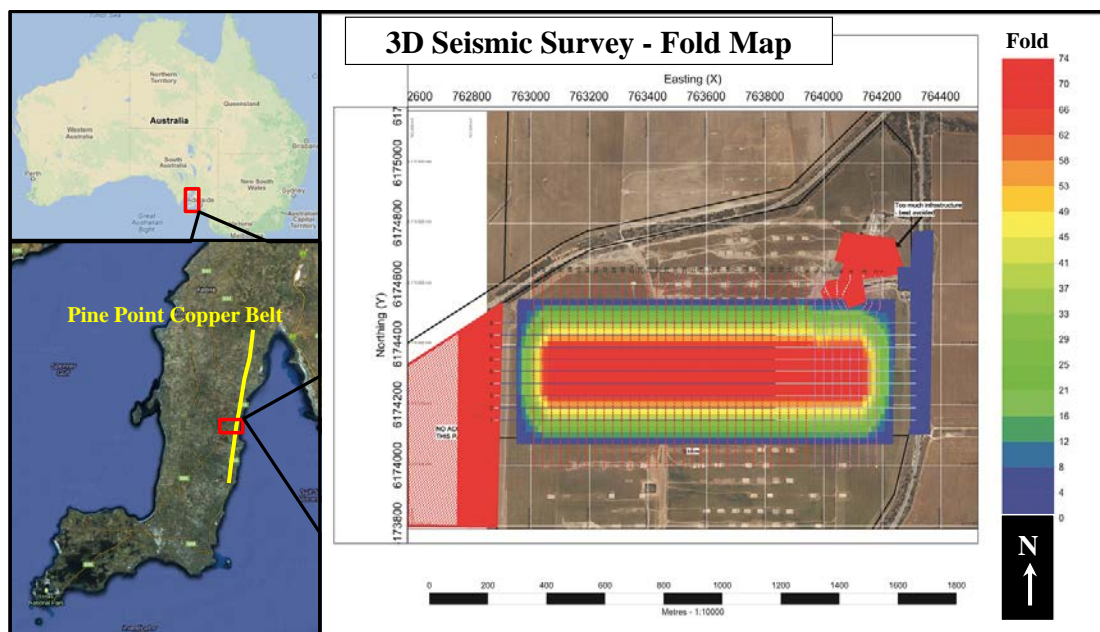


*Figure 6.11. Location of the 3D seismic survey at the Hillside mine site (South Australia) and a CDP fold map of the survey (Images provided by Google Earth 2011).*

Source	720 kg Weight drop
Number of patches	5
Source points per patch	512
Source spacing	10 m
Source line spacing	40 m
Receiver lines per patch	9
Receiver line spacing	30 m
Receiver point spacing	5 m
Record length	2 s
Sample rate	2 ms
Patches overlapping	50 %

***Table 4. Acquisition parameters used for the 3D seismic surveys acquired at Hillside mine site.***

The steered migration algorithm was applied to the stacked 3D seismic volume. A linear velocity function was used for the migration (gradually increasing velocity from 3200 m/s to 4500 m/s in time interval 0-300 ms; constant velocity 4500 m/s below 300 ms). The following calculation parameters for the steered approach have been selected: the angle increment for azimuth scanning is 5°, the lateral offset limit for the searching directions is 50 m, and the time window to estimate the semblance around the diffracted travel time curve is 30 ms.

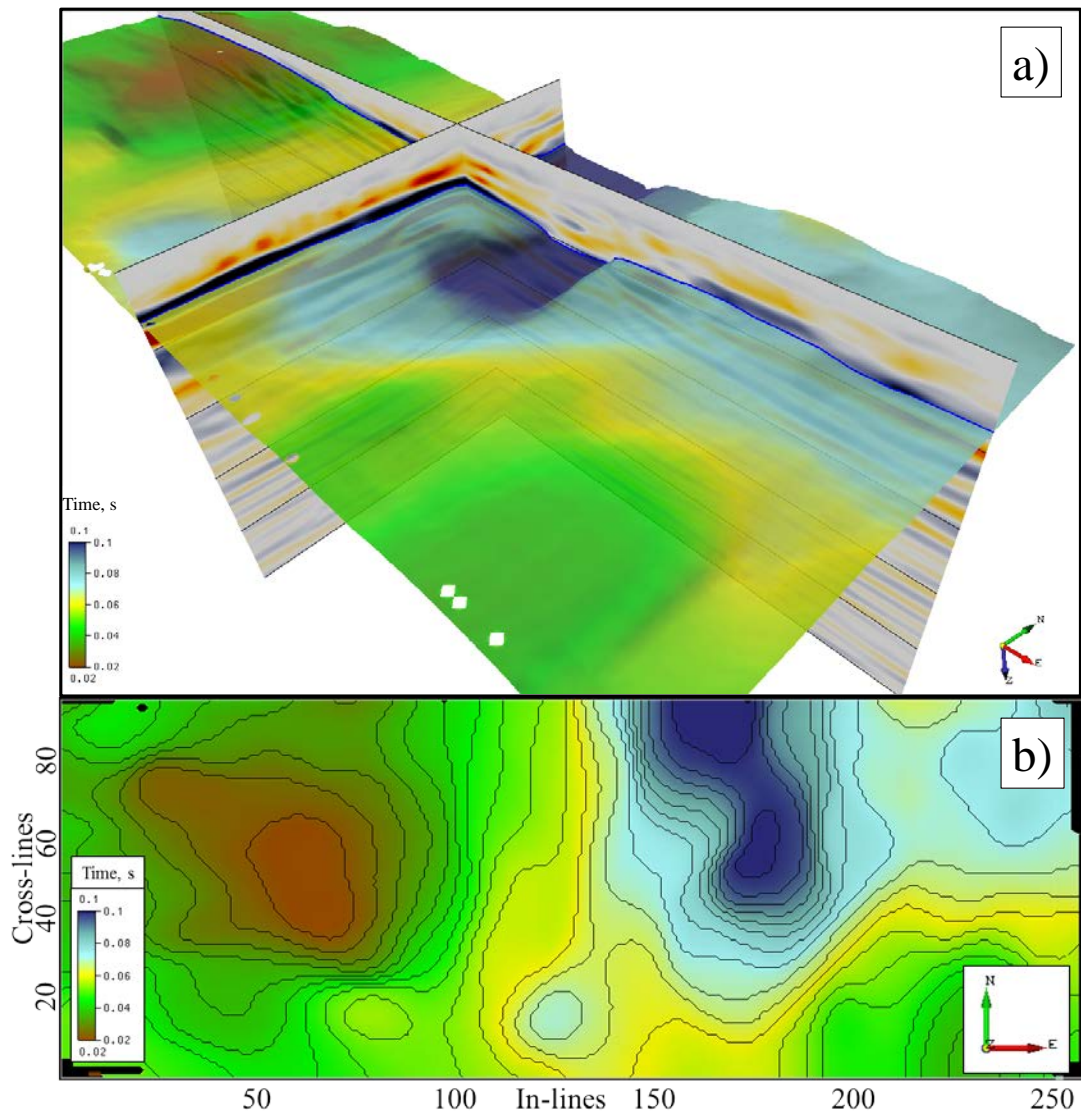


**Figure 6.12. a) Example of steered migrated 3D seismic cube with the interface of the regolith overburden. b) Map of the bottom of the weathered regolith layer.**

The geology at the Hillside camp is highly complex, and to reveal geological structures and delineate mineralization zones the steered migrated 3D seismic cube (Figure 6.12a) has been used as a support for data analysis and interpretation. The structure of the near surface weathered formation has been investigated through the 3D seismic volume. Figure 6.12b shows a map of the bottom interface of the regolith overburden; this information is required not only for geological characterization of the area but also useful for mining planning and design.

To investigate the complexity of subvertical geology at the Hillside camp the diffraction volume with the phase-reversal feature from edge diffractions has been computed. Figure 6.13a shows the time-slice at 120 ms of the diffraction volume which has been calculated taking into account the phase change. The example of distribution of diffraction energy at the same time-slice, which was computed without phase-reversal, is shown in Figure 6.13b. The extended zone of maxima on the left in the upper image of Figure 6.13 defines a location of the subvertical Pine Point Fault Zone, which separates the western mafic schist's sequence (Lowe, 2009) from the central complex metasediment/gabbro formation. Two red lines on both images outline the Eastern Fault/Fracture Zone; the eastern part from that zone is characterized by the presence of massive granite intrusions, one of them is imaged by the diffraction maximum in the upper right corner of the bottom panel. Figure 6.13b identifies two linear maxima areas, which correspond to the Dart and Zanoni Mineralized Fault Zones. The central part is a complex structure and formed mainly by metasedimentary/skarn rocks with a massive gabbro intrusion (area circled blue) complicated by faults/fractures and granite discordant intrusions. Application of the steered migration made it possible to determine the main subvertical linear geological features at the Hillside mine site.

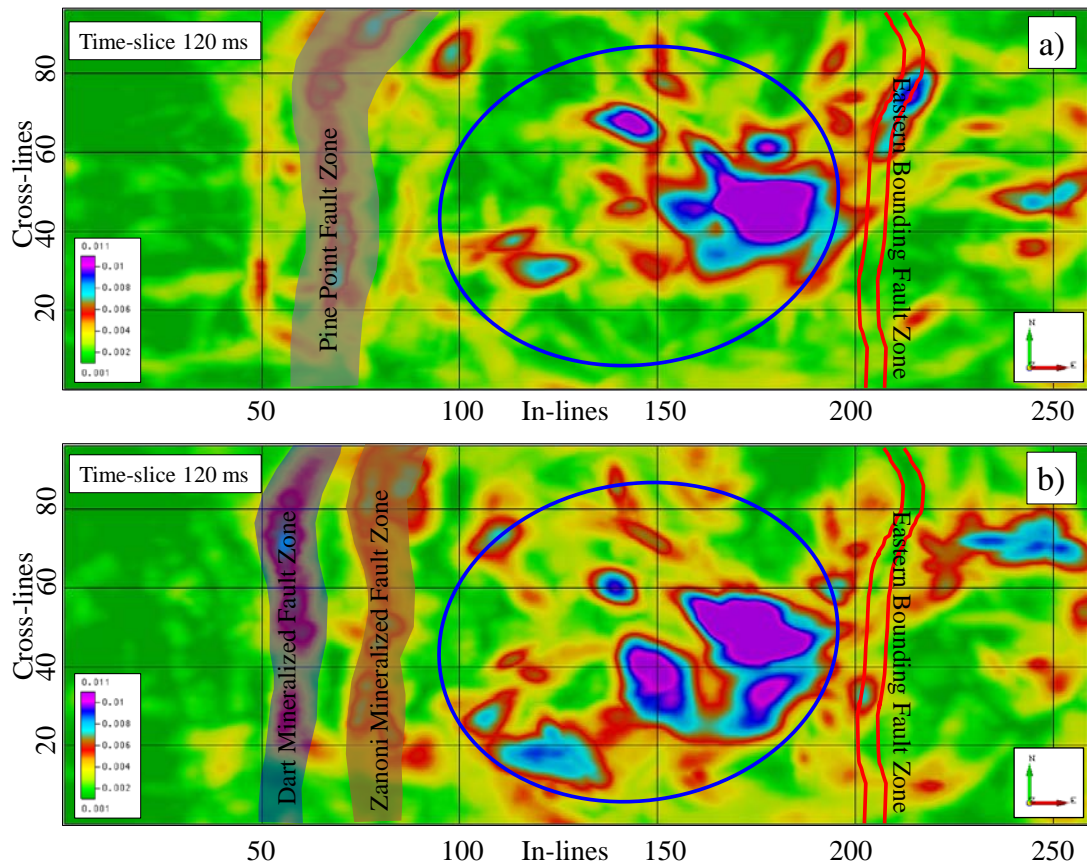


**Figure 6.13.** Time-slices at 120 ms of D-volumes with an indication of main linear geological features. a) The computed D-volume with taking into account the phase-reversal phenomenon. b) The computed D-volume without phase reversal. The area with presence of gabbro intrusions is circled in blue.

### 6.6. Field Example 3 – Solwara Mine Site

The marine 3D seismic dataset was collected at Solwara 1 site in Bismark Sea, west of New Ireland, Papua New Guinea (Figure 6.14). Solwara 1 is a Seafloor Massive Sulfide (SMS) deposit. The deposit contains high grade of base metals (copper, zinc) and precious metals (silver, gold). In the southwest Pacific region the seabed mineral deposits are mainly associated with subduction zones and located usually at island- and back-arcs spreading centres at the ocean rims (Figure 6.14). The submarine sulfide depositions are confined to hydrothermal vents, where the discharging hot fluids mix with cold oceanic water, and form mound-chimney type of accumulations. The chimney structures are made up through sulfides precipitation at the vent site.

The formation of seafloor sulphide mounds occurs due to cyclically repeatable processes: occasional flux of hydrothermal fluids, sea floor oxidation, collapsing of old chimneys, triggered by tectonic events and origination of new chimney structures. Subsequent growth of a mound with accompanying decrease of the permeability takes place till precipitation, replacement and remobilization of sulfides begins to occur inside the mound. As a consequence, minerals are concentrated in the massive deposit (Lydon, 1988).

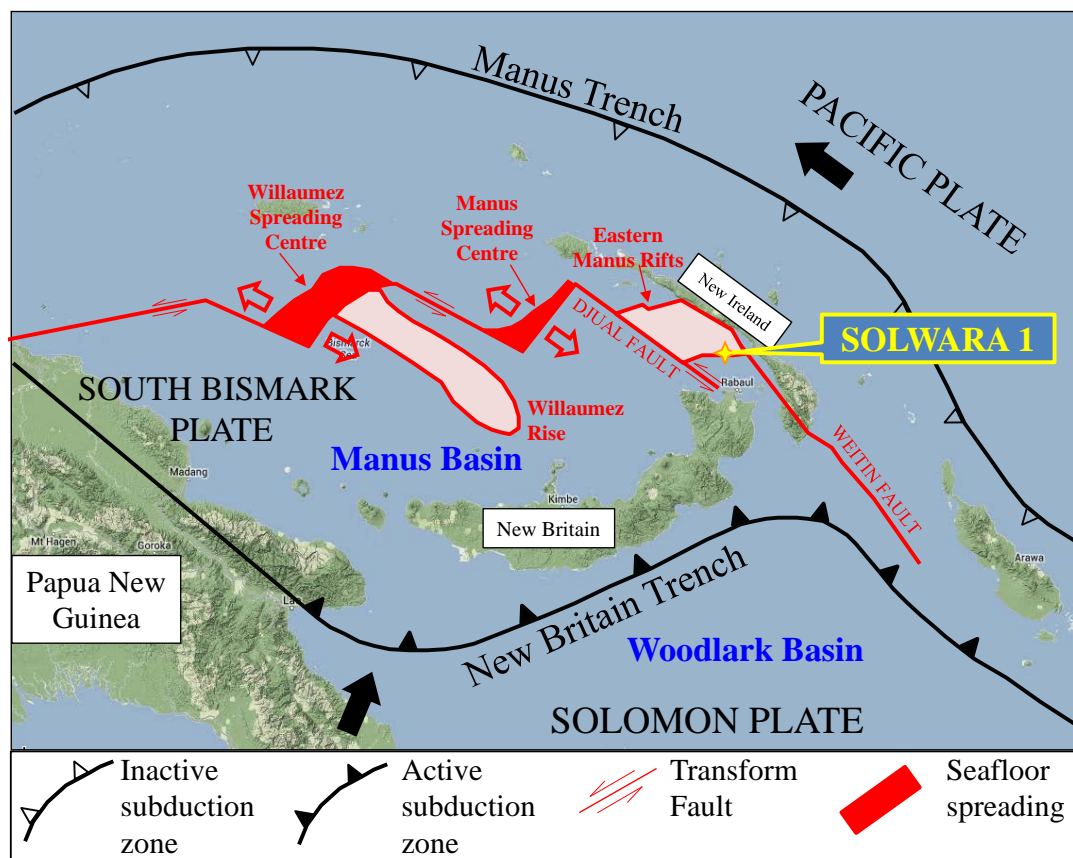


**Figure 6.14. Location of the Solwara 1 site. Main tectonic elements and structures of the Manus Basin region (Moss and Scott, 2001) (Image provided by Google Earth 2011).**

The Solwara 1 sulfide deposit is located on a deep oceanic platform (approximately 1500 m below sea level). The deposit is hosted by a basalt volcanic ridge with two andesite-dacite summits and mainly situated on the crests of the ridges. The area contains a number of hydrothermal chimneys with average height of 10 m. The mineral formation is covered locally by unconsolidated sediments with thickness

from 0 to 4 m. The main mineralized sulphide-dominant rocks is comprised of pyrite and chalcopyrite with andesite or barite gangue and has a thickness range from 0 to 30 m (Lipton, 2012).

The 3D seismic survey consisted of 173 sail lines and covered 6.57 km<sup>2</sup>. The dataset has an inline spacing of 6.25 m and a cross-line spacing of 6.25 m. Seismic lines were acquired using a 2 x 40 cubic inch sleeve airgun array and a 48 trace streamer with 12.5 m groups spacing and 12.5 m shot interval. Traces were recorded with a 3.5 second record length and 0.5 ms sampling rate.

The presented diffraction imaging was applied to the stacked 3D seismic dataset. A constant velocity of 1500 m/s was used for the migration. The following input settings have been used for the steered migration: the angle increment for diffraction azimuth scanning is 5°, the lateral offset limit for the searching directions is 50 m, and the time window to estimate the semblance around the diffracted travel time curve is 30 ms.

Despite the fact that all prospective sulfide mineralization zones are concentrated on the seafloor, knowledge of internal deep geological structures of seabed volcanic ridges and their genesis is important for understanding of the formation of mineral deposits and as a consequence for new discoveries. Figure 6.15b shows the in-line 150 section of the computed D-volume; the linear features, which are clearly seen in the section by following the concentration of diffraction energy, are circled blue. These two objects are untraceable in the Kirchhoff migrated section (Figure 6.15a). The structures may represent low-angle thrusts, which are usually hydrothermal fluid migration paths. Figure 6.16 shows examples of the 2528 ms time-slices of the Solwara 1 3D seismic volume of the standard Kirchhoff migration (left panel) and the steered migration (right panel). There is a significant improvement of the image quality in the steered migration time-slice. This image has much more clear and continuous features, whereas the Kirchhoff time-slice contains a lot of noise.

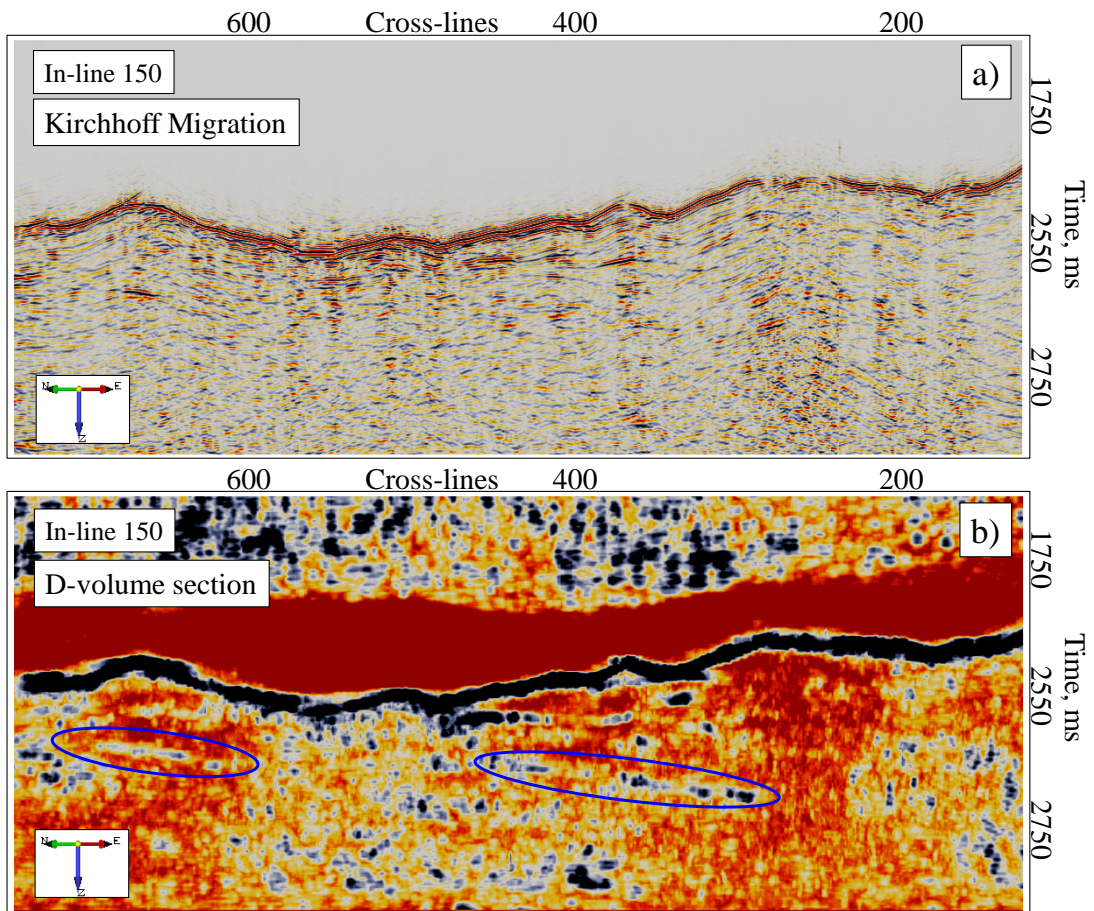


*Figure 6.15. In-line 150 of the Solwara 1 3D seismic volume. a) Kirchhoff migration. b) D-volume section. Concentrations of diffraction energy along linear features, which are unseen on the Kirchhoff image, are circled blue in the section*

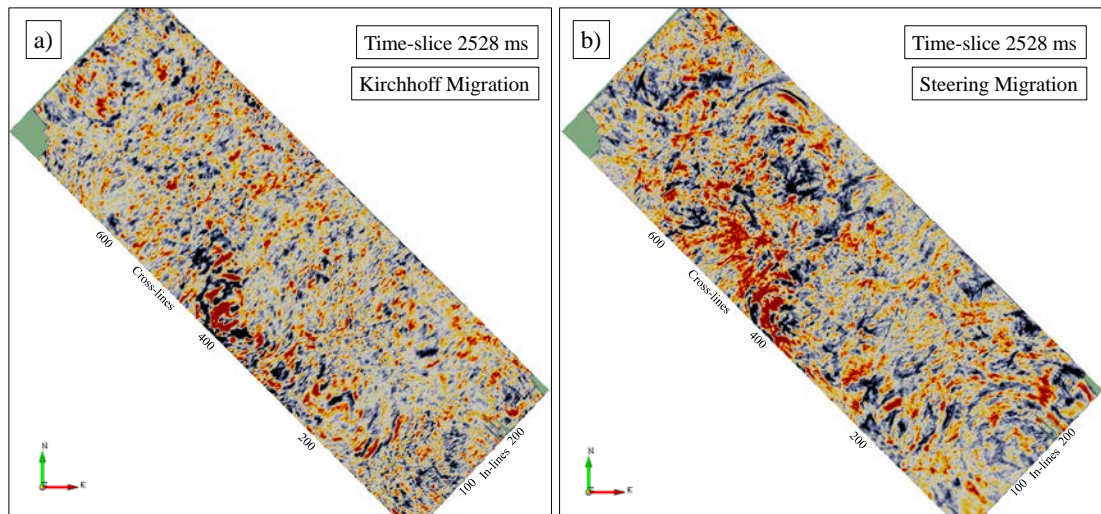


**Figure 6.16.** Time-slices at 2528 ms of the Solwara 1 3D seismic volume. a) Kirchhoff migration. b) Steered migration.

### 6.7. Diffraction Imaging Summary

The modification of weighting summation to the standard Kirchhoff post-stack migration has been suggested in the study. The diffracted wave parameters obtained from the diffraction imaging algorithm have been used to weight the main Kirchhoff summation. The main purpose of the alteration is to improve the signal to noise ratio of the resulting images. A by-product of this process is the D-volume; it represents distribution of focused diffraction energy and supports delineation of geological discontinuities.

The algorithm was successfully tested on a 3D synthetic model. This application has illustrated the stability of the steered migration in the presence of high level random noise; and revealed the greatest improvements in imaging the steeply dipping interfaces. The steered migration was applied to three 3D seismic datasets from different mineral projects with various geological conditions. The algorithm has demonstrated the capability of imaging steep and sharp objects such as fracture and fault zones and lateral heterogeneities and increasing the continuity of the interfaces, and as well an ability to enhance the signal to noise ratio of the final migrated section. The presented applications have shown that in the case of subvertical

geology the diffraction imaging allows one to define linearly extended fault and fracture zones. The research also has shown that the quality of the steered imaging is comparable to a conventional Kirchhoff migration.

The procedure weights seismic amplitudes before summation and no other corrections are involved in this process. Thus, final amplitudes are not consistent and understanding how to deal with amplitudes in the steered migration requires additional research. The current implementation is made only as a time imaging approach with an assumption of hyperbolic moveouts. The steered migration method uses a velocity model as input information and it is sensitive to errors in the model in a way similar to the standard Kirchhoff migration. At the moment, the velocity model is the most sensitive component of the steered migration. The velocity can be introduced as an additional parameter to the semblance estimation. Expansion of the velocity independent approach (Chapter 5) to a 3D case would provide another way of obtaining velocity information.

The main features of the presented steered migration are dealing with noisy data, improving the continuity of steep interfaces and highlighting the subvertical heterogeneities. These benefits have potentially high value for seismic exploration in complex hard rock environments.

## **7. Discussions, Conclusions and Future Outlook**

### ***7.1. Seismic Imaging in Hard Rock Environments***

Successful mining exploration and discovery of new mineral deposits requires a comprehensive understanding of rock forming processes, hydrothermal fluid paths and deep structures as well as geological conditions of shallow successions. Seismic methods are able to construct high resolution 2D and 3D images of near surface strata and deep horizons. However due to several reasons seismic exploration is facing a number of major challenges in hard rock environments:

- High velocity contrast between weathered overburden rocks and base formations as well as inhomogeneous structure of the cover cause distortion of seismic signal and affect quality of recorded data; and at the same time the exploration of a cover regolith is an essential task for mineral targeting and mine design.
- Knowledge of a velocity model is essential for seismic imaging, but obtaining such information is a difficult task due to lack of continuous reflectors and complexity of the geology in hard rock media.
- Hard rock seismic data often have low signal to noise ratio because of various factors: rugged terrain, heterogeneous structure of the overburden formation, low velocity-density contrast, high level of ambient noise in case of surveys conducted in the vicinity of active mines etc.
- Hard rock sites are characterized by the presence of a large number of steeply dipping or subvertical faults, fracture zones and alterations. Such complexity of the geology adds an extra challenge to imaging this environment.

This thesis addresses the main issues for seismic exploration in hard rock environments and focuses on the approaches capable of overcoming these difficulties.

### *Regolith exploration*

Investigation of the overburden provides valuable information for discovery of shallow ore deposits as well as for deep mineral targeting; and designing of mine sites requires the estimation of ground properties. Presence of the regolith cover causes certain difficulties for seismic imaging. The heterogeneous structure of near surface formations should be taken into account during seismic processing (static corrections, etc.) to improve distorted signal. Thus, the altered regolith has to be explored using high density seismic surveys and distribution of shear and compressional velocities should be evaluated to address geological tasks and seismic issues. Several seismic techniques need to be implemented in near surface investigations to achieve such goals.

The comprehensive near surface seismic experiment at Hillside mine site (Chapter 4) combined a number of seismic approaches to investigate shallow subsurface formations and their properties. The near surface seismic survey has revealed the structure of the altered regolith cover using analysis of surface and refracted waves. Employed seismic setups can be used for reliable and fast mapping of the thickness of the regolith and recovering the distribution of elastic properties of the near surface rocks. Estimated velocities of the upper part of geological sections can be used for static corrections in a processing of reflection seismic. Geotechnical information about rock properties, which is evaluated as well from seismic data, is important for designing mining excavation and pit construction. The experiment has also shown that the expenses of acquiring the high dense seismic data could be comparable to the cost of traditional geophysical potential and electromagnetic methods.

### *Velocity estimation in hard rock environments*

One of the biggest challenges that the seismic imaging is facing in hard rock environments is obtaining the essential information about velocity distribution in the media. This difficulty is caused by the complex and discontinuous structures of hard rock formations, lack of acoustic borehole measurements as well as adds a further hardship to the issue. This research has shown that the suggested velocity

independent prestack time imaging algorithm (Chapter 5) can be used as an alternative tool for estimation of the velocity model and as a self-sufficient migration algorithm to create the images of subsurface structures. The additional improvements in the implementation of the method allow us at present to deal with any 2D geometry setups and enhance the quality of the images by the slope-dependent summation. The synthetic tests have demonstrated an ability of the approach to obtain satisfactory results in the presence of high levels of random noise. Comparison with the Kirchhoff prestack time migration has shown that the presented imaging technique produces reasonable seismic sections and the obtained velocity model can be utilized as input data for the conventional migrations. The application to the field dataset from St Ives mining camp has revealed the sufficient geological structural model of the explored area.

The velocity independent imaging is based on the local slopes computation, and to estimate these parameters the semblance approach has been selected as the most robust method even in the presence of random noise. Nonetheless, the quality of the final images relies on the coherency of seismic records and the method requires the thoughtful processing of data before migration. This migration is making a point to point mapping of seismic amplitudes that affects the smoothness of the final sections. The procedure of the slopes calculation is the most time consuming part of the imaging technique, but the repositioning of the events from seismograms to the real locations on the final image takes almost no time. The studied imaging algorithm creates simultaneously the velocity field and migrated image that is the real advantage for hard rock seismic exploration.

#### *Improving signal/noise ratio and revealing subvertical structures*

The hard rock media often contain a lot of subvertical structures (faults, alteration zones, fracture zones, etc.), and such geological elements are usually hardly traceable on seismic data. The study has shown the ability of the 3D imaging approach (Chapter 6) to obtain reliable images of subvertical features and faults using the attribute of focused diffraction energy (D-volume). The seismic signal in mineral exploration is often affected by ambient noise or distorted by the complex environment. Research has demonstrated that the developed diffraction steered

migration algorithm (Chapter 6) has the capability to deal with seismic data with low signal to noise ratio. The steered migration is an alteration to the conventional Kirchhoff post-stack migration, which is using the coherent measurements to identify the seismic traces that do not contribute the energy from the specular reflection point into the final image.

Steered migration was tested on a synthetic 3D seismic volume and applied to three field 3D seismic datasets from different hard rock prospects. The synthetic test has shown that the algorithm is stable in the presence of a high level of random noise and enhances the continuity of steeply dipping interfaces. The application to the field seismic dataset from O'Callaghans mine site has revealed significant improvements to final migrated images compare to results from the standard Kirchhoff migration. The analysis of distribution of diffraction energy has indicated that such volumes (D-volumes) are really useful for faults and fracture detection. The example of seismic data from Hillside camp has confirmed the high potential of the diffraction imaging (D-volumes) to delineate the linear subvertical fault zones. The application of the steered migration to investigate the modern subduction zones in the Bismarck Sea at Solwara mine has improved images of the deep structures and helped to understand the formation mechanisms of seabed deposits in this region.

## ***7.2. Future Research of Seismic Imaging in Mineral Exploration***

This research shows that application of the seismic methods for mineral exploration has good potential and these methods are capable of imaging mineral deposits at various depths. Obtaining reliable images of subsurface geological structures is a great support for successful mineral exploration, and there are a lot of further developments and improvements in seismic imaging that will allow their advanced applications in mining industry. Considering the imaging techniques described in the study, the suggestions for future research are stated below.

Acquisition of surface and refracted waves are inexpensive seismic techniques for exploration the near surface rock formations. They can be acquired and analyse simultaneously or separately depend on tasks. Further advance can be application of the dynamic acquisition systems such as land streamer or 'draggable' geophone

strings. These setups will allow decreasing the time of the data collection process and consequently improving the efficiency of seismic approaches. High channel count acquisition systems with high density survey setups have to be introduced to mine sites investigations to reveal highly inhomogeneous regolith structure and ground properties as well as to improve deep seismic imaging.

The surface wave's method can be recorded in an active mode as well as in a passive mode. The passive modification does not need a particular seismic source for wave generation and records the surface waves from any ambient objects such as moving machinery or drilling rigs. Therefore, it is possible to deploy dense geophone arrays at active mining sites to collect seismic data and develop 3D analysis of surface waves.

The velocity independent imaging algorithms are very desirable for hard rock seismic exploration. As part of future development, we intend to improve the implementation of the presented algorithm in terms of accuracy of estimation of the local event slopes by including quality control of the slope estimation based on the semblance value. Future advances are possible by considering the migration of the events not to a single location. This could be achieved by spreading them over the first Fresnel zone along the estimated dipping interface, or by using Gaussian beams. The modifications to accommodate borehole seismic geometries (VSP, cross-well) and 3D seismic geometry can be made to the method as well.

Diffraction energy is valuable information for seismic imaging especially in complex hard rock environments. For the developed 3D steered algorithm the post-stack Kirchhoff migration has been used as the basis of imaging, however the approach can be easily expanded to other cases, including pre-stack migration. The steered migration takes the input velocity model from the velocity analysis. Building the accurate velocity model is a hard and tedious task in mineral seismic exploration; therefore the velocity itself can be introduced to the algorithm as an additional searching parameter. Searching of the velocity function from a reasonable range can be implemented during the semblance analysis; and then considering to summation the weighted amplitudes by a semblance maximum that based on two parameters:

velocity and azimuth. This alteration will enhance the final image quality by adjusting the velocity information.

Clearly the seismic exploration is a beneficial tool for the mining industry that enables us to provide reliable images of complex subsurface structures and knowledge about rock properties. Adaptation of known imaging techniques and development of new ones is an essential component of the hard rock seismic evolution.

## References

- Adam, E., Perron, G., Milkereit, B., Wu, J., Calvert, A., Salisbury, M., Verpaelst, P. and Dion, D.-J., 2000. A review of high-resolution seismic profiling across the Sudbury, Selbaie, Noranda, and Matagami mining camps. *Canadian Journal of Earth Sciences*, 37(2-3): 503-516.
- Aki, K. and Richards, P., 1980. *Quantitative Seismology: Theory and Methods*. WH Freeman and Co. Cambridge Press, 1: 44-1.
- Alonaizi, F., Alshamry, M., Pevzner, R., Bona, A. and Gurevich, B., 2012. Application of Diffracted Waves Analysis to Edge Detection on 3D and 4D Seismic Data, 74th EAGE Conference & Exhibition.
- Alonaizi, F., Pevzner, R., Bóna, A., Shulakova, V. and Gurevich, B., 2013. 3D diffraction imaging of linear features and its application to seismic monitoring. *Geophysical Prospecting*, 61(6): 1206-1217.
- Arström, K. and Lund, C.E., 1993. Explosion-Generated Short-Period Surface Wave Dispersion and Noise Studies Along Linear Seismic Arrays In Southern Sweden. *Geophysical Journal International*, 114(1): 103-115.
- Bancroft, J.C., 2007. *A Practical Understanding of Pre-and Poststack Migrations: Prestack*, 2. SEG Books.
- Bekker, A., Slack, J.F., Planavsky, N., Krapež, B., Hofmann, A., Konhauser, K.O. and Rouxel, O.J., 2010. Iron formation: the sedimentary product of a complex interplay among mantle, tectonic, oceanic, and biospheric processes. *Economic Geology*, 105(3): 467-508.
- Berkhout, A. and Palthe, D.W., 1980. Migration in the presence of noise. *Geophysical Prospecting*, 28(3): 372-383.
- Berryhill, J.R., 1977. Diffraction response for nonzero separation of source and receiver. *Geophysics*, 42(6): 1158-1176.
- Berson, I.S., , 1957. High-frequency seismic. The USSR Academy of Science, Moscow (in Russian).
- Binns, R.A., 2004. Eastern Manus basin, Papua New Guinea: Guides for volcanogenic massive sulphide exploration from a modern seafloor analogue.

- Copperzinc massive sulfide deposits in Western Australia: CSIRO Explores, 2: 59-80.
- Birch, F., 1960. The velocity of compressional waves in rocks to 10 kilobars, part 1. *Journal of Geophysical Research*, 65(4): 1083-1102.
- Birch, F., 1961. The velocity of compressional waves in rocks to 10 kilobars: 2. *Journal of Geophysical Research*, 66(7): 2199-2224.
- Bóna, A., 2009. Velocityless migration of source gathers, 79th Annual International Meeting, SEG, Expanded Abstracts, pp. 3000-3004.
- Brown, A.R., 1999. Interpretation of three-dimensional seismic data. American Association of Petroleum Geologists and the Society of Exploration Geophysicists.
- Brown, S., Groves, D. and Newton, P., 2002. Geological setting and mineralization model for the Cleo gold deposit, Eastern Goldfields Province, Western Australia. *Mineralium Deposita*, 37(8): 704-721.
- Brune, J. and Dorman, J., 1963. Seismic waves and earth structure in the Canadian shield. *Bulletin of the Seismological Society of America*, 53(1): 167-209.
- Butt, C., Lintern, M. and Anand, R.I., 2000. Evolution of regoliths and landscapes in deeply weathered terrain—implications for geochemical exploration. *Ore geology reviews*, 16(3): 167-183.
- Cassidy, K.F. and Hagemann, S.G., 2001. 'World-class' Archean orogenic gold deposits, eastern Yilgarn Craton: Diversity in timing, structural controls and mineralization styles. *AGSO Journal of Australian Geology & Geophysics*: 382-384.
- Chen, H., 2013. External sulphur in IOCG mineralization: Implications on definition and classification of the IOCG clan. *Ore Geology Reviews*, 51(0): 74-78.
- Claerbout, J.F., 1992. *Earth soundings analysis: Processing versus inversion*, 6. Blackwell Scientific Publications Cambridge, Massachusetts, USA.
- Clout, J. and Simonson, B., 2005. Precambrian iron formations and iron formation-hosted iron ore deposits. *Econ Geol 100th Anniv Vol*: 643-679.
- Cooke, D., Bóna, A. and Hansen, B., 2008. Simultaneous time imaging, velocity estimation and multiple suppression using local event slopes, 2008 SEG Annual Meeting.

- Cooke, D., Bóna, A. and Hansen, B., 2009. Simultaneous time imaging, velocity estimation, and multiple suppression using local event slopes. *Geophysics*, 74(6): WCA65-WCA73.
- Cuellar, V., 1997. Geotechnical applications of the spectral analysis of surface waves. Geological Society, London, Engineering Geology Special Publications, 12(1): 53-62.
- Dalstra, H.J. and Rosière, C.A., 2008. Structural controls on high-grade iron ores hosted by banded iron formation: A global perspective. *Reviews in Economic Geology*, 15: 73–106.
- Debicki, E., 1996. MITEC's Exploration Technology Division: Helping reverse the trend of declining mineral reserves in Canada. *CIM bulletin*, 89(997): 53-59.
- Dobrin, M.B. and Savit, C.H., 1988. Introduction to geophysical prospecting. New York: McGraw2Hill Book Company.
- Dorman, J., Ewing, M. and Oliver, J., 1960. Study of shear-velocity distribution in the upper mantle by mantle Rayleigh waves. *Bulletin of the Seismological Society of America*, 50(1): 87-115.
- Dortman, N.B. and Magid, M.S., 1969. Relations of a velocity of elastic waves and a density of rocks with crystal-chemical characteristics of minerals. *Geology and Geophysics*, 77: 93-105 (in Russian).
- Dragoset, B., 2005. A historical reflection on reflections. *The Leading Edge*, 24(s1): s46-s70.
- Drummond, B.J., Goleby, B.R., Owen, A., Yeates, A., Swager, C., Zhang, Y. and Jackson, J., 2000. Seismic reflection imaging of mineral systems: Three case histories. *Geophysics*, 65(6): 1852-1861.
- Eaton, D.W., Milkereit, B. and Salisbury, M., 2003. Seismic methods for deep mineral exploration: Mature technologies adapted to new targets. *The Leading Edge*, 22(6): 580-585.
- Fomel, S., 2002. Applications of plane-wave destruction filters. *Geophysics*, 67(6): 1946-1960.
- Fomel, S., 2007. Velocity-independent time-domain seismic imaging using local event slopes. *Geophysics*, 72(3): S139-S147.
- Fouqué, F., 1888. *Les tremblements de terre*. Librairie J.-B. Baillière.

- Galley, A., Hannington, M. and Jonasson, I., 2007. Volcanogenic massive sulphide deposits. Mineral Deposits of Canada: A Synthesis of Major Deposit-Types, District Metallogeny, the Evolution of Geological Provinces, and Exploration Methods: Geological Association of Canada, Mineral Deposits Division, Special Publication(5): 141-161.
- Gamburtsev, G.A., Riznichenko, Y.V. and Berson, I.S., 1952. Correlation method of refraction waves. The USSR Academy of Science, Moscow (in Russian).
- Gardner, G., Gardner, L. and Gregory, A., 1974. Formation velocity and density-the diagnostic basics for stratigraphic traps. *Geophysics*, 39(6): 770-780.
- Gibson, H., Allen, R., Riverin, G. and Lane, T., 2007. The VMS model: advances and application to exploration targeting, *Proceedings of Exploration*, pp. 713-730.
- Goldfarb, R., Groves, D. and Gardoll, S., 2001. Orogenic gold and geologic time: a global synthesis. *Ore geology reviews*, 18(1): 1-75.
- Green, A. and Mair, J., 1983. Subhorizontal fractures in a granitic pluton: Their detection and implications for radioactive waste disposal. *Geophysics*, 48(11): 1428-1449.
- Groves, D.I., Bierlein, F.P., Meinert, L.D. and Hitzman, M.W., 2010. Iron oxide copper-gold (IOCG) deposits through earth history: implications for origin, lithospheric setting, and distinction from other epigenetic iron oxide deposits. *Economic Geology*, 105(3): 641-654.
- Groves, D.I., Goldfarb, R.J., Gebre-Mariam, M., Hagemann, S. and Robert, F., 1998. Orogenic gold deposits: a proposed classification in the context of their crustal distribution and relationship to other gold deposit types. *Ore geology reviews*, 13(1): 7-27.
- Hagedoorn, J., 1959. The plus-minus method of interpreting seismic refraction sections. *Geophysical prospecting*, 7(2): 158-182.
- Harlan, W.S., Claerbout, J.F. and Rocca, F., 1984. Signal/noise separation and velocity estimation. *Geophysics*, 49(11): 1869-1880.
- Harlan, W.S., Claerbout, J.F. and Rocca, F.S., 1983. Extracting velocities from diffractions, 1983 SEG Annual Meeting.

- Hatton, L., Worthington, M.H. and Makin, J., 1986. Seismic data processing: theory and practice, Merlin Profiles Ltd.
- Heisey, J., Stokoe, I. and Meyer, A., 1982. Moduli of pavement systems from spectral analysis of surface waves. *Transportation research record*(852).
- Herglotz, G., 1907. Über das Benndorf'sche Problem der Fortpflanzungsgeschwindigkeit der Erdbebenstrahlen. (in German). *Physikal. Zeitschr*, 8: 145-147.
- Hitzman, M.W., Oreskes, N. and Einaudi, M.T., 1992. Geological characteristics and tectonic setting of proterozoic iron oxide (Cu-U-Au-REE) deposits. *Precambrian Research*, 58(1): 241-287.
- Holub, K. and Novotny, O., 1997. Interpretation of the dispersion curves of short-period Rayleigh waves observed in the West Carpathians. *ACTA MONTANA*, 104: 49-58.
- Huygens, C., 1690. *Traite de la lumiere*. Les Maitres de la Pensee Scientifique, Paris.
- Iyer, H. and Hirahara, K., 1993. *Seismic tomography: Theory and practice*. Springer.
- John, D.A., Ayuso, R.A., Barton, M.D., Blakely, R.J., Bodnar, R.J., Dilles, J.H., Gray, F., Graybeal, F.T., Mars, J.C., McPhee, D.K., Seal, R.R., Taylor, R.D. and Vikre, P.G., 2010. Porphyry copper deposit model, chap. B of *Mineral deposit models for resource assessment: U.S. Geological Survey Scientific Investigations Report 2010–5070–B*. 169p.
- Jones, R., 1958. In-Situ Measurement of the Dynamic Properties of Soil by Vibration Methods\*. *Geotechnique*, 8(1): 1-21.
- Juhlin, C. and Palm, H., 2003. Experiences from Shallow Reflection Seismics over Granitic Rocks in Sweden. *Hardrock seismic exploration*(10): 93.
- Kallweit, R. and Wood, L., 1982. The limits of resolution of zero-phase wavelets. *Geophysics*, 47(7): 1035-1046.
- Kanasewich, E.R. and Phadke, S.M., 1988. Imaging discontinuities on seismic sections. *Geophysics*, 53(3): 334-345.
- Karaev, N.A. and Rabinovich, G.Y., 2000. *Ore seismic*. Geoinformmark, Moscow (in Russian).
- Kesler, S.E., 2007. Mineral supply and demand into the 21st century, US Geological Survey circular 1294: proceedings for a workshop on deposit modeling,

- mineral resource assessment, and their role in sustainable development. Reston, VA: US Geological Survey, pp. 55-62.
- Khaidukov, V., Landa, E. and Moser, T.J., 2004. Diffraction imaging by focusing-defocusing: An outlook on seismic superresolution. *Geophysics*, 69(6): 1478-1490.
- Knott, C.G., 1899. Reflexion and refraction of seismic waves. *Philosophical Magazine* 48(290): 64.
- Kovach, R.L., 1965. Seismic surface waves: some observations and recent developments. *Physics and Chemistry of the Earth*, 6: 251-314.
- Krey, T., 1952. The significance of diffraction in the investigation of faults. *Geophysics*, 17(4): 843-858.
- Krylov, S.V., Bryksin, A.V. and Ten, E.N., 1990. Elastic properties of silicate minerals and crystalline rocks for the isotropic model. *Geology and Geophysics*(12): 101-112 (in Russian).
- Landa, E., 2007. Beyond conventional seismic imaging. EAGE publications.
- Landa, E. and Keydar, S., 1998. Seismic monitoring of diffraction images for detection of local heterogeneities. *Geophysics*, 63(3): 1093-1100.
- Landa, E., Shtivelman, V. and Gelchinsky, B., 1987. A method for detection of diffracted waves on common-offset sections. *Geophysical Prospecting*, 35(4): 359-373.
- Large, R.R., 1992. Australian volcanic-hosted massive sulfide deposits; features, styles, and genetic models. *Economic Geology*, 87(3): 471-510.
- Larroque, M., Postel, J.-J., Slabbert, M. and Duweke, W., 2002. How 3D seismic can help enhance mining. *First break*, 20(7): 472-475.
- Leach, D., Sangster, D., Kelley, K., Large, R., Garven, G., Allen, C., Gutzmer, J. and Walters, S., 2005. Sediment-hosted lead-zinc deposits: A global perspective. *Economic Geology*, 100: 561-607.
- Leach, D.L., Bradley, D.C., Huston, D., Pisarevsky, S.A., Taylor, R.D. and Gardoll, S.J., 2010a. Sediment-hosted lead-zinc deposits in Earth history. *Economic Geology*, 105(3): 593-625.
- Leach, D.L., Taylor, R.D., Fey, D.L., Diehl, S.F. and Saltus, R.W., 2010b. A deposit model for Mississippi Valley-type lead-zinc ores. Chapter A of mineral

- deposit models for resource assessment: USGS, Scientific Investigations Report 5070–A.
- Lehmann, B., 2008. Uranium ore deposits. *Rev. Econ. Geol. AMS Online*, 2008: 16-26.
- Li, T., 2009. O’Callaghans Project Western Australia. Presentation to the International Tungsten Industry Association Annual Conference, Vancouver, <http://www.newcrest.com.au/investors/presentations>: accessed September 2009.
- Lipton, I., 2008. Mineral Resource Estimate-Solwara 1 Project, Bismarck Sea, Papua New Guinea for Nautilus Minerals Inc.
- Lipton, I., 2012. Mineral Resource Estimate Solwara Project, Bismarck Sea, Papua New Guinea. Prepared by Golder Associates for Nautilus Minerals Inc.
- Liu, G., Fomel, S., Jin, L. and Chen, X., 2009. Stacking seismic data using local correlation. *Geophysics*, 74(3): V43-V48.
- Love, A., 1911. *Some problems in geodynamics*, Cambridge Univ. Press, Cambridge.
- Lowe, G., 2009. The Hillside Cu-Au Project Hillside Yorke Peninsula, 6th SA Explorers’ Conference, Adelaide, South Australia.
- Lydon, J.W., 1983. Chemical parameters controlling the origin and deposition of sediment-hosted stratiform lead-zinc deposits. SANGSTER, DF Sediment-hosted stratiform lead-zinc deposits. Vitória, Mineralogical Association of Canada: 175-250.
- Lydon, J.W., 1988. Ore deposit models# 14. Volcanogenic massive sulphide deposits Part 2: genetic models. *Geoscience Canada*, 15(1).
- Malehmir, A. and Bellefleur, G., 2009. 3D seismic reflection imaging of volcanic-hosted massive sulfide deposits: Insights from reprocessing Halfmile Lake data, New Brunswick, Canada. *Geophysics*, 74(6): B209-B219.
- Malehmir, A., Juhlin, C., Wijns, C., Urosevic, M., Valasti, P. and Koivisto, E., 2012. 3D reflection seismic imaging for open-pit mine planning and deep exploration in the Kevitsa Ni-Cu-PGE deposit, northern Finland. *Geophysics*, 77(5): WC95-WC108.

- McKay, A.D., Meizitis, Y., Porritt, K., Champion, D.C., Britt, A., Whitaker, A., Summerfield, D., Sexton, M., Jaireth, S., Huston, D., Hoatson, D., Schofield, A., Carson, L., Towner, R. and Huelatt, M., 2013. Australia's Identified Mineral Resources 2012. Geoscience Australia.
- McQueen, K., 2005. Ore Deposit Types and their Primary Expressions. Regolith Expression of Australian Ore Systems;(Eds) CRM Butt, IDM Robertson, KM Scott, M. Cornelius. CRC LEME.
- Milkereit, B., Berrer, E., King, A.R., Watts, A.H., Roberts, B., Erick, A., Eaton, D.W., Wu, J. and Salisbury, M.H., 2000. Development of 3-D seismic exploration technology for deep nickel-copper deposits—A case history from the Sudbury basin, Canada. *Geophysics*, 65(6): 1890-1899.
- Moss, R. and Scott, S.D., 2001. Geochemistry and mineralogy of gold-rich hydrothermal precipitates from the eastern Manus Basin, Papua New Guinea. *The Canadian Mineralogist*, 39(4): 957-978.
- Nafe, J.E. and Drake, C.L., 1963. Physical properties of marine sediments. In: M.N. Hill (Editor), *The sea*. Interscience publishers, New York, pp. 794-815.
- Nazarian, S., Stokoe, I. and Hudson, W.R., 1983. Use of spectral analysis of surface waves method for determination of moduli and thicknesses of pavement systems. *Transportation Research Record*(930).
- Neducza, B., 2007. Stacking of surface waves. *Geophysics*, 72(2): V51-V58.
- Neidell, N. and Taner, M.T., 1971. Semblance and other coherency measures for multichannel data. *Geophysics*, 36(3): 482-497.
- Nelson, R., 1984. Seismic reflection and mineral prospecting. *Exploration Geophysics*, 15(4): 229-250.
- Nemeth, T., Sun, H. and Schuster, G.T., 2000. Separation of signal and coherent noise by migration filtering. *Geophysics*, 65(2): 574-583.
- Novotny, O., 1999. *Seismic Surface Waves*. Instituto de Física, Instituto de Geociências, Salvador, Bahia.
- Ottolini, R., 1983a. Signal/noise separation in dip space. SEP-37: Stanford Exploration Project: 143-149.
- Ottolini, R., 1983b. Velocity independent seismic imaging. SEP-37: Stanford Exploration Project: 59-68.

- Palmer, D., 1980. The Generalized Reciprocal Method of Seismic Refraction Interpretation.
- Paradis, S., Hannigan, P. and Dewing, K., 2007. Mississippi Valley-type lead-zinc deposits. Mineral Deposits of Canada: A Synthesis of Major Deposit-Types, District Metallogeny, the Evolution of Geological Provinces, and Exploration Methods: Geological Association of Canada, Mineral Deposits Division, Special Publication, 5: 185-203.
- Park, C.B., Miller, R.D. and Xia, J., 1999. Multichannel analysis of surface waves. *Geophysics*, 64(3): 800-808.
- Park, C.B., Miller, R.D., Xia, J. and Ivanov, J., 2007. Multichannel analysis of surface waves (MASW)—active and passive methods. *The Leading Edge*, 26(1): 60-64.
- Pirajno, F. and Bagas, L., 2008. A review of Australia's Proterozoic mineral systems and genetic models. *Precambrian Research*, 166(1): 54-80.
- Pretorius, C., Jamison, A. and Irons, C., 1989. Seismic exploration in the Witwatersrand basin, Republic of South Africa, *Proceedings of Exploration*, pp. 241-253.
- Pretorius, C.C., Trewick, W.F. and Irons, C., 1997. Application of 3D seismics to mine planning at Vaal Reefs Gold Mine, Number 10 Shaft, Republic of South Africa. In: A.G. Gubins (Editor), 4th Decennial International Conference on Mineral Exploration. Prospectors and Developers Association of Canada, pp. 399-408.
- Rayleigh, L., 1885. On waves propagated along the plane surface of an elastic solid. *Proceedings of the London Mathematical Society*, 17: 4-11.
- Reitner, J. and Thiel, V., 2011. *Encyclopedia of geobiology*. Springer.
- Riabinkin, L.A., 1957. Fundamentals of resolving power of controlled directional reception (CDR) of seismic waves. In: L. Lu (Editor), *Slant-stack processing*, 1991. SEG, pp. 36-60.
- Richart, F.E., Hall, J.R. and Woods, R.D., 1970. *Vibrations of soils and foundations*.
- Rieber, F., 1936. A new reflection system with controlled directional sensitivity. *Geophysics*, 1(1): 97-106.

- Rietsch, E., 1980. Estimation of the signal-to-noise ratio of seismic data with an application to stacking. *Geophysical Prospecting*, 28(4): 531-550.
- Rowins, S.M., Groves, D.I., McNaughton, N.J. , 1998. Neoproterozoic Telfer-style Au (Cu) deposits. *AGSO Journal of Australian Geology & Geophysics*, 17(4): 217-223.
- Roy, B. and Clowes, R.M., 2000. Seismic and potential-field imaging of the Guichon Creek batholith, British Columbia, Canada, to delineate structures hosting porphyry copper deposits. *Geophysics*, 65(5): 1418-1434.
- Salisbury, M.H., Harvey, C. and Matthews, L., 2003. The acoustic properties of ores and host rocks in hardrock terranes. *Hardrock Seismic Exploration: Society of Exploration Geophysicists, Geophysical Development Series*, 10: 9-19.
- Salisbury, M.H., Milkereit, B., Ascough, G., Adair, R., Matthews, L., Schmitt, D.R., Mwenifumbo, J., Eaton, D.W. and Wu, J., 2000. Physical properties and seismic imaging of massive sulfides. *Geophysics*, 65(6): 1882-1889.
- Salisbury, M.H., Milkereit, B. and Bleeker, W., 1996. Seismic imaging of massive sulfide deposits; Part I, Rock properties. *Economic Geology*, 91(5): 821-828.
- Schleicher, J., Costa, J., Santos, L., Novais, A. and Tygel, M., 2009. On the estimation of local slopes. *Geophysics*, 74(4): P25-P33.
- Schodde, R. and Guj, P., 2012. Where are Australia's mines of tomorrow. Centre for Exploration Targeting, University of Western Australia, September.
- Schodde, R.C., 2012. What's the future for Mineral Exploration in Australia? ... and why we need smart geoscientists now! Presentation to the Geological Society of Australia Victoria Division, Monash, <http://www.minexconsulting.com/publications/oct2012.html>: accessed October 2012.
- Scott, K.M. and Pain, C.F., 2008. *Regolith science*. CSIRO Publishing.
- Shanks, W.C.P., III and Thurston, R., eds, 2012. Volcanogenic massive sulfide occurrence model. U.S. Geological Survey Scientific Investigations Report 2010-5070-C: 345p.
- Sheriff, R. and Geldart, L., 1982. *Exploration seismology, volume 1: history, theory, and data acquisition*.
- Sherrif, R. and Geldart, L., 1995. *Exploration seismology*. Cambridge Univ. Press.

- Shuey, R., 1985. A simplification of the Zoeppritz equations. *Geophysics*, 50(4): 609-614.
- Sillitoe, R.H., 2010. Porphyry copper systems. *Economic Geology*, 105(1): 3-41.
- Stefani, J.P., 1995. Turning-ray tomography. *Geophysics*, 60(6): 1917-1929.
- Stevenson, F. and Durrheim, R., 1997. Reflection seismics for gold, platinum and base metal exploration and mining in southern Africa, Proc. Exploration 97: 4th Decennial International Conference on Mineral Exploration, pp. 391-398.
- Stolz, E., Urosevic, M. and Connors, K., 2004. Reflection Seismic Surveys at St Ives Gold Mine, WA. *ASEG Extended Abstracts*, 2004(1): 1-4.
- Strobbia, C., 2003. Surface wave methods: acquisition, processing and inversion. Torino: Politecnico di Torino.
- Stuart, G.W., Jolley, S.J., Polome, L.G. and Tucker, R.F., 2000. Application of 3-D seismic attributes analysis to mine planning: Target gold deposit, South Africa. *The Leading Edge*, 19(7): 736-742.
- Sword Jr, C.H., 1987. Tomographic determination of interval velocities from reflection seismic data: The method of controlled directional reception, Stanford University.
- Taner, M.T. and Koehler, F., 1969. Velocity spectra-digital computer derivation applications of velocity functions. *Geophysics*, 34(6): 859-881.
- Telford, W.M., Geldart, L.P. and Sheriff, R.E., 1990. *Applied geophysics*, 1. Cambridge university press.
- Trorey, A., 1970. A simple theory for seismic diffractions. *Geophysics*, 35(5): 762-784.
- Twining, M., 2012. The Hillside Project: Australia's Next Great Copper Development, 9th SA Exploration and Mining Conference, Adelaide, South Australia.
- Urosevic, M., Bhat, G. and Grochau, M.H., 2012. Targeting nickel sulfide deposits from 3D seismicreflection data at Kambalda, Australia. *Geophysics*, 77(5): WC123-WC132.
- Urosevic, M. and Evans, B., 2007. Feasibility of seismic methods for imaging gold deposits in Western Australia. , Minerals and Energy Research Institute of Western Australia.

- Van Overmeeren, R., 2001. Hagedoorn's plus-minus method: the beauty of simplicity. *Geophysical prospecting*, 49(6): 687-696.
- Vearncombe, J.R., 1998. Shear zones, fault networks, and Archean gold. *Geology*, 26(9): 855-858.
- Vermeulen, J., Urosevic, M., Gurevich, B. and Landa, E., 2006. Enhancing coherency analysis for fault detection and mapping using 3D diffraction imaging, 2006 SEG Annual Meeting.
- Weatherby, B.B., 1940. The history and development of seismic prospecting. *Geophysics*, 5(3): 215-230.
- Weichert, E., 1910. Bestimmung des weges der erdbebenwellen im erdinneren. I. Theoretisches. *Phys. Z*, 11: 294-304.
- Weinberg, R.F., Hodkiewicz, P.F. and Groves, D.I., 2004. What controls gold distribution in Archean terranes? *Geology*, 32(7): 545-548.
- White, D., Secord, D. and Malinowski, M., 2012. 3D seismic imaging of volcanogenic massive sulfide deposits in the Flin Flon mining camp, Canada: Part 1—Seismic results. *Geophysics*, 77(5): WC47-WC58.
- Whiteley, R.J., 1994. Seismic refraction testing - a tutorial. In: R.D. Woods (Editor), *Geophysical Characterization of Sites*. Oxford & IBH Publishing, pp. 45-47.
- Williams, P., Kopic, A. and Urosevic, M., 2010. Integrated multidisciplinary high resolution 3D geophysics in brownfields and in-mine exploration: New, successful approaches in gold, nickel and uranium deposits, PDAC Conference, Toronto, Canada.
- Williams, P.J., Barton, M.D., Johnson, D.A., Fontboté, L., De Haller, A., Mark, G., Oliver, N.H. and Marschik, R., 2005. Iron oxide copper-gold deposits: geology, space-time distribution, and possible modes of origin. *Economic Geology*: 371-405.
- Witt, W. and Vanderhor, F., 1998. Diversity within a unified model for Archaean gold mineralization in the Yilgarn Craton of Western Australia: an overview of the late-orogenic, structurally-controlled gold deposits. *Ore geology reviews*, 13(1): 29-64.
- Xia, J., Miller, R.D. and Park, C.B., 1999. Estimation of near-surface shear-wave velocity by inversion of Rayleigh waves. *Geophysics*, 64(3): 691-700.

- Yavuz, S., Tertyshnikov, K., Strobach, E. and Urosevic, M., 2012. The Use of Seismic Methods for Imaging Complex Mineral Bodies in Hard Rock Environments, Near Surface Geoscience 2012 – 18th European Meeting of Environmental and Engineering Geophysics Paris, France.
- Yilmaz, Ö., 2001. Seismic data analysis. Society of Exploration Geophysicists.
- Zoeppritz, K., 1919. Erdbebenwellen VII. Nachrichten von der Gesellschaft der Wissenschaften zu Göttingen, Mathematisch-Physikalische Klasse, 1919: 57-65.

Every reasonable effort has been made to acknowledge the owners of copyright material. I would be pleased to hear from any copyright owner who has been omitted or incorrectly acknowledge.